Strong-Field Photodetachment of Negative Ions – Orbital Alignment Effects and Tomographic Imaging of Photoelectrons

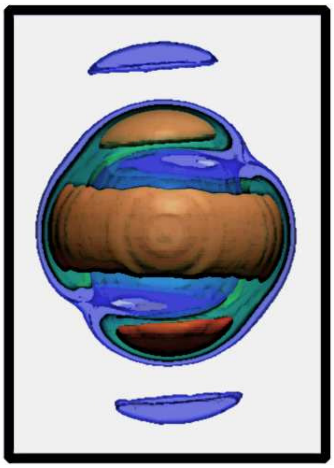

Inaugural-Dissertation
zur Erlangung des Doktorgrades der

Fakultät für Mathematik und Physik der
Albert-Ludwigs-Universität,
Freiburg im Breisgau,
Deutschland

und

Department of Physics,
University of Gothenburg,
Göteborg, Schweden

Vorgelegt von

Mikael Eklund
aus Skövde, Schweden

Juli 2015

Dekan:	Prof. Dr. Dietmar Kröner
Prodekan (Physik):	Prof. Dr. Frank Stienkemeier
Betreuer der Arbeit:	Prof. Dr. Hanspeter Helm Prof. Dr. Dag Hanstorp
Referent:	Prof. Dr. Hanspeter Helm
Koreferent:	
Datum der mündlichen Prüfung:	

Research Publications

Some parts of this thesis have already contributed to the following publications.

Chapter 5:

ORBITAL ALIGNMENT IN ATOMS GENERATED BY PHOTODETACHMENT IN A STRONG LASER FIELD.
Mikael Eklund, Hannes Hultgren, Dag Hanstorp, and Igor Yu. Kiyan.
Phys. Rev. A, 88:023423, Aug 2013.
doi:10.1103/PhysRevA.88.023423.

My contribution: Development of data acquisition and data analysis software. Performance of experiments. Data analysis. Writing the manuscript.

ELECTRON DYNAMICS IN THE GROUND STATE OF A LASER-GENERATED CARBON ATOM.
Hannes Hultgren, Mikael Eklund, Dag Hanstorp, and Igor Yu. Kiyan.
Phys. Rev. A, 87:031404, Mar 2013.
doi:10.1103/PhysRevA.87.031404.

My contribution: Development of data acquisition and data analysis software. Performance of experiments. Data analysis. Writing the manuscript.

Chapter 6:

TOMOGRAPHY OF PHOTOELECTRON DISTRIBUTIONS PRODUCED THROUGH STRONG-FIELD PHOTODETACHMENT OF Ag^-.
Mikael Eklund, Dag Hanstorp, and Hanspeter Helm.
In preparation.

My contribution: Design of experimental setup. Development of data acquisition and data analysis software. Performance of experiments. Data analysis. Writing the manuscript.

In addition to this, the following publication was part of of my PhD work, but falls outside the scope of this thesis:

FEASIBILITY OF PHOTODETACHMENT ISOBAR SUPPRESSION OF WF_5^- WITH RESPECT TO HfF_5^-.
T. Leopold, J. Rohlén, P. Andersson, C. Diehl, M. Eklund, O. Forstner, D. Hanstorp, H. Hultgren, P. Klason, A.O. Lindahl, and K. Wendt.
International Journal of Mass Spectrometry, 359(0):12 – 18, 2014. ISSN 1387-3806. doi:10.1016/j.ijms.2013.12.010.

My contribution: Design and programming of movable mirror. Performance of experiments.

Contents

1 Introduction 1

2 Theoretical Description of Negative Ions and Photodetachment 5

2.1 Negative ions . . . 5
2.2 Photodetachment . . . 6
2.3 Strong-field photodetachment . . . 8
  2.3.1 Strong-field photodetachment of atomic negative ions . . . 9
  2.3.2 Strong-field photodetachment of homonuclear diatomic molecules 15

3 Simulating Photodetachment and Data Processing 19

3.1 Simulating strong-field photodetachment . . . 19
  3.1.1 Simulation of quantum beats . . . 21
3.2 Reconstruction of the 3D photoelectron distribution . . . 23
  3.2.1 Radon transform . . . 29

4 Experimental Setup 31

4.1 Laser System . . . 31
  4.1.1 Data acquisition procedure and optics . . . 33
  4.1.2 Pulse characterization . . . 33
4.2 Ion Accelerator . . . 36
  4.2.1 Sputter source . . . 36
  4.2.2 Ion optics . . . 36
4.3 Electron imaging spectrometer . . . 38
  4.3.1 Velocity map imaging . . . 40
  4.3.2 Projection voltage calibration . . . 40

5 Observation and Simulation of Ground-State Wave Packet Motion in C, Si and Ge 43

5.1 Introduction . . . 43
5.2 Method . . . 45
  5.2.1 Principle of the strong-field ionization probe technique . . . 46
5.3 Experimental procedure . . . 48
5.4 Results . . . 50
5.5 Data analysis and discussion . . . 56

5.6 Simulation 61
5.7 Summary 63

6 Tomography of Electron Emission Patterns **67**
6.1 Introduction 67
6.2 Experimental setup 68
6.3 Results 69
6.4 Discussion 70
6.5 Asymmetry in the polarization plane for photodetachment at 1310 nm . 73
6.6 Conclusion 76

7 Strong-Field Photodetachment of Homonuclear Diatomic Negative Ions **81**
7.1 Introduction 81
7.2 Methods 82
7.3 Results 83
7.4 Discussion 91
7.5 Conclusion 95

8 Conclusion and Outlook **97**

Acknowledgments **99**

Appendix A Effects on Polarization Ellipticity Passing Through a Retarder Plate **101**

Appendix B Discussion of the Lack of Mirror Symmetry in the Polarization Plane **105**

Bibliography **109**

Chapter 1

Introduction

Through the work of many prominent physicists at turn of the 20th century, not only had it been discovered that electricity is quantized in the form of electrons, but that even light itself comes in quanta of photons. Instrumental to these discoveries was the experimental finding[1] by Hertz, and Einstein's subsequent theoretical description[2] of the photoelectric effect, where an electron is emitted from a surface or particle[3] by absorption of a photon. This initial discovery of the wave-particle duality of light was in the coming years extended to matter, and was a key contribution in the creation of an entirely new field of physics – *Quantum Mechanics.*

In this thesis the basic topic of study is *strong-field photodetachment of negative ions.* Photodetachment is nothing but a direct manifestation of the photoelectric effect, with the illuminated target being negative ions. Electrons in bound states in the negative ions are promoted into the continuum by absorption of photons. Photoionization of neutral atoms and molecules in the gas phase has been studied since 1900, but due to the experimental difficulties of producing and containing negative ions, it was not until 1953[4] that photodetachment was first experimentally studied by Branscomb *et al.*. In this first study a conventional light source in the form of a hot tungsten filament was used to photodetach H^- (and in a later experiment also D^-[5]) in order to measure the photodetachment cross section. The electron affinity of O[6] was measured using photodetachment in the same year by the same authors. In 1967 a laser was for the first time used for photodetachment experiments when Brehm *et al.* performed photoelectron spectroscopy on He^- to determine the electron affinity of He[7].

Common to all of these early experiments is that only the total photodetachment rate was considered. In 1968 the theoretical[8] model by Cooper *et al.* and experimental[9] study by Hall of the angular distribution of photoelectrons produced through photodetachment allowed for resolving differential cross sections. The imaging technique adapted to photoelectrons by Helm *et al.* in 1993[10, 11] adds to this by also being able to simultaneously measure the momentum distribution of photoelectrons. The imaging technique was first applied to photodetachment by Blondel *et al.* in 1996 [12] in a study of Br^-. The introduction of Abel inversion[13] and velocity map imaging[14] brought further improvements to the imaging technique.

The first laser in the optical range was developed in 1960[15]. It proved to be an incredibly valuable tool for performing spectroscopy. In the following years the invention of the wavelength-tunable dye laser[16] made it possible for Lineberger and others to measure binding energies of atomic negative ions with high precision[17]. With the advent of mode-locked pulsed titanium-sapphire lasers in the late 1980s and early 1990s, [18, 19, 20] and application of chirped-pulse amplification[21] to optical pulses, the peak power of lasers had reached that of the order of a gigawatt. This opened up an entirely new field of atomic and molecular physics. Strong-field laser physics challenges the notion of optical wavelengths being non-ionizing radiation. In these intense laser fields the photon density is sufficiently high for an atom to pick up a large amount of photons and be ionized even though the energy of the individual photons is insufficient to overcome the ionization threshold. Focusing such a high-power pulse means that the electric field of the laser is comparable to that exerted by the atomic core which makes it possible for a bound electron to pick up more photons than what are needed to overcome the binding potential or even tunnel through the field-induced potential barrier. This *above threshold ionization* (ATI) was first observed in xenon in 1979 by Agostini *et al.*[22], and the corresponding process in negative ions, known as *excess photon detachment* (EPD), was first recorded by Blondel *et al.* in strong-field detachment of F^-[23]. In parallel to and strongly correlated with the development of intense pulses, the duration of laser pulses has been significantly shortened. Today, in a typical pulsed titanium sapphire laser, the pulse duration is of the order of a few femtoseconds. Such a pulse duration is on the timescale of electron dynamics in atoms and opens up an area of application for the laser which has not been reachable before in that the creation of wave packets in the electron distribution of atoms is possible. A wave packet is a fundamental concept in quantum mechanics and is direct evidence of the wave character of matter. A wave packet is formed when a quantum system is in a coherent superposition of states, whose wave functions will interfere constructively in some locations and destructively in other. When the superposition constitutes of a few bound states, this manifests as an oscillation in the probability density, known as a *quantum beat*.

The aim of the experiments presented in this thesis is to experimentally investigate photodetachment of monomer and dimer negative ions in a strong-field regime and compare it to theoretical models. As a tool to perform the experiments, photoelectron imaging methods are used and expanded upon to record and analyze the momentum distributions of photoelectrons produced in photodetachment and photoionization processes. Strong-field photodetachment is also used as a means to create a valence electron wave-packet in neutral atoms. While studies have been performed of electronic wave packets created through superpositions of Rydberg states[24, 25, 26] and lower-lying excited states in atoms[27, 28], as well as in the electronic ground state of positive ions[29, 30], studies of electronic wave packets in the *ground-state* of atoms are lacking. A pump-probe method is employed to study the electron dynamics in C, Si and Ge atoms produced through photodetachment of their respective negative ion. In order to automate the data acquisition procedure and more thoroughly analyze photoelectron emission patterns, a new tomographic method was developed. A tomographic method has been applied before to analyze photoelectron emission patterns from neutral atoms[31], but its applicability in conjunction with low-yield photodetachment experiments had not been tested. The method was applied to photodetachment of the negative ion of silver, where strong-field photodetachment data is scarce. In addition to this, experiments are performed to test the validity of two models for the photodetachment of homonuclear diatomic molecular negative ions. A previous inconclusive comparison has been made for F_2^-[32], but studies are otherwise lacking. As a target, the negative ions of C_2 and Si_2 are used.

This thesis is arranged as follows. In Chapter 2, aspects of the theoretical foundations of negative ions and photodetachment are treated. An existing photodetachment model is generalized to elliptically polarized laser light. Chapter 3 contains details on how the theory is used to simulate photodetachment under experimental conditions, while Chapter 4 describes the setup which has been used to perform the experiments. Chapter 5 deals with the wave packet and orbital alignment dynamics in an atom. In chapter 6, an experimental method to measure the entire 3D momentum distribution of photoelectrons is developed and applied to photodetachment of the negative ion of silver, and in Chapter 7 photodetachment experiments are performed on diatomic molecular negative ions. Finally in Chapter 8, a conclusion and an outlook to future prospects is made.

Chapter 2

Theoretical Description of Negative Ions and Photodetachment

2.1 Negative ions

An atom consists of a nucleus of integer positive charge and an equal amount of negatively charged electrons. The electrons can be thought to be added one by one to the Coulomb potential of the core, in accordance with the Aufbauprinzip, with the probability cloud of each added electron screening one additional nuclear proton. The total charge is thus zero and to a distant observer the unperturbed neutral atom produces no electrical field. In light of this, the mere existence of negative ions, when yet another electron is added to the atom, may seem like a violation of the laws of physics. In a more realistic view where there is mutual interaction between electrons so that their orbitals are altered and their motion is correlated, the existence of negative ions can be easily explained. In a classical view the negatively charged excess electron deforms the electron cloud of the atom, polarizing it, to induce an electric dipole which will exert an attractive force on the excess electron[33]. This induced dipole potential is fundamentally different from the Coulomb potential of positive ions and atoms. While the Coulomb potential has an inverse dependence on the core-electron separation r, i.e. $V \propto \frac{1}{r}$, the long-range behavior of the induced dipole potential is proportional to $\frac{1}{r^4}$[34]. The consequence of this is that the *Electron Affinity* (EA), i.e. the binding energy of of the excess electron is an order of magnitude smaller than that of the Ionization Potential (IP) of an atom, making the negative ion a far more delicate construct. Additionally, the Coulomb potential allows for an infinite number of bound states with the existence of Rydberg states close to the ionization limit; the induced dipole potential only allows a finite number of bound states, in practice limiting the amount of excited states in negative ions to a handful if any. With its apparent simplicity through the scarcity of excited states it makes the negative ion an experimentally attractive target for comparison to theoretical models for laser-induced electron removal.

2.2 Photodetachment

Due to the short range character of the binding potential in the negative ion there are, as mentioned previously, few if any bound electronically excited state. This prohibits traditional methods of spectroscopy, where excitations to bound states are induced and the fluorescence from de-excitation is observed (it should be noted, however, that bound-bound dipole transitions have been observed in a few atomic[35, 36, 37] and diatomic[38, 39] negative ions). To study a negative ion, it is therefore necessary to destroy it by detaching the additional electron or alternatively, in the case of a molecular ion, dissociating it and detecting the fragments. Examples of ways to do this is through application of an external electric field, impacting the negative ion with an electron or a heavier particle like an atom, and through *photodetachment* by exposing the negative ion to laser light, which is the topic of this thesis. The general photodetachment process can be written as

$$A^- + nh\nu \to A + e^- + E, \tag{2.1}$$

where A is an atomic or molecular species, $h\nu$ signifies the photon energy of the n photons absorbed, and $E = EA - nh\nu$ is the excess energy in the process. Since the mass of the residual neutral is much larger than that of an electron, it can be assumed that all the energy is converted into kinetic energy of the detached electron so that $E = \frac{p^2}{2m}$, where p and m is the linear momentum and mass of the electron, respectively. The probability for the process to occur is given by the detachment cross section σ, a measure given in units of area.

In a weak laser field, where one-photon detachment is the only possibility, it is necessary for the photon energy to be larger than the electron affinity, $h\nu > EA$. For an N-electron atomic system with nuclear charge Z, the non-relativistic Hamiltonian is given by (in atomic units $\hbar = m_e = e = 1$) [40]

$$H = \sum_{i=1}^{N} \left(\frac{\mathbf{p}_i^2}{2} - \frac{Z}{r_i} + \sum_{j=i+1}^{N} \frac{1}{|\mathbf{r}_i - \mathbf{r}_j|} \right), \tag{2.2}$$

where $\mathbf{r}_i$ and $\mathbf{p}_i$ are the electron positions and momenta, respectively. Here the first term represents the kinetic energy, the second the potential energy of the electrons in the coulomb field of the nucleus, and the third term represents the Coulomb potential energy between individual electrons. The corresponding Hamiltonian for an atomic system in an external electromagnetic field, such as that of a laser, is obtained by replacing the electron momentum with the generalized momentum, $\mathbf{p}_i \to \mathbf{p}_i + \mathbf{A}(\mathbf{r}_i, t)/c$, where $\mathbf{A}(\mathbf{r}_i, t)$

is the vector potential of the external field, transforming $H \to H + H_{\text{int}}$, where the interaction Hamiltonian H_{int} is given by

$$H_{\text{int}} = \sum_{i=1}^{N} \frac{1}{2c} \left(\mathbf{p}_i \cdot \mathbf{A}(\mathbf{r}_i, t) + \mathbf{A}(\mathbf{r}_i, t) \cdot \mathbf{p}_i + \frac{1}{c} |\mathbf{A}(\mathbf{r}_i, t)|^2 \right). \tag{2.3}$$

The vector potential can be chosen to be in its Coulomb gauge form

$$\mathbf{A}(\mathbf{r}_i, t) = \sqrt{\frac{2\pi c^2}{\omega V}} \hat{\varepsilon} e^{i(\mathbf{k}\cdot\mathbf{r}_i - \omega t)}, \tag{2.4}$$

where $\hat{\varepsilon}$ is the polarization unit vector of the laser light, V a volume, $\mathbf{k}$ the wave vector, and ω the angular frequency of the laser field.

Introducing the *dipole approximation*, $e^{i\mathbf{k}\cdot\mathbf{r}_i} \approx 1$, valid when the wavelength of the incoming light is much larger than the size of an atom (but not too large for a strong laser field [41]), and neglecting the square term for the vector potential in Eq. (2.3), we arrive at the simplified expression

$$H_{\text{int}} = \sqrt{\frac{2\pi}{\omega V}} \sum_{i=1}^{N} \mathbf{p}_i \cdot \hat{\varepsilon} e^{-i\omega t}. \tag{2.5}$$

Excluding the omission of the square vector potential term, this is known as the *velocity gauge* form of the interaction Hamiltonian. The square term can in principle only be neglected in a weak field, in a strong laser field it manifests as an AC Stark shift.

The interaction Hamiltonian (2.5) has the form of a time-harmonic perturbation to the zero-field Hamiltonian given in Eq. (2.2) and time-dependent perturbation theory thus gives that the frequency dependent photodetachment cross section $\sigma(\omega)$ is proportional to[42, 43]

$$\sigma(\omega) \propto \rho(\hbar\omega - EA) |T_{if}|^2 \tag{2.6}$$

where T_{if} is the transition matrix element

$$T_{if} = \langle \psi_i | \, H_{\text{int}}(0) \, | \psi_f \rangle \tag{2.7}$$

for the initial and final states ψ_i and ψ_f and $\rho(\hbar\omega - EA)$ is the density of final states. For photon energies slightly higher than the EA, the photodetachment cross section follows the *Wigner threshold law*[44]

$$\sigma(\omega) \propto (\hbar\omega - EA)^{\ell + 1/2}, \tag{2.8}$$

where ℓ is the orbital angular momentum of the detached electron. The Wigner law is valid for an interaction which decays faster than $1/r^2$ and is thus valid for negative ions but not for atoms[33].

It is worth noting that the interaction Hamiltonian (2.5) can be rewritten in the *length gauge*[40, 43] as

$$H_{\text{int}} = -i\sqrt{\frac{2\pi\omega}{V}} \sum_{i=1}^{N} \mathbf{r}_i \cdot \hat{\varepsilon} e^{-i\omega t}. \tag{2.9}$$

through the equivalent expression for the matrix element

$$\langle\psi_i| \sum_{i=1}^{N} \mathbf{p}_i \,|\psi_f\rangle = -i\omega \,\langle\psi_i| \sum_{i=1}^{N} \mathbf{r}_i \,|\psi_f\rangle \,. \tag{2.10}$$

2.3 Strong-field photodetachment

With increased laser intensity, non-linear effects start playing a role in the photodetachment process. The character of the strong-field photoprocess can be classified by the *Keldysh parameter*[45]

$$\gamma = \omega \frac{\sqrt{2|E_0|}}{F}, \tag{2.11}$$

where ω and F is the angular frequency and electric field strength of the laser field, respectively, and E_0 is the zero-field detachment energy (or ionization energy in the case of photoionization). For $\gamma > 1$, the photoprocess is said to be in the *multiphoton regime*, in which the electron simultaneously picks up the energy of more than a single photon. This can be thought of as having a photon density sufficiently large to allow for a series of virtual states, spaced by the photon energy, which are traversed to overcome the binding potential. In an even stronger laser field, these virtual states can be located in the continuum allowing for *excess photon detachment* (EPD)[23, 22]. In an EPD process the electron absorbs the energy of more than the minimum amount of photons required to overcome the binding energy, resulting in peaks in the photoelectron spectrum spaced by the photon energy. In the perturbation theory limit, the detachment rate is proportional to the n-th power of the photon flux, with n being the number of photons absorbed[46]. For a Keldysh parameter $\gamma \ll 1$, the photoprocess is said to be in the *tunneling regime*. This corresponds to the situation where the external field deforms the atomic potential to the point of forming a potential barrier, through which the electron can tunnel. As can be seen in Eq. (2.11) there is a direct dependence on the frequency of the laser. This can be thought of as the electron needing a certain amount of time to tunnel through the barrier. In the experiments performed in this work the Keldysh parameter, calculated at peak intensity, is in the range 0.1 – 0.4, representing the case where the EPD and tunneling processes are competing.

For a theoretical treatment of photodetachment in this regime, higher order contributions to the photodetachment rates can no longer be a neglected and a non-perturbative approach is necessary. One successful approach is that of a group of closely related theories collectively known as Keldysh-Faisal-Reiss theory (KFR)[45, 47, 48]. KFR theory makes use of a single active electron model, in which the initial state can be described by a single electron in e.g. a zero-range (δ-model) potential[49] and the final state neglects the atomic potential and describes a free electron in a laser field. Neglecting the atomic potential is known as the strong-field approximation (SFA) and is justifiable for a strong-field laser, where the electric field of the laser is comparable to that produced by the atom. Note that while the above discussion is valid also for photoionization of atoms, negative ions are particularly well-suited to test the validity of SFA theories due to the lack of long-range forces exerted by the leftover core on the detached electron. In addition to this, the scarcity of electronically excited states makes the zero-range potential a suitable model as it can only contain a single bound state. The evaluation of the transition matrix elements by means of the saddle-point method was developed by Gribakin and Kuchiev[46, 50] and is described in the next section. An extension to homonuclear diatomic molecules was done by Milosevic[51] and is also discussed below. Modifications of the theory adding the effects of rescattering also exist[52]. Rescattering is the process in which the detached electron is accelerated back by the electric field of the laser and colliding elastically with the core. In the following, rescattering is not considered.

2.3.1 Strong-field photodetachment of atomic negative ions

The goal of this section is to generalize the theory of strong field photodetachment to elliptically polarized light using the methods in [46] for linearly polarized light and [53] for circularly polarized light. For elliptically polarized light the electric field is of the form

$$\mathbf{F}(t) = F(\cos(\omega t)\hat{\mathbf{z}} - \varepsilon \sin(\omega t)\hat{\mathbf{y}}), \tag{2.12}$$

with the laser propagating in the positive x-direction so that $\hat{\mathbf{z}}$ and $\hat{\mathbf{y}}$ are the unit vectors pointing in the direction of the semi-major and semi-minor axes of the polarization ellipse, respectively, and the parameter $\varepsilon \in [-1, 1]$ determines the ellipticity. With a positive ellipticity parameter ε this defines a right-handed polarization when looking in the direction of the laser propagation axis $\hat{\mathbf{x}}$. We consider here the detachment probability over a single laser cycle where the amplitude F can be assumed to be constant. The discussion is limited to the length gauge, since it has been shown to be in better agreement with experimental results than the velocity gauge[54, 55].

Transition Amplitude The n-photon transition amplitude over the period T of one laser cycle from the bound to the detached state is given by

$$A_{\mathbf{p}n} = \frac{1}{T}\int_0^T \langle \Psi_{\mathbf{p}} | V_F | \Psi_0 \rangle \, dt, \tag{2.13}$$

where the initial state Ψ_0 with binding energy E_0 is given by

$$\Psi_0 = \Phi_0 e^{-iE_0 t}. \tag{2.14}$$

Here $\Psi_{\mathbf{p}}$ is the continuum state with drift momentum $\mathbf{p}$, $V_F = -e\mathbf{F}\cdot\mathbf{r}$ is the coupling of the electron ($e = -1$) to the laser field, and Φ_0 is the spatial part of the initial bound state. $\Psi_{\mathbf{p}}$ fulfills the time-dependent Schrödinger equation with the full Hamiltonian $H = p^2/2 + V_F + U_0$, where p is the momentum of the electron, and U_0 is the potential the detached electron experiences from the residual neutral core. In situations where the electric field of the laser is strong, it is possible to neglect the atomic potential U_0 for the final state. This is what is known as the *Strong Field Approximation* (SFA). The SFA is particularly suitable for strong-field photodetachment of negative ions, since the left-over atomic core is neutral and does not exert any long-range Coulomb force on the detached electron. By neglecting the atomic potential we are left with the Hamiltonian $H_{\text{SFA}} = p^2/2 + V_F$, i.e. a free electron in the presence of a laser field. The solution to the time-dependent Schrödinger equation for H_{SFA} is given by the Volkov wave function[56]

$$\Psi_V = e^{i(\mathbf{p}+\mathbf{k}_t)\cdot\mathbf{r} - \frac{i}{2}\int^t (\mathbf{p}+\mathbf{k}_t)^2 dt}, \tag{2.15}$$

where

$$\mathbf{k}_t = e\int^t \mathbf{F}(t')dt' = \frac{eF}{\omega}(\sin(\omega t)\hat{\mathbf{z}} + \varepsilon\cos(\omega t)\hat{\mathbf{y}}) \tag{2.16}$$

is the electron momentum induced by the laser field. By approximating $\Psi_{\mathbf{p}} \approx \Psi_V$ we obtain

$$\begin{aligned} A_{\mathbf{p}n} &\approx \frac{1}{T}\int_0^T \langle \Psi_V | V_F | \Psi_0 \rangle \, dt \\ &= \frac{1}{T}\int_0^T \left\langle e^{i(\mathbf{p}+\mathbf{k}_t)\cdot\mathbf{r} - \frac{i}{2}\int^t (\mathbf{p}+\mathbf{k}_t)^2 dt} \middle| V_F \middle| \Phi_0 e^{-iE_0 t} \right\rangle dt, \end{aligned} \tag{2.17}$$

which evaluates to

$$A_{\mathbf{p}n} \approx \frac{1}{T}\int_0^T (E_0 - \frac{1}{2}(\mathbf{p}+\mathbf{k}_t)^2)\tilde{\Phi}_0(\mathbf{p}+\mathbf{k}_t)e^{iS(\omega t)}dt, \tag{2.18}$$

where

$$S(\omega t) = \frac{1}{2}\int^{t}\left((\mathbf{p}+\mathbf{k}_{t'})^2 - 2E_0\right)dt' = \int^{t}\left(\frac{\mathbf{p}^2}{2} + \frac{\mathbf{k}_{t'}^2}{2} + \mathbf{p}\cdot\mathbf{k}_{t'} - E_0\right)dt' \tag{2.19}$$

is the coordinate-independent part of the classical action and

$$\tilde{\Phi}_0(\mathbf{q}) = \int_{\mathbb{R}^3}\Phi_0(\mathbf{r})e^{-i\mathbf{q}\cdot\mathbf{r}}dr^3 \tag{2.20}$$

is the Fourier transform of the spatial part of the initial state.

The integrand in Eq. (2.18) contains a rapidly oscillating exponential function and can be approximated by means of the saddle point method[57, 46], which states that the integral can be approximated by evaluating the integrand when $S(\omega t)$ is stationary, i.e. when

$$S'(\omega t) = 0. \tag{2.21}$$

Let ωt_μ be the saddle points that are solutions to (2.21). Then by applying the saddle point method, (2.18) reduces to

$$A_{\mathbf{p}n} \approx -\frac{1}{2\pi}\sum_{\mu}(E_0 - \frac{1}{2}(\mathbf{p}+\mathbf{k}_{t_\mu})^2)\tilde{\Phi}_0(\mathbf{p}+\mathbf{k}_{t_\mu})\sqrt{\frac{2\pi}{-iS''(\omega t_\mu)}}e^{iS(\omega t_\mu)}. \tag{2.22}$$

In the general case, Eq. (2.21) has four solutions, two of which have a positive imaginary part. In the following only these two saddle points, denoted by $\mu = \pm 1$, are considered since only these have physical meaning.

As the next step an explicit expression for the action will be derived. In the length gauge the interaction with the laser field puts emphasis on large distances from the core. It is therefore possible to approximate the initial state with an asymptotic form as a zero-range potential wave-function [49]

$$\Phi_0(\mathbf{r}) \approx Ar^{-1}e^{-\kappa r}Y_l^m(\theta,\phi), \tag{2.23}$$

where $E_0 = -\frac{\kappa^2}{2}$, A is a normalization constant and Y_l^m is a spherical harmonic function. The zero-range potential is defined as

$$U_{\mathrm{ZRP}}(\mathbf{r}) = \frac{2\pi}{\kappa}\delta(\mathbf{r})\frac{\partial}{\partial r}r. \tag{2.24}$$

At the saddle points this yields the asymptotic expression for the Fourier transform of the wave function

$$\tilde{\Phi}_0(\mathbf{p}+\mathbf{k}_t) = 4\pi A\mu^l Y_l^m(\hat{\mathbf{p}})\frac{1}{(\mathbf{p}+\mathbf{k}_t)^2 - 2E_0}, \tag{2.25}$$

where $\hat{\mathbf{p}}$ is the unit vector in the direction of $\mathbf{p} + \mathbf{k}_t$.

Inserting (2.25) into (2.22) gives the final expression for the transition amplitude

$$A_{\mathbf{p}n} \approx -A \sum_{\mu} \mu^l Y_l^m(\hat{\mathbf{p}}) \sqrt{\frac{2\pi}{-iS''(\omega t_\mu)}} e^{iS(\omega t_\mu)}. \tag{2.26}$$

The differential n-photon detachment rate is given by

$$dw_n = 2\pi |A_{\mathbf{p}n}|^2 \delta(U_p - E_0 - n\omega) \frac{d^3p}{(2\pi)^3} \tag{2.27}$$

which by integration over p yields

$$\frac{dw_n}{d\Omega} = \frac{p}{(2\pi)^2} |A_{\mathbf{p}n}|^2, \tag{2.28}$$

where $p = \sqrt{2(n\omega - F^2(1+\varepsilon^2)/4\omega^2 + E_0)}$ is the momentum of the detached electron as determined by energy conservation. U_p is the ponderomotive energy defined below.

As an example, for the ground state of Ag^- the single active electron is in the 5s state. We thus have $\ell = m = 0$ meaning that (2.26) reduces to

$$A_{\mathbf{p}n} \approx -A \sum_{\mu=\pm 1} \sqrt{\frac{1}{2S''(\omega t_\mu)}} e^{iS(\omega t_\mu)}, \tag{2.29}$$

where the normalization constant is $A = 1.3$ [50].

Saddle points In order to derive the explicit expression for (2.19) we note that

$$\frac{\mathbf{k}_t^2}{2} = \frac{1}{2}\frac{e^2F^2}{\omega^2}\left(\sin^2(\omega t) + \varepsilon^2 \cos^2(\omega t)\right) = U_p + \frac{1}{4}\frac{e^2F^2}{\omega^2}\cos(2\omega t)(\varepsilon^2 - 1), \tag{2.30}$$

where

$$U_p = \frac{1}{T}\int_0^T \frac{\mathbf{k}_t^2}{2} dt = \frac{1}{4}\frac{e^2F^2}{\omega^2}(1+\varepsilon^2) \tag{2.31}$$

is the mean quiver energy of the electron, also known as the *ponderomotive energy*. Furthermore

$$\mathbf{p}\cdot\mathbf{k}_t = \begin{pmatrix} p_\perp \\ -p_\parallel \sin(\theta) \\ p_\parallel \cos(\theta) \end{pmatrix} \cdot \frac{eF}{\omega} \begin{pmatrix} 0 \\ \varepsilon\cos(\omega t) \\ \sin(\omega t) \end{pmatrix} = \frac{eFp_\parallel}{\omega}\left(\cos(\theta)\sin(\omega t) - \varepsilon \sin(\theta)\cos(\omega t)\right). \tag{2.32}$$

Here $p_\perp$ is the photoelectron momentum in the direction perpendicular to the laser polarization plane, $p_\parallel$ is the momentum in the polarization plane at an emission angle of $\theta \in [0, 2\pi)$ such that θ increases in the clockwise direction when looking along the laser propagation axis. By introducing the angle

$$\theta_{\text{eff}} = \arctan(\varepsilon \tan(\theta)) \tag{2.33}$$

(2.32) can be rewritten as

$$\mathbf{p} \cdot \mathbf{k}_t = \frac{eFp_\parallel \sqrt{\cos^2(\theta) + \varepsilon^2 \sin^2(\theta)}}{\omega} \sin(\omega t - \theta_{\text{eff}}), \tag{2.34}$$

where the branch of the arctangent is chosen so that θ_{eff} is the angle which $(\cos(\theta)\hat{\mathbf{z}} - \varepsilon \sin(\theta)\hat{\mathbf{y}})$ makes with the positive z-axis.

Energy conservation requires that

$$n\omega = \frac{\mathbf{p}^2}{2} + U_p - E_0. \tag{2.35}$$

Equation (2.19) can then be rewritten as

$$S(\omega t) = n\omega t - \frac{z}{2} \sin(2\omega t) - \xi \cos(\omega t - \theta_{\text{eff}}), \tag{2.36}$$

where

$$\begin{aligned} z &= \frac{e^2F^2}{4\omega^3}(1 - \varepsilon^2) && (2.37) \\ \xi &= \frac{p_\parallel eF}{\omega^2} \sqrt{\cos^2(\theta) + \varepsilon^2 \sin^2(\theta)}. && (2.38) \end{aligned}$$

The first and second derivatives of the action with respect to ωt are then given by

$$\begin{aligned} S'(\omega t) &= n - z\cos(2\omega t) + \xi \sin(\omega t - \theta_{\text{eff}}) && (2.39) \\ S''(\omega t) &= 2z \sin(2\omega t) + \xi \cos(\omega t - \theta_{\text{eff}}). && (2.40) \end{aligned}$$

Setting (2.39) equal to zero and solving for ωt yields four saddle points in the general case, two of which are lying in the half-plane with $\text{Im}(\omega t_\mu) > 0$. The solutions are analytical, but in the elliptical case the expressions are very involved so that a numerical solution is preferable. For purely linear and circular polarization, however, the saddle points can be expressed concisely as will be done below.

Limiting cases - linear and circular polarization For a linearly polarized laser field, i.e. setting $\varepsilon = 0$, the parameters of Eq. (2.36) become

$$\begin{aligned} z &= \frac{e^2F^2}{4\omega^3} && (2.41)\\ \xi &= \frac{eFp_\parallel}{\omega^2}\cos\theta && (2.42)\\ \theta_{\text{eff}} &= 0. && (2.43) \end{aligned}$$

The action then reduces to

$$S(\omega t) = n\omega t - \frac{z}{2}\sin(2\omega t) - \xi\cos(\omega t). \qquad (2.44)$$

This expression is exactly what is described in Ref. [46], and accordingly the sine and cosine of the saddle points can in this case be expressed as

$$\begin{aligned} \sin(\omega t_\mu) &= \frac{-\xi + i\mu\sqrt{8z(n-z)-\xi^2}}{4z} && (2.45)\\ \cos(\omega t_\mu) &= \mu\sqrt{1-\sin^2(\omega t_\mu)}, && (2.46) \end{aligned}$$

with $\mu = \pm 1$.

Setting $\varepsilon = \pm 1$ for a circularly polarized field yields

$$\begin{aligned} z &= 0 && (2.47)\\ \xi &= \frac{eFp_\parallel}{\omega^2} && (2.48)\\ \theta_{\text{eff}} &= \theta && (2.49) \end{aligned}$$

so that the expression for the action is

$$S(\omega t) = n\omega t - \xi\cos(\omega t - \theta), \qquad (2.50)$$

in agreement with Ref. [53]. In the case of circularly polarized light, the two saddle points merge into a single one which can be expressed as

$$\omega t_\mu = \theta + \frac{3}{2}\pi + i\ln\left(\frac{n\omega^2}{Fp_\parallel} + \sqrt{\frac{n^2\omega^4}{F^2p_\parallel^2} - 1}\right). \qquad (2.51)$$

It should be noted that the above generalization is not able to explain the lack of mirror symmetry, which appears in Chap. 6, as a consequence of an elliptical polarization. In order to do this it is necessary to use a model which takes into account the interaction of the detached electron with the residual core. There are extensions to the SFA theory which adds such Coulomb correction terms to introduce an asymmetry for strong-field photoionization in an elliptically polarized field[58]. A more thorough treatment of strong-field photodetachment in an elliptically polarized field using the quasistationary quasienergy state (QQES) method is treated in Ref. [59] and a brief summary thereof is given in section 6.5.

2.3.2 Strong-field photodetachment of homonuclear diatomic molecules

The goal of this section is to briefly describe the two models of strong-field ionization of homonuclear diatomic molecules developed in Ref. [51].

The theoretical models developed for strong-field detachment/ionization are based on a three particle system - a single electron and two atomic cores. This has a few important consequences compared to models for monoatomic systems. The molecules have an internuclear axis which can be arbitrarily oriented with respect to the laser polarization axis, which increases the computational requirements by two orders of magnitude. Considering the molecular orbital as a linear combination of atomic orbitals, the atomic orbitals of the two cores can be added either symmetrically or antisymmetrically. This gives rise to constructive or destructive interference, significantly altering the photoelectron distribution as compared to an atom with the same detachment energy. The spatial separation of the two cores means that the electric potential induced by the electric field of the laser differs between them. In the paper by Milosevic, two different models for strong-field ionization are presented. In the undressed version of the theory, the potential difference between the two cores is neglected and in the dressed version, the potential difference is assumed to cause a phase difference for electrons ejected from either of the cores. This can significantly alter the interference pattern in the photoelectron distribution.

In the following the theory for atomic negative ions in the previous section is modified by simply replacing the initial wave function Φ_0 with its molecular counterpart Φ_0^q to derive the transition amplitude for molecules. The superfix q signifies whether the undressed ($q = u$) or dressed ($q = d$) version of the theory is treated. We follow the lead of Milosevic, although it is not necessary to modify the interaction term ([51], Eq. (20)) for detachment of a negative ion since the final state of the molecule is electrically neutral. We limit ourselves to a single active electron model and take the initial wave function to be the highest occupied molecular orbital (HOMO). Using a linear combination of atomic orbitals (LCAO) and assuming a constant internuclear distance, the initial state can be described as

$$\Phi_0^u = A \sum_{s=\pm 1} c_s \Phi_{0s}(\mathbf{r} + s\mathbf{R}_0/2), \tag{2.52}$$

where Φ_{0s} are appropriately chosen and oriented zero-range atomic wave functions given by Eq. (2.23) for the two cores labeled $s = \pm 1$. $\mathbf{r}$ is the position vector relative to a point located at the center of the internuclear axis, $\mathbf{R}_0$ is the relative internuclear position vector and A is a normalization constant. The above wave function describes the undressed initial state, unaffected by the laser field. The dressed initial state requires us to take into account the difference in electric potential between the two cores. Taking the electric potential to be zero at the origin and the R-axis to lie along the internuclear axis, the potential at the two atomic cores becomes

$$V_s(t) = -\int_0^{sR_0/2} \mathbf{F}(t) \cdot \hat{R} dR = -s\mathbf{F}(t) \cdot \mathbf{R}_0/2. \tag{2.53}$$

This gives rise to a phase shift which adds a factor of

$$e^{\int^t V_s(t')dt'} = e^{\int^t -s\mathbf{F}(t) \cdot \mathbf{R}_0/2 dt'} = e^{-s\mathbf{k}_t \cdot \mathbf{R}_0/2} \tag{2.54}$$

to the atomic orbitals so that the laser-dressed initial wave function is

$$\Phi_0^d = A \sum_{s=\pm 1} c_s e^{-s\mathbf{k}_t \cdot \mathbf{R}_0/2} \Phi_s(\mathbf{r} + s\mathbf{R}_0/2). \tag{2.55}$$

Using the molecular wave functions instead in the above treatment yields the transition amplitude that can be written as

$$A_{\mathbf{p}n} \approx \frac{1}{T} \int_0^T \mathscr{F}^q(t) e^{iS(\omega t)} dt \tag{2.56}$$

with

$$\mathscr{F}^u(t) = A(E_0 - \frac{1}{2}(\mathbf{p} + \mathbf{k}_t)^2) \sum_{s=\pm 1} c_s e^{is(\mathbf{p}+\mathbf{k}_t) \cdot \mathbf{R}_0/2} \tilde{\Phi}_{0s}(\mathbf{p} + \mathbf{k}_t) dt \tag{2.57}$$

in the undressed case and

$$\mathscr{F}^d(t) = A(E_0 - \frac{1}{2}(\mathbf{p} + \mathbf{k}_t)^2) \sum_{s=\pm 1} c_s e^{is\mathbf{p} \cdot \mathbf{R}_0/2} \tilde{\Phi}_{0s}(\mathbf{p} + \mathbf{k}_t) dt \tag{2.58}$$

in the dressed case.

As in the atomic case, this can be approximated using the saddle-point method and thus yields the final expression for the transition amplitude

$$A_{\mathbf{p}n} \approx -\frac{1}{2\pi} \sum_{\mu=\pm 1} \mathscr{F}^q(t_\mu) \sqrt{\frac{2\pi}{-iS''(\omega t_\mu)}} e^{iS(\omega t_\mu)}. \tag{2.59}$$

In the above, the vibrational wave functions are not considered, but this is easily accounted for by adding the vibrational overlap factor

$$S_{\nu_f \nu_i} = \int_0^\infty \varphi^*_{\nu_f}(R) \varphi_{\nu_i}(R) dR \tag{2.60}$$

to the transition amplitude. Here R is the internuclear distance, and $\varphi_{\nu_f}(R)$ and φ_{ν_i} are final and initial vibrational wave functions, respectively.

Chapter 3

Simulating Photodetachment and Data Processing

3.1 Simulating strong-field photodetachment

The theoretical description of strong-field photodetachment described in section 2.3.1 assumes that the electric field strength F is constant with respect to time, albeit switched on adiabatically, and the detachment rate per laser cycle is calculated. Under experimental conditions this is of course not true since we have a both temporal and spatial variation of the laser intensity. In addition to this we also need to consider saturation effects. For detachment where few photons are needed, saturation can occur significantly before the intensity of the pulse reaches its maximum.

It is sufficient to limit the spatial dependence of the laser intensity to the radial direction as the Rayleigh length of the laser beam is sufficiently large compared to the waist of the focused ion beam for the axial variation to be negligible.

The laser beam is assumed to be Gaussian in both its temporal and radial profile so that the spatio-temporal intensity distribution for the laser intensity is given by

$$I(r,t) = I_0 e^{-(t/\sigma_t)^2} e^{-(r/\sigma_r)^2}, \tag{3.1}$$

where t is time and r is the radial position while σ_t and σ_r determine the width of the Gaussian, and thus the amplitude of the electric field is

$$F(r,t) = F_0 e^{-(t/\sigma_t)^2/2} e^{-(r/\sigma_r)^2/2}. \tag{3.2}$$

The detachment rate $w(F(r,t))$ can be obtained by integrating (2.28) over the unit sphere. Let $n(r,t)$ be the density of negative ions at a given position and time. Then the amount of detachment events during time dt is given by $n(r,t)w(F(r,t))dt$ so that we can set up the rate equation

$$\frac{dn}{dt} = -n(r,t)w(F(r,t)) \tag{3.3}$$

which has the solution

$$n(r,t) = n_0(r)\exp\left(-\int_{-\infty}^{t} w(F(r,t'))dt'\right), \tag{3.4}$$

where $n_0(r)$ is the initial density, usually set to unity.

Using the spatio-temporal population of negative ions in (3.4) as a weight, we can express the full-pulse differential electron yield as the double integral

$$\frac{dW}{d\Omega} = \int_0^\infty \int_{-\infty}^\infty n(r,t)\frac{d}{d\Omega}w(F(r,t))dtdr \tag{3.5}$$

where

$$\frac{dw}{d\Omega} = \frac{1}{(2\pi)^2}\sum_n p|A_{\mathbf{p}n}|^2. \tag{3.6}$$

The integrals are approximated using the trapezoidal method [60] in the ranges $[-3\sigma_t, 3\sigma_t]$ and $[0, 3\sigma_r]$ for t and r, respectively, with a step size of $\sigma/100$.

Molecules For detachment of molecules one also needs to consider the random orientation of the molecules with respect to the laser field polarization. Let $\hat{R}$ be the unit vector pointing along the internuclear axis. Let α be the angle between the laser polarization axis in laboratory coordinates $\hat{z}$, and $\hat{R}$

$$\cos(\alpha) = \hat{z}\cdot\hat{R}. \tag{3.7}$$

Then the total simulated distribution is obtained by integrating Eq. (3.5)

$$\frac{dW_{\text{tot}}}{d\Omega} = \int_0^\pi \frac{dW(\alpha)}{d\Omega}\sin(\alpha)d\alpha. \tag{3.8}$$

The integral is evaluated by summing the contribution for angles with a step size of $\pi/60$.

3.1.1 Simulation of quantum beats

The goal of this section is to describe a model for the pump-probe experiment described in Chap. 5. A hole is created in the electron distribution of a neutral atom by means of strong-field photodetachment by a first laser pulse. This produces a quantum beat between fine-structure states, manifesting as an oscillation in the electron distribution, which is probed by subsequent strong-field photoionization. The discussion is limited to atomic species in the carbon group as this is what was used in the experiments.

As can be seen in Eq. (2.26), there is a dependence on ℓ and m_ℓ in the detachment rate through the appearance of a spherical harmonic. For ion species with valence electrons with a non-zero value for ℓ, one thus needs to take into account the population of different spin-orbit states. This can be done by statistically populating a density matrix as will be shown below.

Negative ions produced in the sputter source described in Sec. 4.2 are fully incoherent and the population of spin-orbit states are merely given by their statistical weights. In the pump-probe experiment described in Chap. 5, however, neutral atoms produced through photodetachment are created in a coherent state. The reason for this is that for an electron with $\ell \neq 0$, using the polarization axis of the linearly polarized laser pulse as a quantization axis, orbitals with $m_\ell = 0$ are preferentially detached. This is intuitively clear for detachment in the tunneling regime, but also holds true in the multi-photon regime as will be shown in Chap. 5.

In order to populate the density matrix for the neutral, strong-field photodetachment simulations are made for the individual spin-orbit states to determine the ratio between the photodetachment probabilities. The simulations are made for full pulse photodetachment taking saturation into account.

Let M'_L designate the total magnetic quantum number of the negative ion. For the ground state of the negative ions of carbon, silicon and germanium, the valence shell with $\ell = 1$ is half-filled with three electrons with $m_\ell = -1, 0, 1$, respectively. Now $M'_L = M_L + m_{\ell_3}$, where M_L is the magnetic quantum number of the neutral atom and m_{ℓ_3} that of the excess electron. Since the ground state of the negative ion is ${}^4S$, $M'_L = 0$ so that necessarily

$$M_L = -m_{\ell_3}. \tag{3.9}$$

Detachment of an $m_\ell = 0$ electron thus leaves the neutral in the $M_L = 0$ state and detaching an $m_\ell = \pm 1$ electron results in the neutral being in the $M_L = \mp 1$ state.

Because of the different probabilities for detaching an electron in a $m_\ell = 0$ and one in a non-zero state, we assign a weight to how the initial density matrix is populated

$$W_{M_L} = \begin{cases} d_{\mathrm{NI}}, & M_L = 0 \\ 1, & M_L \neq 0 \end{cases}, \tag{3.10}$$

where d_{NI} is the ratio between the detachment rate for m_ℓ zero and non-zero. The detachment rates are calculated over an entire laser pulse for the full solid angle, taking the spatial intensity distribution and saturation effects into account.

The initial density matrix after detachment is then given by

$$\rho(0) = N \sum_{M_L=-1}^{1} \sum_{M_S=-1}^{1} W_{M_L} \left| M_L, M_S \right\rangle \left\langle M_L, M_S \right|, \tag{3.11}$$

where N is a normalization constant determined by

$$N = \frac{1}{\sum_{M_L=-1}^{1} \sum_{M_S=-1}^{1} W_{M_L}} = \frac{1}{3(2 + d_{\mathrm{NI}})}. \tag{3.12}$$

The initial density matrix is diagonal in the uncoupled $\{\langle M_L, M_S|\}$ basis but will have off-diagonal coherences in the coupled $\{\langle J, M_J|\}$ representation. The temporal evolution of the density matrix is then given in atomic units by

$$\rho(t) = e^{-itH} \rho(0) e^{itH}, \tag{3.13}$$

where H is the Hamiltonian having the excitation energies relative to $J = 0$ as diagonal entries. As a next step we form a *reduced density matrix*

$$\rho(M_L, t) = tr_{M_S}(\rho(t)), \tag{3.14}$$

by taking the *partial trace*[61] over the spin magnetic quantum number manifold. The partial trace over a manifold Φ is defined as

$$tr_\Phi(\rho(t)) = \sum_i \left\langle \Phi_i \right| \rho(t) \left| \Phi_i \right\rangle. \tag{3.15}$$

The population of atoms in state M_L at a time t is then given by the (M_L, M_L) element of the reduced density matrix.

$$\rho(M_L, t)_{M_L M_L} = \left\langle M_L \right| \rho(M_L, t) \left| M_L \right\rangle. \tag{3.16}$$

Changing the basis of the density matrix in (3.16) to the uncoupled representation $\{\langle m_{\ell_1}, m_{\ell_2}|\}$ for the two valence shell electrons allows for determination of the population of the m_ℓ orbitals. Again applying the theory for strong-field ionization allows for simulating the experimental signal.

The orientation of the laser polarization axis of the pump pulse can be set by rotating the system by means of the small Wigner d-matrix

$$d^j_{m'm}(\alpha) = \left\langle jm' \right| e^{-i\alpha J_k} \left| jm \right\rangle , \tag{3.17}$$

where α signifies the rotation angle around the k-axis with corresponding angular momentum operator J_k. The angular momentum is determined by j, while m and m' are the angular momentum projection quantum numbers with respect to the old and new quantization axes, respectively. Defining the k-axis to be the laser propagation axis, and $\alpha = \pi/2$ thus changes the quantization axis from an axis perpendicular to the detector surface, to an axis parallel to it.

3.2 Reconstruction of the 3D photoelectron distribution

As will be described in section 4.3, the three-dimensional electron swarm created in the photodetachment process is projected onto a two-dimensional detector. When the laser polarization is either linear or circular, a spatial symmetry axis is present in the electron swarm. For linear polarization, the symmetry axis is defined by the polarization axis and for circular polarization, the symmetry axis is defined by the propagation direction of the laser beam. As long as the symmetry axis is kept parallel to the detector surface, the projection can be described mathematically by the *Abel transform*

$$F(x,z) = \int_{-\infty}^{\infty} f(\rho,z) dy = 2\int_{x}^{\infty} \frac{f(\rho,z)}{\sqrt{1-x^2/\rho^2}} d\rho, \tag{3.18}$$

where x and z are the coordinates parallel to the detector surface, with z being the polarization axis, y the coordinate perpendicular to the detector surface and $\rho = \sqrt{x^2+y^2}$. Since in most cases one is interested in the original momentum distribution of photoelectrons and not its projection, the recorded image needs to be inverted. The inverse transform to Eq. (3.18) is given by

$$f(\rho,z) = -\frac{1}{\pi}\int_{r}^{\infty} \frac{dF(x,z)}{dx} \frac{1}{\sqrt{x^2-\rho^2}} dx. \tag{3.19}$$

While the explicit inverse, or rather a discretized version thereof, could be used for inversion, doing so is not recommended due to its noise sensitivity. For a high projection field, where the electron swarm expansion during projection is negligible, the inversion process is essentially one-dimensional and can be performed line by line.

A number of inversion algorithms exist, e.g. BASEX [62], pBASEX [63], where the projected image is fitted to a set of well-behaved basis functions that have known inversions, Fourier-Hankel inversion which works by applying transforms, and ”onion peeling” [13] which is an iterative approach. Each of the inversions have their strengths and weaknesses which will be discussed briefly below. In the following the use of lower case f indicates a function that describes the full or part of the three dimensional distribution and upper case F indicates its projection.

BASEX The BASEX method uses a line-by-line approach by fitting each line of the inverted image to a set of functions. It is assumed that the electron distribution at a certain z-position can be written as an expansion

$$f(\rho) = \sum_{k=0}^{K} w_k f_k(\rho) \tag{3.20}$$

where f_k are appropriately chosen functions with a known projection. In [62], the authors use a Gaussian-like function

$$f_k(\rho) = (e/k^2)^{k^2} (\rho/\sigma)^{2k^2} e^{-(\rho/\sigma)^2}. \tag{3.21}$$

The parameter σ determines the width of the basis functions and is usually set to the pixel size so as to be able to reconstruct sharp features of the image. The functions closely resemble a Gaussian with its maximum at $\rho = k\sigma$. Via the Abel transform in Eq. (3.18), one obtains the analytic expression for its projection

$$\begin{aligned} F_k(x) &= 2\int_x^\infty \frac{f_k(\rho)}{\sqrt{1 - x^2/\rho^2}} d\rho \\ &= 2\sigma f_k(x) \left(1 + \sum_{l=1}^{k^2} (x/\sigma)^{-2l} \times \prod_{m=1}^{l} \frac{(k^2 + 1 - m)(m - 1/2)}{m}\right). \end{aligned} \tag{3.22}$$

The projected line can through the linearity of the Abel transform be expressed as

$$F(x) = \sum_{k=0}^{K} w_k F_k(x). \tag{3.23}$$

By fitting a line of the experimental image to Eq. (3.23) to calculate the expansion coefficients w_k, the original distribution in Eq. (3.20) is determined.

The advantages of BASEX over iterative algorithms as onion peeling are its computational efficiency, better performance for noisy pictures and the fact that the expression for the inverted image is analytical.

pBASEX The pBASEX is similar to the BASEX method in that it fits the experimental image to a set of basis functions. The difference is that while BASEX inverts line-by-line, pBASEX fits the entire image at once. It does this by using the intrinsically polar nature of photoprocesses induced by linearly (or circularly) polarized light. Photoelectrons are assumed to be distributed on a finite set of spherical shells with a Gaussian distribution in the radial direction. The dependence on the polar angle θ of the photoelectron distribution can be expanded in Legendre polynomials so that the distribution is given by

$$f(\rho,\theta) = \sum_{k=0}^{K}\sum_{l=0}^{L} w_{kl} f_{kl}(\rho,\theta) \tag{3.24}$$

with

$$f_{kl}(\rho,\theta) = e^{-(\rho-\rho_k)^2/\sigma} P_l(\cos(\theta)). \tag{3.25}$$

Here σ determines the width of the Gaussian and ρ_k is the radius of the k-th spherical shell. The number of fit functions can be reduced for linearly polarized light, where only even Legendre polynomials need to be used. In addition to this, for an n-photon process, L can be set to $L = 2n$ [63].

In the same way as for the BASEX method, the expansion coefficients can be determined by fitting the experimental image to the projection basis expansion

$$F(P,\Theta) = \sum_{k=0}^{K}\sum_{l=0}^{L} w_{kl} F_{kl}(P,\Theta), \tag{3.26}$$

where $F_k(P,\Theta)$ are the projections of the basis functions in image polar coordinates (P,Θ). When an explicit expression for the projections $F_k(P,\Theta)$ is lacking, they can be calculated numerically.

The biggest difference between the pBASEX method and the other inversion methods is that it accumulates the noise induced error to the center of the image instead of accumulating it to the symmetry axis. The method is very sensitive to centering the image properly and calculating the projections is very resource intensive, although this only needs to be done once. Its biggest flaw lies in its inherent symmetrization of the image and the small basis set used. Inverted images are in a sense artificial and aesthetically appealing so that inversion artifacts can be difficult to identify.

Fourier-Hankel method Another method makes use of the *Projection-Slice Theorem*[64]. The theorem states that for a two-dimensional function $F(x, y)$, projecting the function onto a line, followed by a one-dimensional Fourier transform is equivalent to taking a slice through the center of the two-dimensional Fourier transform of the function

$$\mathscr{F}_1 \mathscr{P} f(x, y) = \mathscr{S} \mathscr{F}_2 f(x, y). \tag{3.27}$$

Here $\mathscr{F}_1 : \mathbf{R} \to \mathbf{R}$ and $\mathscr{F}_2 : \mathbf{R}^2 \to \mathbf{R}^2$ are the one- and two-dimensional Fourier transforms, respectively, $\mathscr{P} : \mathbf{R}^2 \to \mathbf{R}$ is a projection operator, and $\mathscr{S} : \mathbf{R}^2 \to \mathbf{R}$ is a slice operator. In the special case of circular symmetry, $f(x, y) = f(\rho)$, the projection operator is the Abel transform described above and the right hand side of Eq. (3.27) can be written as the zeroth order *Hankel transform*

$$\mathscr{H} f(\rho) = \int_0^\infty f(\rho) J_0(k\rho) \rho d\rho, \tag{3.28}$$

where J_0 is the Bessel function of the first kind of order zero.

In addition to this, using the fact that the expression for the inverse of the Hankel transform is identical to the transform itself, Eq. (3.27) can be written as

$$\mathscr{H} \mathscr{F} \mathscr{A} f(\rho) = f(\rho), \tag{3.29}$$

where $\mathscr{A}$ and $\mathscr{H}$ are the Abel and Hankel transforms described above. Eq. (3.29) is known as the *Abel-Fourier-Hankel cycle of transforms.* The cycle recreates the original function which in the case at hand is the photoelectron image.

The Abel transform is performed physically in the experiment itself and the subsequent forward transforms are performed in post-processing. Using the cycle of transforms above for inversion provides a stable method which can make use of well tested and optimized routines for Fourier transforms. For noisy images, however, it introduces artifacts and it fails to reproduce sharp features reliably. Under the conditions of the experiments performed in this work, images inverted by the use of Eq. (3.29) are virtually indistinguishable from the direct iterative onion-peeling approach described below.

Onion peeling The Abel inversion routine used in this work is based on the *onion peeling* method[13]. This method assumes that the electron distribution is constant in the radial direction over the size of a pixel. A line can thus be seen as the projection of a finite number of annuli with weight w_i

$$F(x_n) = \sum_{i=1}^{N} w_i F_i(x_n), \tag{3.30}$$

where x_n is the position of the n-th pixel, F_i is the projection of the unit-valued annulus given by

$$f_i(\rho) = \begin{cases} 1, & (i-1)d < \rho \leq id \\ 0, & \text{else} \end{cases} \tag{3.31}$$

where d is the pixel size.

The expression for the projection can be obtained by introducing a function

$$\text{segm}(x, r) \equiv r^2 \arccos\left(\frac{x}{r}\right) - x\sqrt{r^2 - x^2}, \tag{3.32}$$

which describes the area of a circular segment with outer radius r and cutoff distance x.

The projections can then be written as

$$\begin{aligned}
F_i(x_i) &= \text{segm}(x_{i-1}, x_i) \\
F_i(x_{i-1}) &= \text{segm}(x_{i-2}, x_i) - \text{segm}(x_{i-2}, x_{i-1}) - F_i(x_i) \\
F_i(x_{i-2}) &= \text{segm}(x_{i-3}, x_i) - \text{segm}(x_{i-3}, x_{i-1}) - \sum_{j=0}^{1} F_i(x_{i-j}) \\
&\vdots \\
F_i(x_{i-k}) &= \text{segm}(x_{i-k-1}, x_i) - \text{segm}(x_{i-k-1}, x_{i-1}) - \sum_{j=0}^{k} F_i(x_{i-j}) \\
F_i(-x_j) &= F_i(x_j),
\end{aligned} \tag{3.33}$$

examples of which can be seen in Fig. 3.1 for $i = \{8, 16, 32\}$.

Setting N to a number which corresponds to a radius larger than that reached by the most energetic electrons, the weight w_i can be obtained by subtracting the signal from

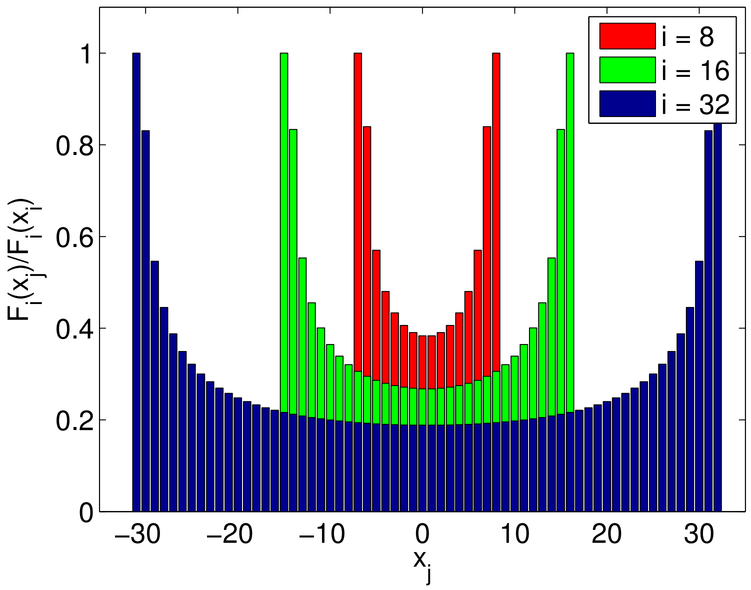

Figure 3.1: Normalized discretized projections for the annuli described by Eq. (3.31)

annuli with a radius larger than $x_n = nd$, iterating inwards from N

$$\begin{aligned} w_N &= \frac{F(x_N)}{F_N(x_N)} \\ w_{N-1} &= \frac{F(x_{N-1}) - w_N F_N(x_{N-1})}{F_{N-1}(x_{N-1})} \\ &\vdots \\ w_i &= \frac{F(x_i) - \sum_{j=i+1}^{N} w_j F_j(x_i)}{F_i(x_i)} \end{aligned} \tag{3.34}$$

in a manner reminiscent of peeling an onion. The value of the reconstructed distribution is then simply

$$f(\rho_i) = w_i. \tag{3.35}$$

The onion-peeling method is reliable and makes no other assumptions but cylindrical symmetry. It is easily implemented in a computer and performs well when compared to the other methods. A drawback is that it tends to oversubtract towards the center of the image, but with sufficient statistics, it reproduces the original distribution at a low computational cost.

3.2.1 Radon transform

In the above treatment of image inversion, the discussion was limited to assuming cylindrical symmetry induced by a linearly or cylindrically polarized laser field. Furthermore, for all the inversion methods intended to produce the Abel inversion of the experimental image, it is necessary for the symmetry axis to be parallel to the detector surface. There is, however, a way to lift this requirement by applying a tomographic method as will be discussed in Chap. 6. The mathematical basis of this method will be discussed in this section, while the experimental details will be laid out in Chap. 6.

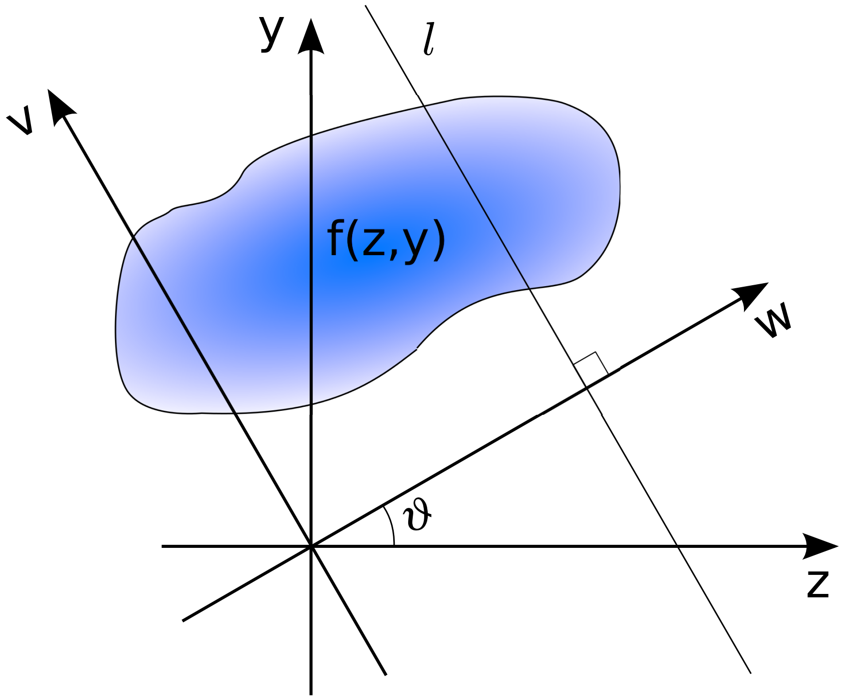

Figure 3.2: Variables needed for the Radon transform. The z-axis is defined by the laser (major) polarization axis. The w- and v- axes are parallel to the detector surface and the projection field, respectively.

Mathematically the projection of a two-dimensional object onto a set of straight lines is described by the two dimensional *Radon transform*. Let $f(z, y)$ be a continuous function on $\mathbf{R}^2$ with compact support and let $\mathbf{L}$ be the space of straight lines in $\mathbf{R}^2$. Then for all $l \in \mathbf{L}$ there exists a parametrization by v as

$$l = \left\{(z(v), y(v)) \in \mathbf{R}^2 | (v \sin\vartheta + w\cos\vartheta, -v\cos\vartheta + w\sin\vartheta\right\} \tag{3.36}$$

where

$$-\infty < w < \infty$$

and

$$0 \leq \vartheta < \pi.$$

w and ϑ are coordinates in $\mathbf{L}$ where w is the perpendicular distance to the line from the origin and ϑ the angle this distance vector makes with the z-axis (see fig. 3.2). With this parametrization, the Radon Transform $\mathscr{R}$ is the transform $\mathscr{R} : \mathbf{R}^2 \to \mathbf{L}$ defined as

$$(\mathscr{R}f)(w,\vartheta) = \int_{-\infty}^{\infty} f\left((v\sin\vartheta + w\cos\vartheta, (-v\cos\vartheta + w\sin\vartheta)\right)\,\mathrm{d}v. \tag{3.37}$$

This is the integral of f along the straight line defined by w and ϑ. A number of formulae for the inverse Radon transform (IRT) exist but the simplest one is given in [65] as

$$f(z,y) = \frac{1}{\pi}\lim_{c\to 0}\int_0^{\pi}\int_{-\infty}^{\infty}(\mathscr{R}f)(w - z\cos\vartheta - y\sin\vartheta, \vartheta)G_c(w)\,\mathrm{d}w\mathrm{d}\vartheta, \tag{3.38}$$

where the convolution kernel G_c is given by

$$G_c(w) = \begin{cases} \dfrac{1}{\pi c^2}, & |w| \leq c \\ \dfrac{1}{\pi c^2}\left(1 - \dfrac{1}{\sqrt{1 - c^2/w^2}}\right), & |w| > c. \end{cases} \tag{3.39}$$

Owing to its frequent use in medical applications, stable, numerical implementations of both the Radon transform and its inverse are readily available. In our experiment, the laser polarization semi-major axis is aligned along the z-axis and the w-axis is defined by the detector plane. The x-axis is defined to be along the laser propagation. This means that we record images in the (x, w)-plane for a series of ϑ values so that every column (i.e. x-position) in the recorded images represent a two-dimensional Radon transform of a slice of the electron swarm. In fact, in the case when the electron swarm has cylindrical symmetry around the z-axis, the central column of the recorded images contains sufficient information to recreate the full electron distribution. In practice, however, this is not always feasible as the count rate for any single column is relatively low under typical experimental conditions.

Chapter 4

Experimental Setup

The following chapter describes the experimental setup used for imaging strong-field photodetachment. Negative ions are produced in a sputter source and accelerated in a beam to a kinetic energy of 4.5 keV. Ultra-short high-intensity laser pulses in the near-infrared regime are created in a femtosecond laser system. The laser pulses are overlapped with the ion beam inside an electron imaging spectrometer which records the angular and momentum distribution of photoelectrons produced through photodetachment.

4.1 Laser System

The laser system used is a commercially available Chirped Pulse Amplified (CPA) titanium-sapphire Clark-MXR CPA-1000 system, capable of producing 800 nm laser pulses with a duration of 100 fs FWHM and with a pulse energy of 1.4 mJ at a repetition rate of 1000 Hz. A schematic of the laser system is shown in Fig. 4.1.

The oscillator consists of a folded 1.875 m cavity containing a Ti:sapphire crystal pumped by a 532 nm diode laser. On startup the cavity operates in continuous wave (CW) mode. Perturbing the cavity slightly introduces longitudinal modes which if their phases match interfere to form a pulse. The pulse has an increased intensity which will cause it to self-focus in the gain medium and be amplified further. This is what is known as *mode-locking*. The output of the oscillator has a pulse length of 100 fs, but the pulse energy is very low at no more than 5 nJ. The center wavelength is 800 nm and the repetition rate is 80 MHz.

Amplification of the short pulse output from the oscillator is not possible as the short pulse duration in conjunction with high intensity would burn the gain medium and optics of the amplifier. The pulse therefore has to be stretched first. The stretcher

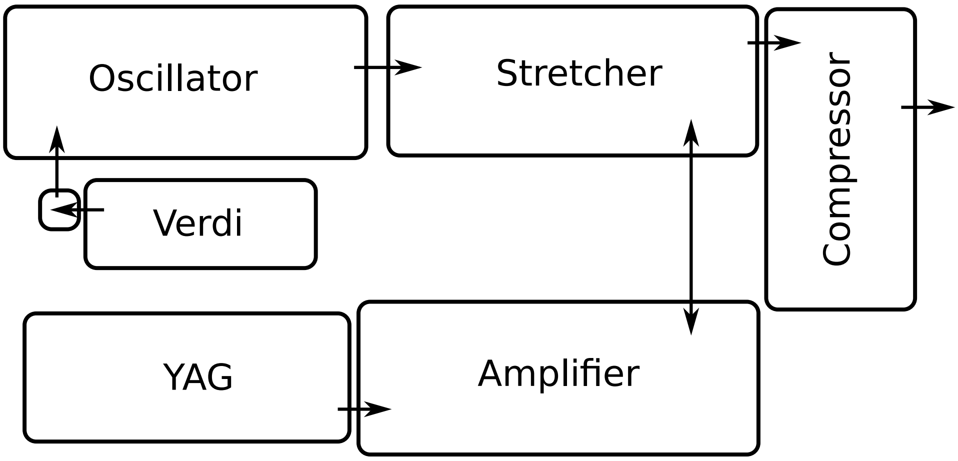

Figure 4.1: Laser system schematic. Description given in the text.

takes advantage of the fact that in order to form a short pulse, it is necessary to have a large spectral bandwidth. For a Fourier-limited Gaussian pulse the relation between the bandwidth ν_{FWHM} and pulse duration t_{FWHM} reads

$$\nu_{\mathrm{FWHM}} = \frac{0.44}{t_{\mathrm{FWHM}}}. \tag{4.1}$$

For a 100 fs pulse with center wavelength 800 nm this corresponds to a minimum spectral width of approximately 10 nm. Under realistic conditions, where some chirp is present, the output of the oscillator has a spectral width of around 15 nm. By using a pair of gratings, the optical path for different wavelengths can be altered to introduce positive *chirp* to the pulse, i.e. the higher-frequency components are made to lag behind the low-frequency components. In this way the pulse length is increased by around a factor of 1000 and the intensity is decreased by the same factor to make it safe for amplification.

The amplifier consists of a Ti:sapphire crystal, pumped by a doubled Nd:YAG at 532 nm, pulsed at 1 kHz with a pulse length and energy of around 250 ns and 7 mJ, respectively. The crystal is placed in a cavity which can be opened and closed by means of a Pockels cell and a polarizer. First, the cavity is opened to let the stretched seed pulse in. The seed pulse is allowed to make around 4 round trips through the gain medium, picking up energy, after which the cavity is again opened to let the amplified pulse out. The output from the regenerative amplifier has a pulse energy of around 1.5 mJ, an increase of a factor of 300000 from the seed pulse.

The final component of the CPA system is a compressor which operates in the reverse manner of the stretcher. The lower frequencies are delayed with the help of a grating to minimize the chirp of the pulse, compressing the pulse back to its original pulse length of 100 fs.

The 800 nm pulses are fed into an OPA (Light Conversion, TOPAS[66]) for frequency conversion. The OPA operates by splitting each pump photon $h\nu_{\text{pump}}$ into two in a non-linear crystal fulfilling the energy conservation condition

$$h\nu_{\text{pump}} = h\nu_{\text{signal}} + h\nu_{\text{idler}}, \tag{4.2}$$

where $h\nu_{\text{signal}}$ and $h\nu_{\text{idler}}$ are the signal and idler outputs, respectively. The output frequencies are determined by phase matching through altering the angle between the laser propagation axis and the optic axis of the crystal. The wavelength range of the OPA output is 1150-2600 nm.

4.1.1 Data acquisition procedure and optics

The signal and idler outputs of the OPA can both be used for experiments either individually or together for pump-probe experiments. The setup facilitating this is pictured in Fig. 4.2. The two beams are separated in a dichroic mirror and led down two different beam paths. Motorized shutters are present in both beam paths for beam selection. The idler beam path contains a motorized delay stage which allows for setting the time delay between pulses in the range [-100,100] ps. The two beams are recombined in a second dichroic mirror. The time zero for the time delay is determined by overlapping the beams in a BBO crystal where they recombine to a wavelength of 800 nm. The direction of the polarization axes of the two beams can be individually controlled through the use of two half-wave plates. To be able to control the focus size as well as to compensate for achromatic aberrations in the focusing lens (not pictured), two telescopes are used. The delay stage, shutters and waveplates are fully computer controlled for automated data acquisition.

4.1.2 Pulse characterization

In order to compare experimental data with simulations it is necessary to characterize the laser pulse to estimate its intensity profile. Assuming a Gaussian profile for the pulse, the temporal and spatial dependence on the intensity is given by

$$I(r,t) = I_{\text{peak}} \exp\left(-4\ln(2)\left(\left(\frac{r}{r_{\text{FWHM}}}\right)^2 + \left(\frac{t}{t_{\text{FWHM}}}\right)^2\right)\right). \tag{4.3}$$

The intensity profile is completely determined by the peak intensity I_{peak} and the pulse duration and focus width, r_{FWHM} and t_{FWHM} respectively.

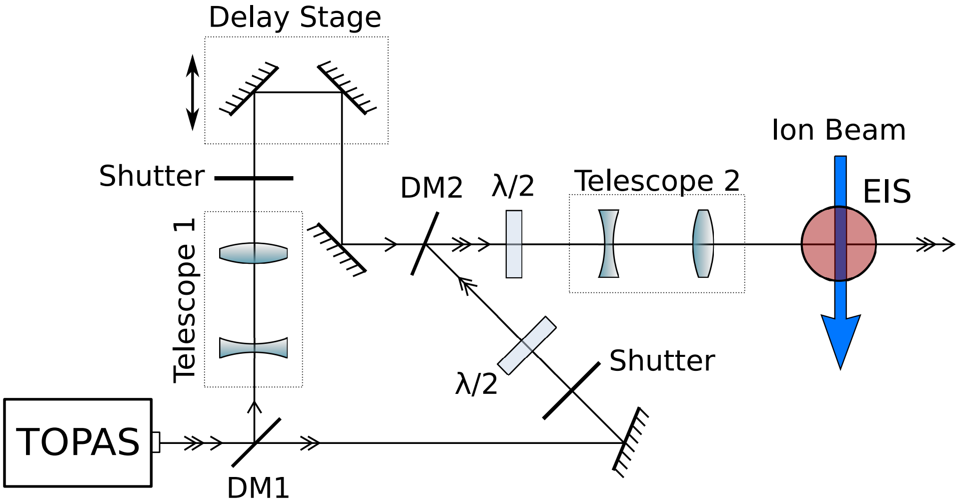

Figure 4.2: Optics for preparing polarization direction as well as time delay for the pump and probe laser pulses. Details are given in the text.

The pulse duration is determined in a single-shot intensity autocorrelator. The autocorrelator, depicted in Fig. 4.3 functions by splitting the pulse into two with a beam-splitter. One of the pulses takes a path with a variable delay before the pulses are made to overlap in a BBO crystal at an angle to each other. The individual pulses are frequency-doubled in the crystal and the produced SHG pulse follows the same beam path independent of the pulse overlap. If the pulses are made to overlap, however, photons produced by combining photons from the two pulses propagate at an angle perpendicular to the focal plane due to momentum conservation. By scanning the time delay, one obtains a signal proportional to the autocorrelation of the pulse intensity

$$R_{\mathrm{II}}(\tau) = \int_{-\infty}^{\infty} I(t)I(t-\tau)dt, \tag{4.4}$$

where τ is the time delay between pulses. For a Gaussian pulse envelope the FWHMs of the intensity and autocorrelation are related by

$$t_{\mathrm{FWHM}} \equiv \mathrm{FWHM(I(t))} = \frac{\mathrm{FWHM(R_{II}(\tau))}}{\sqrt{2}}. \tag{4.5}$$

The radius of the focus is determined by scanning a razor blade over the focus while measuring the power. Assuming a Gaussian shape for the radial geometry and that the razor blade blocks the beam for positions larger than the razor blade position x, the measured power is given by

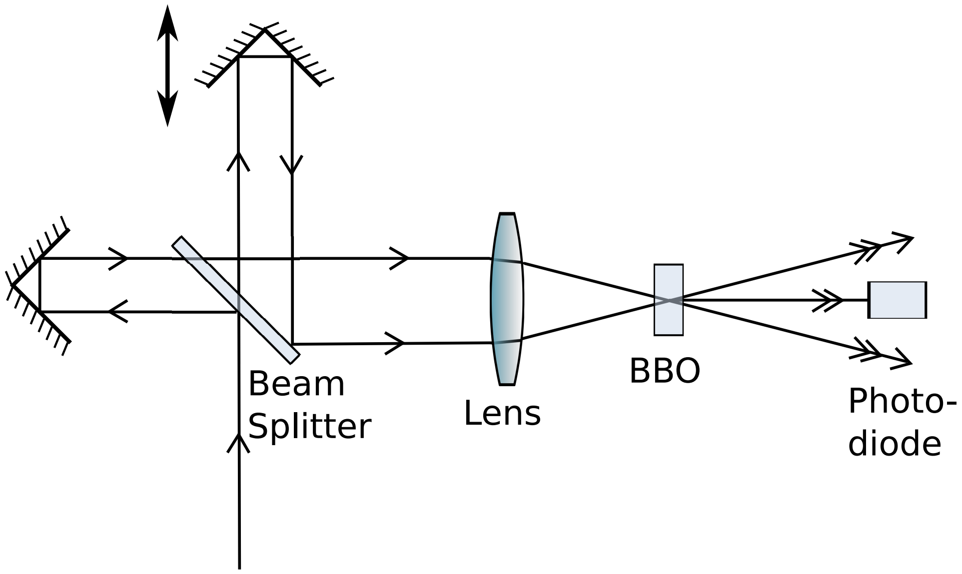

Figure 4.3: Single shot intensity autocorrelator. Description is given in the text.

$$\begin{aligned} P(x) &= P_0 \int_{-\infty}^{x} \exp\left(-4\ln(2)\left(\frac{x'}{r_{\mathrm{FWHM}}}\right)^2\right) dx' \qquad (4.6) \\ &= \sqrt{\frac{\pi}{\ln(2)}}\frac{P_0 r_{\mathrm{FWHM}}}{4}\left(1+\mathrm{erf}\left(\frac{2\sqrt{\ln(2)}\mathrm{x}}{\mathrm{r}_{\mathrm{FWHM}}}\right)\right), \end{aligned}$$

where P_0 is the power of the unblocked beam. By fitting the measured power to Eq. (4.6), r_{FWHM} can be determined.

The peak intensity is determined from the measured power by equating the pulse energy as calculated from the power and as an integral of the intensity

$$\frac{P_0}{n} = 2\pi \int_{-\infty}^{\infty}\int_{0}^{\infty} I(r,t) r dr dt = I_{\mathrm{peak}} \left(\frac{\pi}{4\ln(2)}\right)^{\frac{3}{2}} r_{\mathrm{FWHM}}^2 t_{\mathrm{FWHM}}, \qquad (4.7)$$

where n is the pulse repetition rate, and thus

$$I_{\mathrm{peak}} = \frac{P_0}{n r_{\mathrm{FWHM}}^2 t_{\mathrm{FWHM}}} \left(\frac{4\ln(2)}{\pi}\right)^{\frac{3}{2}}. \qquad (4.8)$$

With the assumptions of the pulse shape above, the pulse characteristics are then determined.

4.2 Ion Accelerator

4.2.1 Sputter source

The negative ion source used in the experimental setup is a commercial cesium sputter source manufactured by Peabody Scientific [67]. Fig. 4.4 shows a simplified schematic of the source. Elemental cesium is heated in an oven (1) to around 150°C. This is far from the boiling point, but it serves to increase the vapor pressure enough to send a thin gas of cesium through a feed tube onto the ionizer coil (2). The tungsten ionizer coil has a current running through it which is typically 19 A which gives it a temperature of around 1200°C. The cesium atoms are ionized by the hot coil, forming Cs^+ ions that are accelerated towards the cathode (3) which is kept at a potential of -900 V relative to the coil, which is kept at a potential of -3.6 kV. The cathode is made out of a copper rod in which a 4 mm deep hole with a diameter of 5 mm has been drilled. A sample containing the element of which negative ions are desired, is placed into the hole, either in solid or compacted powder form. It is necessary for the sample to be sufficiently electrically conductive, something that can be accomplished by adding a small amount of silver powder. Atoms from the thin cesium gas condense on the surface of the sample, forming a thin layer. The sputtered atoms (or molecules) of the sample then have to pass this layer of cesium, which acts as an electron donor, forming the required species of negative ion. The same electric field which accelerated the Cs^+ ions onto the cathode acts to accelerate the negative ions in the opposite direction through the coil to form an ion beam (4) which by the time it reaches the exit port of the sputter source reaches a kinetic energy of 4.5 keV with a typical energy spread of around 10 eV. The source produces mainly monomer negative ions and to a lesser extent dimers. The different species are produced continuously with the same kinetic energy, but can be separated by their different masses and velocities. The source is kept at a vacuum of the order of 10^{-6} mbar.

4.2.2 Ion optics

In the following the ion beam apparatus transporting the ions from the source to the interaction chamber will be described. The apparatus, depicted in Fig. 4.5, consists of three differentially pumped chambers (1), (2) and (3).

Chamber 1 contains an einzel lens (4) and a pair of deflector plates (5) which optimizes the ion beam for passage through a Wien filter (6). The Wien filter produces static electric and magnetic fields which are arranged to be perpendicular to each other and

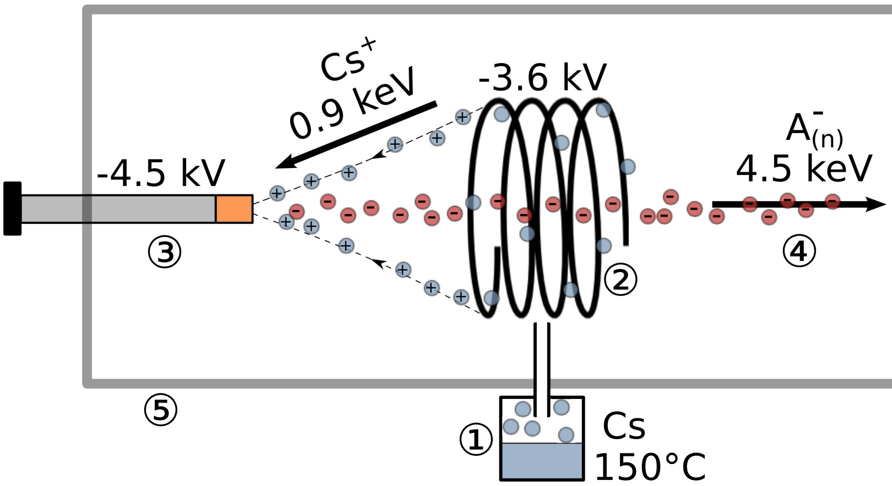

Figure 4.4: Schematic of the cesium sputter source. 1. Cesium oven 2. Ionizer 3. Sputtering cathode 4. Negative ion beam 5. Vacuum chamber

the negative ion beam so that forces are exerted in the direction of the electric field. The magnetic force on the negative ions is linearly dependent on their velocity. By choosing an electric force which balances the magnetic force, mass selection can be achieved according to

$$m = 2E_k \left(\frac{B}{E}\right)^2, \tag{4.9}$$

where m and E_k is the mass and kinetic energy of the ion, respectively, and B and E are the field strength of the electric and magnetic fields. The mass selection is possible because the kinetic energy of the singly charged ions is always the same, and thus they differ in velocity due to their differing masses. The mass resolution of the Wien filter is relatively low but the total resolution is improved by pulsing the ion beam by switching the deflector plates on for 10 μs per laser pulse. Due to the differing velocities for different masses, ionic species arrive in the interaction chamber at a time determined by its mass and can thus be exclusively chosen by an appropriate time delay. The pulsing of the ion beam also serves to extend the lifetime of the phosphor screen in the detector described below, as well as improving the signal-to-background ratio by reducing the amount of electrons formed by collisional detachment in the interaction chamber.

Chamber 2 is used primarily for differential pumping. A turbomolecular pump is connected to the chamber, leaving the residual pressure at around 10^{-7} mbar. The chamber contains horizontal and vertical pairs of deflection plates (7) as well as an einzel lens (8) for optimizing the ion beam path through the quadrupole deflector (9). The quadrupole deflector deflects the ion beam at a 90° angle. This serves to clean out potential neutral particles from the ion beam.

Chamber 3 contains a pair of vertical deflection plates (10) and an einzel lens (11) for positioning and focusing the ion beam into the electron imaging spectrometer (EIS) (12), described in the next section. The ion beam is collected in a Faraday cup (13) placed after the EIS for monitoring the ion current. A typical mass selected ion current is about 100 nA which is about 50% of the current measured directly after the Wien filter.

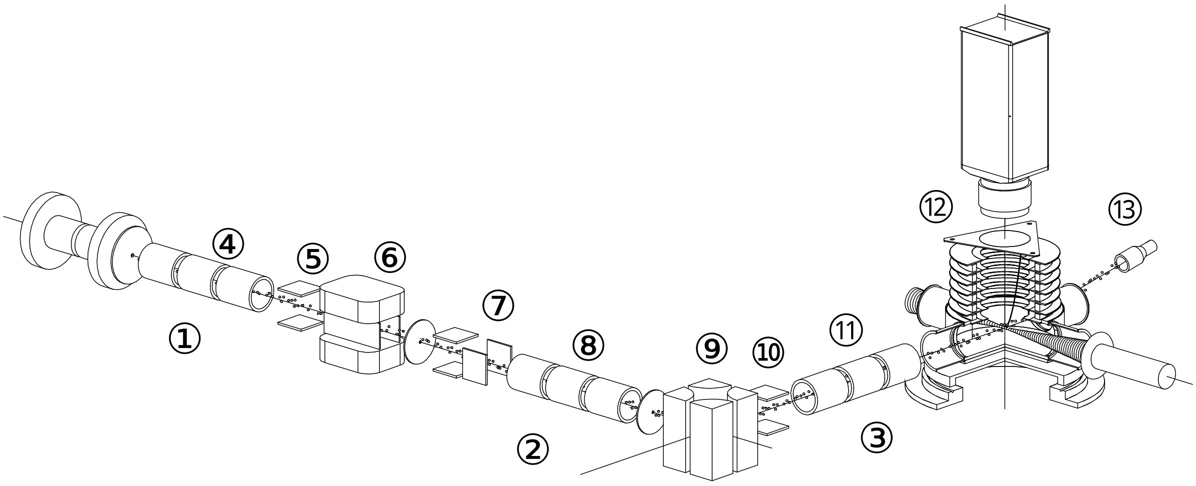

Figure 4.5: Schematic showing the ion beam apparatus. 1. First section 2. Second section 3. Third section 4. Einzel lens 5. Deflection plates 6. Wien filter 7. Deflection plates 8. Einzel lens 9. Quadrupole deflector 10. Deflection plates 11. Einzel lens 12. Electron imaging spectrometer 13. Faraday cup. Figure modified from Ref. [68].

4.3 Electron imaging spectrometer

The ion beam is intersected with the laser beam inside an Electron Imaging Spectrometer (EIS), depicted in Fig. 4.6. The EIS is kept at a vacuum of the order of 10^{-9} mbar by an ion pump. Photoelectrons are ejected in the interaction zone (1). The spectrometer operates by projecting ejected photoelectrons onto a position sensitive detector. The electrons are accelerated onto the detector surface by a nearly homogeneous electric field created by a stack of electrodes (2,3), connected in series by resistors. Electrons with a given momentum modulus p form a sphere which expands during the projection to a radius which is proportional to the electron momentum.

The imaging detector consists of two micro-channel plates (MCPs) (4) in a chevron configuration in conjunction with a phosphor screen (5) and a CCD camera (6). Each individual photoelectron impinging on the MCP stack triggers an avalanche of electrons

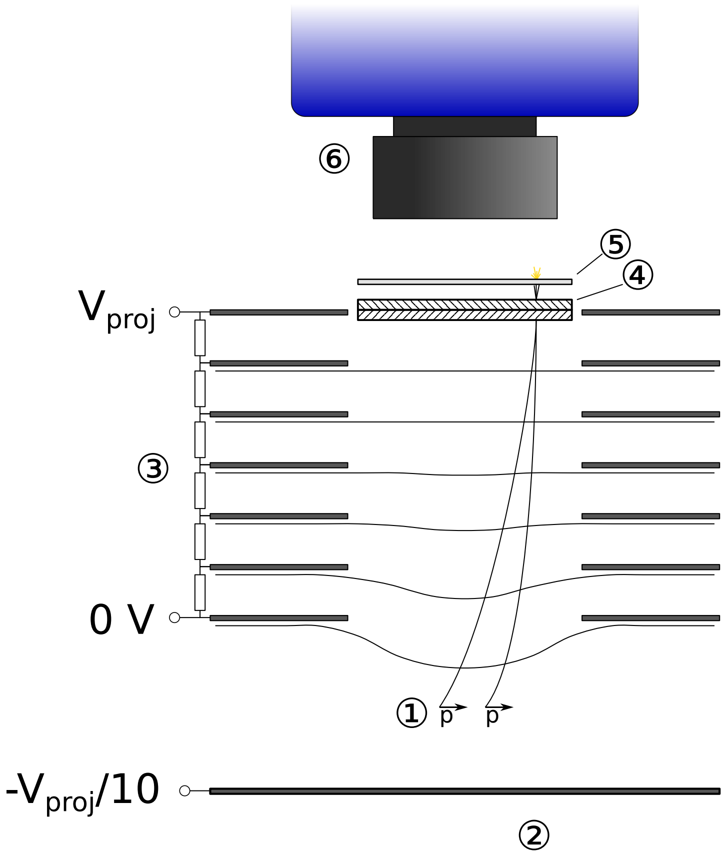

Figure 4.6: Schematic of the Electron Imaging Spectrometer (EIS). 1. Interaction region 2. Extraction electrode 3. Electrode stack 4. MCP stack 5. Phosphor screen 6. CCD Camera.

that are accelerated onto a phosphor screen. On impact of this electron burst, the phosphor screen sends out a flash of light which is recorded by a camera. Collecting data for several seconds produces an image representing a two-dimensional projection of the three-dimensional photoelectron momentum distribution. The three-dimensional distribution can be recreated from the projection using the inversion algorithms described in Sec. 3.2.

Using a high projection field ensures that the projection time is virtually instantaneous to minimize streaking effects due to the ion beam velocity and continued expansion of the electron sphere during the projection. Typically the projection voltage V_{proj} is set to 1600 V producing an electric field of around 27000 V/m. The EIS operates in the velocity mapping regime described in the next section.

In order to not overexpose the CCD camera, for each photoelectron distribution measurement, a series of images with relatively low count rate are recorded. In addition to this a background image with the laser beam blocked is recorded for each partial image and subsequently subtracted so as to eliminate background signal from collisional detachment of the negative ion beam as well as stray photons from laboratory light sources. The partial images are added to form the final image.

In a typical experiment with an ion current of 100 nA, a partial image is acquired by recording photoelectrons and ion beam background for 20 s each in a series of 20 partial images. The number of events in the summed image is of the order of 10^5-10^6.

4.3.1 Velocity map imaging

Using a simple homogeneous projection field (position mapping) limits the resolution of the spectrometer by the volume in which the photodetachment occurs. While the focal radius has a size which is of the same order as the channel size of the MCP and does not significantly limit the resolution, the extension of the focus in the laser propagation direction may have a noticeable effect.

The above problem was solved by Eppink and Parker[14] with a method called velocity map imaging (VMI). The VMI method is implemented by choosing the electrode potentials in such a manner that the projection field acts as an electrostatic lens. This has the result that in a certain plane of the spectrometer, parallel to the detector surface, electrons ejected with the same momentum vector are projected onto the same position on the detector surface, regardless of their initial positions, enhancing the resolution of the detected momentum distribution. Fig. 4.6 shows the lensing effect the projection field has on two electrons ejected with the same momentum vector.

4.3.2 Projection voltage calibration

Operating in the hard projection regime ensures that projection errors are kept to a minimum. There is however a tradeoff with respect to resolution, where a higher projection voltage gives a lower resolution. In cases where the momentum of the ejected electrons is relatively small, having a strong projection field is less crucial and can be reduced for a better momentum resolution. For a homogeneous projection field, the dependence between the projection voltage and the impact position of a photoelectron is straightforward to calculate. For an imaging spectrometer operating in the velocity mapping regime this is not obvious, however. In the following, measurements are performed to verify that the same relation is applicable also in the velocity mapping regime. The imaging spectrometer has previously been carefully calibrated for momentum dependence[54].

It can be shown that for a homogeneous field the radial impact position r on the detector of an electron ejected parallel to the detector surface with momentum p_r is given by

$$r = d\sqrt{\frac{2}{qm}} p_r V_{\text{proj}}^{-\frac{1}{2}}, \tag{4.10}$$

where q and m are the electron charge and mass, d is the distance from the ejection position to the detector surface and V_{proj} is the projection voltage. Using calibration data for the spectrometer obtained at a projection voltage of 1600 V, the relation reads

$$r = 8996 p_r V_{\text{proj}}^{-\frac{1}{2}}, \tag{4.11}$$

where p_r is given in atomic units and V_{proj} is given in volts to obtain the radius in pixels. The relation (4.11) is compared to experimentally obtained values below.

In order to calibrate the projection voltage of the detector, experimental images were obtained for photodetachment of Ag^- at a laser wavelength of 800 nm, requiring a single photon. This is important as that the peak intensity can be kept low to avoid a ponderomotive shift of uncertain magnitude that would decrease the reliability of the calibration data. The transition yields an excess energy of 0.245 eV, corresponding to a momentum of 0.134 atomic units. Images were recorded at projection voltages ranging from 200 to 1600 volts with a step size of 200 V. Fig. 4.7 shows a superimposed image of calibration data obtained at projection voltages 200, 400, 800 and 1600 V. The images have been normalized to their peak values. The experimental images were Abel inverted and a circle was fitted to the maximum of the distribution to determine its radius.

Fig. 4.8 shows the measured radii compared to the relation (4.11). The agreement is very good down to a voltage of 400 volts and stays within one percent of the calculated value. The agreement is not as good at 200 volts, which in part could be because the difficulty of determining the radius because of the lower signal. We conclude that for low electron momenta (4.11) is applicable also in the velocity mapping regime.

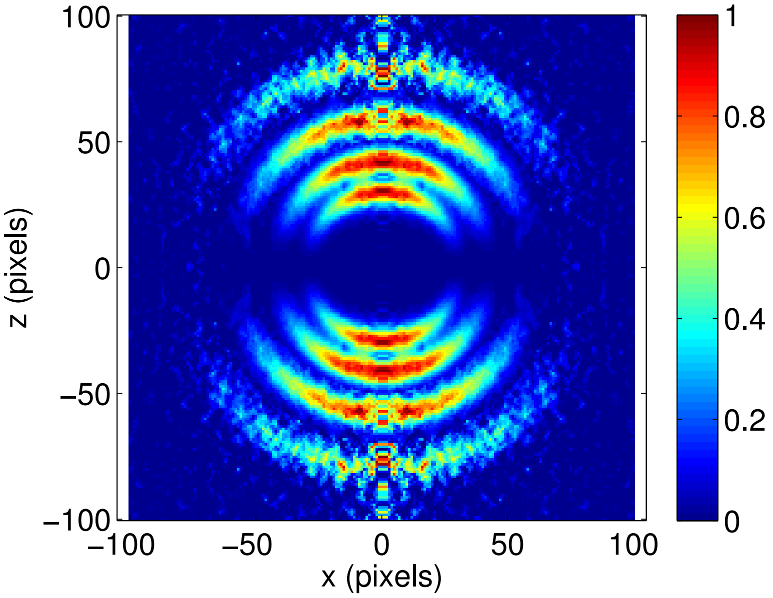

Figure 4.7: Superimposed images of calibration data produced by photodetachment of Ag^- at 800 nm. Images shown were recorded for projection voltages of 200, 400, 800 and 1600 V

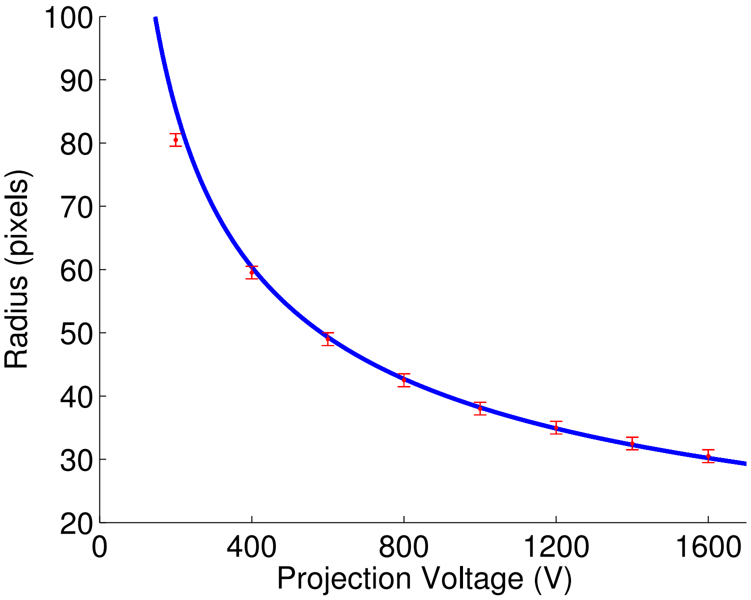

Figure 4.8: Radius of photoelectrons produced by photodetachment of Ag^- at 800 nm for different projection voltages. The blue curve represents the calculated values. Measured data points are shown in red.

Chapter 5

Observation and Simulation of Ground-State Wave Packet Motion in C, Si and Ge

5.1 Introduction

In this chapter a new method, based on an angle-resolved strong-field ionization probe technique, to explore the electron dynamics in carbon, silicon and germanium atoms generated by photodetachment of their respective negative ions in a short laser pulse is described. The development of lasers with pulse lengths of a few femtoseconds has opened up the possibility to study the electron dynamics in atoms and molecules on a time scale of valence-shell electron motion [69, 70, 71]. One interesting effect is the orbital alignment effect that governs electron dynamics in the residual ion produced in the process of ionizing an atom in a strong laser-field. The polarization axis of the external laser field provides a quantization axis for the electron orbital angular momentum and spin. The corresponding projection components m_ℓ and m_s are usually assumed to be conserved during ionization. At high laser intensities the electron tunneling rate is strongly dependent on the magnetic quantum number m_ℓ of the initial state [72, 73]. For a state of non-zero orbital angular momentum and a linearly polarized laser field, the ionization rates from $m_\ell = 0$ substates are typically more than an order of magnitude higher than from $m_\ell \neq 0$ substates. As a consequence, the $m_\ell = 0$ orbital is preferentially ionized and the residual ion is left with a hole in its electron density distribution oriented in the laser polarization direction. This constitutes the orbital alignment effect.

Orbital alignment in laser-generated ions has received a great deal of attention in recent years. The effect was considered by Taïeb *et al.* [74] in an attempt to describe measured photoelectron spectra [75, 76] from multiple ionization of noble-gas atoms in ultra-intense laser pulses. Numerical simulations have shown that the alignment effect plays an essential role in the population dynamics of multiply charged ions during the pulse, since a laser-generated ion represents an aligned target for the subsequent ionization step. However, calculations failed to reproduce the angular distributions of energetic electrons reported in Ref. [76]. The complexity of the problem was addressed with a suggestion to measure higher ionization stages reached at a given peak intensity of the laser pulse. This issue was explored by Gubbini *et al.* [77] by measuring the yields of multiply charged krypton ions as a function of the laser intensity in the range of $10^{16} - 10^{18}$ W/cm^2. Experimental results were analyzed by using the Ammosov-Delone-Krainov theory [72] and by separately considering the possibility of fast and slow alignment relaxation. It was concluded that the relaxation is fast and at each ionization stage the photoemission rate represents a statistical average of rates from the available m_ℓ orbitals. The interaction with the magnetic component of the field and electron-electron correlations were considered as possible mechanisms causing the fast relaxation.

The role of orbital alignment in the process of sequential double detachment of atomic negative ions was discussed by van der Hart [78] on the basis of experimental results presented by Greenwood *et al.* [79]. The measured yields of singly charged positive ions, generated by double detachment, revealed a counter-intuitive behavior of saturation intensities. In particular, double detachment of Ag$^-$ was found to be more strongly saturated than double detachment of Al$^-$, although both the electron affinity and the ionization potential are greater in Ag than in Al. This surprising result was interpreted by van der Hart [78] by considering orbital alignment in the residual atoms generated in the first step of the sequential process and the m_ℓ-dependence of the ionization rate in the second step.

While studies on multiple ionization/detachment brought contradictory results regarding the role of the alignment effect, it was clearly observed in pump-probe experiments on strong-field ionization of Kr in a laser pulse of $10^{14} - 10^{15}$ W/cm^2 peak intensity [80, 81, 82]. The alignment degree of the generated Kr$^+$ ions was measured by employing a synchrotron-based time-resolved X-ray microprobe technique. The frequency of the X-ray radiation was tuned to a resonance with the $1s \to 4p$ absorption transition in Kr$^+$, which is absent in neutral Kr due to the filled $4p$ shell. Since X-ray absorption addresses unoccupied orbitals according to dipole selection rules, the alignment degree could be defined by measuring a difference in the X-ray absorption strength for configurations with the X-ray polarization being parallel or perpendicular to the alignment axis. It was demonstrated that the orbital alignment is preserved on a nanosecond scale and that its decay is caused by the electron-ion collisions in the ionized medium [82]. A detailed interpretation of the results is presented in Refs. [83, 84], where the importance of spin-orbit coupling in the strong-field ionization dynamics is emphasized.

More recently orbital alignment was shown to play an essential role in the electron dynamics induced in the ground state of the residual core by a short laser pulse [30, 29]. The formation of a spatially confined hole in the electron density distribution of the valence shell is a result of coherent population of spin-orbit components of the ground state. For example, for laser-generated positive ions of noble gas atoms, a hole forms in the valence p-shell due to a superposition of the $p^{-1}_{j=3/2}$ and $p^{-1}_{j=1/2}$ manifolds. In order to populate these manifolds coherently, the ionization process is required to be faster than the spin-orbit period of the ground state [84]. Since the wave packet is composed of states having different energies, the created hole shows a time dependent spatial distribution [30]. Different methods have been used to monitor the electronic motion in laser-generated positive ions. These include transient absorption spectroscopy with the use of isolated attosecond extreme-ultraviolet pulses [30] and ionization-probe spectroscopy which includes measurements of the recoil momentum of the doubly charged ion and the total ionization yield [29].

The possibility to initiate and monitor electron motion in the ground state of a neutral atom represents a topic of great interest. By preparing reactive atoms with a desirable electron density distribution one could ultimately achieve control over chemical reactions. In the following the new method is used to investigate orbital alignment and its dynamics in atoms created by photodetachment of negative ions with a half-filled valence p-shell. A detailed description of the experimental method and the setup will be presented.

5.2 Method

A strong-field pump-probe laser scheme is used to investigate the time evolution of orbital alignment in laser-generated carbon, silicon and germanium atoms. The experiment is initiated by photodetaching a valence electron from a negative ion in a strong linearly polarized laser field of short pulse duration. As discussed above, the electron emission in a strong field results in the formation of a spatially oriented hole in the electron density distribution of the residual atom. This alignment is subsequently probed with a second strong laser pulse, applied after a variable time delay, which photoionizes the atom. Since the probe pulse is also strong, it preferentially ionizes the portion of the spatial electron density distribution which is oriented along its polarization axis. By employing an electron imaging technique, this portion is projected onto a position sensitive detector. This makes it possible to visualize the electron density aligned along the polarization axis of the probe pulse and to monitor the motion of the electron cloud in the laser-generated atom. The principle of the strong-field ionization probe technique is described in more detail below.

5.2.1 Principle of the strong-field ionization probe technique

The sensitivity of strong-field ionization to the spatial distribution of the electron density in the bound state can be easily understood for the case when the ionization process is of tunneling character. In this case the valence electron leaves the core by tunneling through a potential barrier created by the superposition of the external field and the core potential. Since the potential barrier is well localized along the field polarization direction, only the part of the electron density which is oriented along this direction can tunnel through the barrier and consequently determines the ionization yield.

A similar selectivity of ionization to the electron density orientation also takes place in the multiphoton regime of this process. This can be shown using a theory based on the strong field approximation (SFA) (see Sec. 2.3). The theory is proven to successfully describe the processes of strong-field photodetachment and ionization [85]. Following the analysis in [54] of the predictions by the SFA theory, the n-photon differential ionization rate in the laser field $\mathbf{F}(t) = \mathbf{F}\cos(\omega t)$ can be represented by the product of the amplitude and the interference terms (atomic units, $e = m = \hbar = 1$, are used throughout):

$$\frac{dw_n}{d\Omega} \propto \left| P_\ell^{|m|}\left(\sqrt{1 + p^2 \sin^2(\theta)/\kappa^2}\,\right) \right|^2 \frac{p\; e^{-2a}}{|S''_{t_1}|^2} \times \left(1 + (-1)^{\ell+m}\cos(b - \beta)\right). \tag{5.1}$$

Here p is the photoelectron momentum, θ is the emission angle with respect to the laser polarization axis, $P_\ell^{|m|}$ is a Legendre polynomial, (ℓ, m) are the orbital angular momentum and magnetic quantum numbers of the electron in the initial state, $-\kappa^2/2 = E_0$ is the initial binding energy, $a = \mathrm{Im}(S_{t_1}) = \mathrm{Im}(S_{t_2})$, $b = S_{t_1} - S_{t_2}$, $\beta = 2\arg(S''_{t_1})$, and S_{t_1,t_2} are the values of the coordinate-independent part of the classical action

$$S(t) = n\omega t - \frac{\mathbf{F}\cdot\mathbf{p}}{\omega^2}\cos(\omega t) - \frac{F^2}{8\omega^3}\sin(2\omega t) \tag{5.2}$$

calculated at the transition instances t_1 and t_2 that lie in the upper half-plane of complex time t and satisfy the saddle-point condition [46]

$$(\mathbf{p} + (\mathbf{F}/\omega)\sin(\omega t_{1,2}))^2 = 2E_0\ . \tag{5.3}$$

Eq. (5.1) immediately shows that only the $m = 0$ orbital contributes to emission along the laser polarization axis, since at $\theta = 0$ the argument of the Legendre polynomial is equal to 1 and $P_\ell^{|m|}(1) = 0$ for $|m| \neq 0$. We derive below that in the limit of a large number of absorbed photons, $n \gg |E_0|/\omega$, the amplitude term in Eq. (5.1) confines the angular distribution of photoelectrons into a narrow cone oriented along the polarization axis. Since the Legendre polynomial is multiplied by the amplitude term, the $m = 0$ contribution remains dominant in this limit.

Considering the multiphoton regime, $\kappa\omega/F \gg 1$, one can use the expansion introduced by Gribakin and Kuchiev [46]:

$$c_{1,2} \simeq -i\, s_{1,2} + \frac{i}{2s_{1,2}} + O(s_{1,2}^{-2}) \ , \tag{5.4}$$

where $c_{1,2} = \cos(\omega t_{1,2})$, $s_{1,2} = \sin(\omega t_{1,2})$, and $|s_{1,2}| \gg 1$. The latter inequality is due to the fact that the complex values of t_1 and t_2 have a large imaginary part. Retaining only the leading terms in calculations of S_{t_1,t_2}, we obtain the following expression for the amplitude term in Eq. (5.1)

$$\frac{p\ e^{-2a}}{|S''_{t_1}|^2} = f(\theta)\,\frac{\omega p}{2n}\left(\frac{F^2}{8\omega^3 n}\right)^n \exp\left(n + \frac{p^2}{\omega}\right) \ , \tag{5.5}$$

where the dependency on the emission angle θ is factorized as

$$f(\theta) = \frac{\exp\left(-(p^2/\omega)\sin^2(\theta)\right)}{\kappa^2 + p^2\sin^2(\theta)} \ . \tag{5.6}$$

In the limit $n \gg |E_0|/\omega$ the value of $p^2/\omega \sim 2n$ is large and the exponential term in Eq. (5.6) dominates the angular distribution of photoelectrons. This restricts the distribution to a small angle $\Delta\theta \approx (2\ln 2/n)^{1/2}$ (FWHM), which decreases with the increase of n. For example, the emission is confined to $\Delta\theta \approx 14^\circ$ at $n = 25$ and to 10° at $n = 50$. The number of photons needed to overcome the ionization potential was disregarded in these calculations. The denominator in Eq. (5.6) becomes important in the limit $p^2 \gg \kappa^2$, i.e. when the electron kinetic energy is orders of magnitude larger than its initial binding energy. One can easily see that the denominator term results in an additional narrowing of the angular distribution. Such a high-energy condition, however, is not reached in the present study.

Thus, we obtain that the product of the Legendre polynomial and the amplitude term in Eq. (5.1) results in the selectivity of ionization to the $m = 0$ orbital and, consequently, to the electron density orientation along the polarization direction. This selectivity is stronger at higher kinetic energies, where the angular distribution of emitted electrons is narrow and forms two electron jets along the laser polarization axis [85]. Thus, by imaging the photoelectron yield in the high-energy jets we directly probe the electron density in the bound state along the laser polarization axis. In this energy range the interference term in Eq. (5.1) is not essential. Indeed, it was shown before that at $\theta = 0$ the interference term oscillates on the $1/p$ scale [54]. Its oscillation period is defined by the energy of the initial state and the laser frequency and is independent of the laser intensity. The first maximum of this oscillation from the side of high electron momenta defines the position of the maximum signal in the electron jet. The interference term does not oscillate within the jet and, therefore, can be disregarded in our consideration.

The high-energy jets can be easily distinguished in the angle resolved spectra of photoelectrons, as will be demonstrated in our results. It should be noted that under the conditions of the present experiment the dominant ionization is in the multiphoton regime, when the condition $\kappa\omega/F \gg 1$ is satisfied. Despite the high peak intensity of the probe laser pulse, the main contribution to the ionization yield is defined by lower intensities due to the integration of signal over the spatiotemporal intensity distribution in the laser focus and due to the saturation effect. This matter was discussed in detail in Ref. [85].

5.3 Experimental procedure

The ion beam apparatus used in this experiment is described in detail in Chap. 4. A beam of negative ions was generated using a sputter ion source. A graphite rod was used as cathode material to produce C^-, whereas powder of silicon and germanium was used when Si^- and Ge^- ions were generated. The ion beam was accelerated to a kinetic energy of 4.5 keV and mass selected in a Wien filter. Einzel lenses, a quadrupole deflector and deflection plates were used to steer and focus the ion beam into an electron imaging spectrometer (EIS), where it was intersected by the focused laser beams. The waist of the ion beam inside the spectrometer was approximately 1 mm and the ion current measured after the spectrometer was of the order of 100 nA. The pressure in the interaction region was of the order of 10^{-9} mbar.

The EIS consists of a set of electrodes that project electrons emitted from the laser focus in the entire solid angle onto a microchannel plate detector equipped with a phosphor screen [54]. The light pulses from the screen, generated by the detected electrons, were recorded with a 1280x1024 pixels CCD-camera. Millions of single electron counts, accumulated during a CCD exposure time of the order of 10 min, composed a statistically significant image. In order to reduce the image distortions, the EIS was operated in the velocity mapping regime[14] with a hard projection voltage of 1.6 kV. In this regime electrons having the same momentum vector $\mathbf{p}$ are projected to the same point on the position-sensitive detector of the EIS independent of initial position in the interaction region.

Laser pulses were generated using an optical parametric amplifier (OPA) pumped with a mode-locked Ti:sapphire laser system at a repetition rate of 1 kHz. The linearly polarized idler (2055 nm) and signal (1310nm) outputs from the OPA were used as the pump and probe beams, respectively. The long pump wavelength was chosen in order to reach a higher degree of non-linearity of the photodetachment process. This reduced the saturation of this process at the leading edge of the pump pulse. As a consequence, the negative ions were exposed to higher laser intensities. The binding energies of C^-, Si^-, and Ge^- are 1.26212, 1.38952, and 1.23271 eV, respectively [86]. At the chosen pump wavelength of 2055 nm, the photon energy is 0.6 eV which means that for photodetachment of these negative ions absorption of at least three photons is required. The probe pulse has a wavelength of 1310 nm, i.e. a photon energy of 0.95 eV.

A schematic drawing of the optics setup is presented in Fig. 4.2. The signal and idler beam outputs of an OPA were separated using a dichroic mirror (DM1). Their polarization axes were controlled by means of two $\lambda/2$ wave plates. The time delay between the pump and probe pulses was varied by changing the optical path length of the pump beam with the use of an optical delay stage. The divergence of the pump beam was controlled using a telescope installed in its beam path. This was used to make the focal points of the two laser beams to longitudinally coincide inside the interaction region. The two laser beams were merged using a second dichroic mirror (DM2). The merged beams were expanded and focused into the interaction region with the use of a second telescope placed in front of the experimental chamber. Focal sizes of 30 μm (FWHM) and 17 μm (FWHM) for the pump and probe pulses, respectively, were measured by scanning a razor blade across the laser foci. The pulse duration of both beams was 100 fs (FWHM). The pulse energies of the pump and probe pulses were 150 and 240 μJ, yielding peak intensities of the order of 1×10^{14} and 7×10^{14} W/cm^2, respectively.

Substantial efforts were made to ensure that the foci of the laser beams were on top of each other at their intersection with the ion beam. The spatial beam overlap was regularly controlled during the experiment by monitoring replicas of the foci with a CCD camera. This was performed by inserting a glass wedge into the beam path in front of the experimental chamber, where the beam reflections from the front wedge surface were guided into the camera (not shown in Fig. 4.2). The larger focus size of the pump beam and saturation of the photodetachment process facilitated maintaining the condition where the probe beam interacts mainly with neutral atoms created in the aligned state. The target ions moved over a negligible fraction of the focal size during the time between the pump and probe pulses.

The zero time delay between pulses was determined by optimizing the yield of their sum-frequency generation in a thin BBO crystal inserted in the beam path. The accuracy of setting the time delay to zero was of the order of 50 fs. Thereafter, the BBO crystal was removed and the delay line was adjusted to the desired time delay. All data presented in this work were acquired with time delays larger than 600 fs. This ensured that the two laser pulses were completely separated in time, hence avoiding interference between the two coherent laser pulses.

The data acquired in the experiment is the angle and momentum resolved images recorded with the CCD camera of the EIS. The experimental goal was to measure the yield of high energy electrons emitted along the polarization axis of the probe laser, as it was described in the previous section. To make this possible, the probe polarization was kept parallel to the detector plane, making the required angular and momentum resolved measurement possible. However, the time delay between the pump and probe laser pulses was much shorter than the time resolution of the detector. This prevented direct discrimination of electrons produced in the photodetachment step. In order to obtain an image of only the photoionized electrons, which reveals the density distribution in the aligned atom, an additional image was recorded for the pump pulse alone and subtracted from the image recorded with both pulses. The acquisition of the two images was done in alternating sequences of 10 seconds by blocking and opening the probe laser beam with a shutter.

The probe pulse monitors the electron density distribution in the direction of its own polarization axis, whereas the pump polarization defines the axis of orbital alignment in the atom. The alignment effect was observed with a higher signal-to-background contrast by subtracting the image of ionized electrons obtained with the pump polarization parallel to the probe polarization (the latter was kept parallel to the detector plane) from the image recorded with perpendicular polarization axes. Finally, the difference of the images was normalized to their sum. This serves to compensate for variations in laser intensity and ion current. The entire image processing can be represented as

$$Q = \frac{Q_\perp - Q_\parallel}{Q_\perp + Q_\parallel} \, , \tag{5.7}$$

where $Q_\perp$ and $Q_\parallel$ denote images of ionized electrons obtained with the perpendicular and parallel arrangements of the pump and probe polarizations, respectively. The signal value in the normalized image Q, averaged over a chosen range of high kinetic energies and small emission angles (see the following section), is used to quantify the alignment degree in the laser-generated atoms.

5.4 Results

Owing to the dynamics of the orbital alignment after the pump pulse, the signal distribution in the normalized image Q introduced in Eq. (5.7) is dependent on the time delay between the pump and probe pulses. A sequence of images for different time delays was recorded in order to monitor the dynamics. To identify the area of interest, i.e. the area where the yield of high-energy electrons reveals the alignment degree in the residual atom, an average over the different settings of the pump-probe delay was formed.

Figs. 5.1, 5.2 and 5.3 show normalized images of these averaged images of ionized electrons for C, Si, and Ge, respectively. The images are the cylindrically symmetric 3D distributions of ionized photoelectrons projected onto the detector plane. The symmetry axis, which coincides with the laser polarization axis, is vertical in the figure. The radial distance from the image center is proportional to the electron momentum in the detector plane, and the coordinates $p_{\|}$ and $p_{\perp}$ represent the momentum components along and perpendicular to the laser polarization axis, respectively. The calibration of the momentum scale is described in [54] and in Sec. 4.3.2.

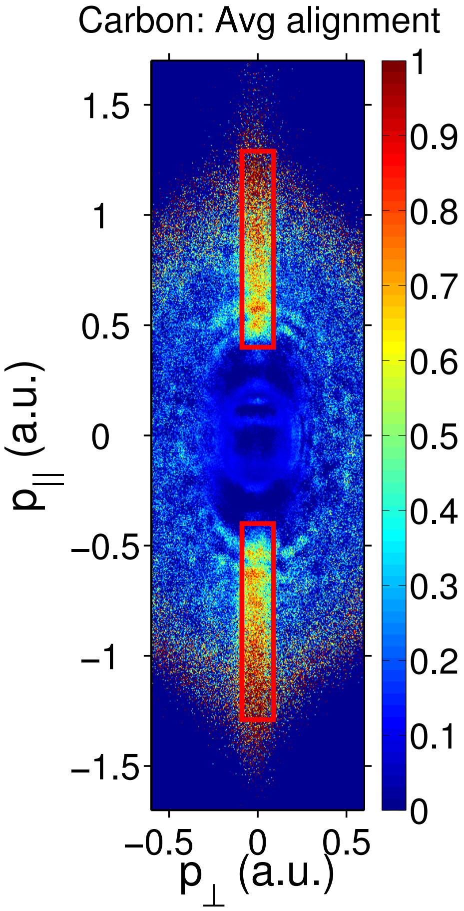

Figure 5.1: Normalized images of electrons produced by photoionization of neutral carbon averaged over the entire range of the pump-probe time delay. $p_{\|}$ and $p_{\perp}$ denote the electron momentum components parallel and perpendicular to the polarization axis of the probe beam, respectively. The area of interest in the jet region, used in the data analysis, is outlined by the red rectangle.

Each distribution shown in Figs. 5.1–5.3 exhibits two opposing narrow jets along the laser polarization axis. The jets are the most pronounced in the carbon image, where

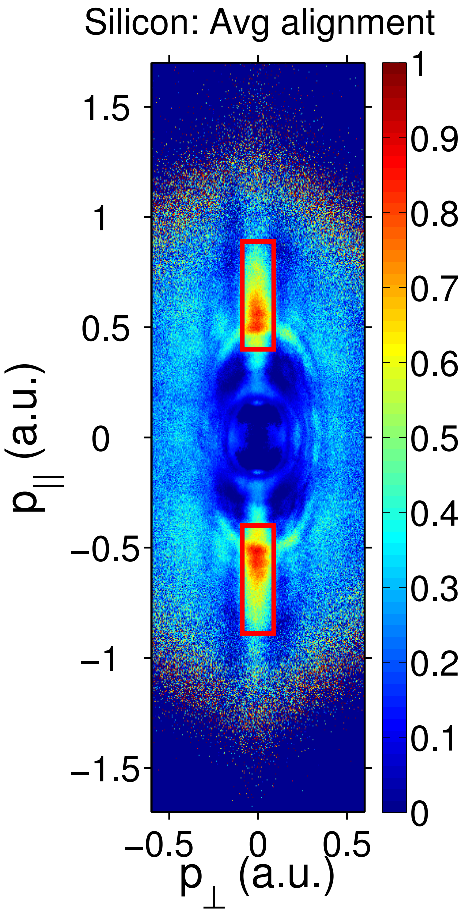

Figure 5.2: Normalized images of electrons produced by photoionization of neutral silicon averaged over the entire range of the pump-probe time delay. $p_{\|}$ and $p_{\perp}$ denote the electron momentum components parallel and perpendicular to the polarization axis of the probe beam, respectively. The area of interest in the jet region, used in the data analysis, is outlined by the red rectangle.

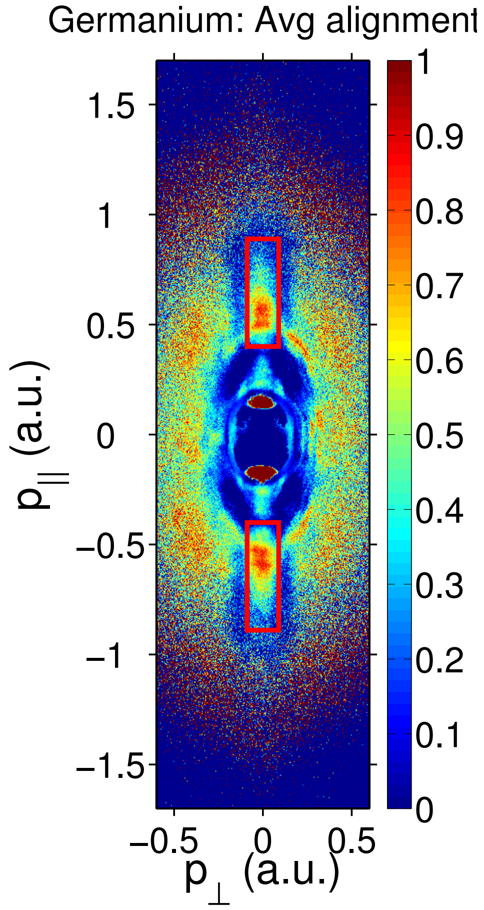

Figure 5.3: Normalized images of electrons produced by photoionization of neutral germanium averaged over the entire range of the pump-probe time delay. $p_{\|}$ and $p_{\perp}$ denote the electron momentum components parallel and perpendicular to the polarization axis of the probe beam, respectively. The area of interest in the jet region, used in the data analysis, is outlined by the red rectangle.

they extend to electron momenta of approximately 1.5 atomic units (a.u.). This value corresponds to the absorption of more than 30 photons above the ionization threshold of C at the laser wavelength of the pump beam. Thus, the value of p^2/ω in the exponential term of Eq. (5.6) is large and, as it follows from the analysis of this equation, the selectivity condition of ionization to the electron density distribution in the bound state is satisfied. The jets are also well pronounced in the silicon image, but to a smaller extent than for carbon. The prominence of the jets is smaller in the germanium image, which immediately implies that the time-averaged alignment degree in the laser-generated Ge atom is smaller than for C and Si.

In order to reconstruct the angle and momentum resolved distribution of photoelectrons from a raw image recorded by the CCD camera, it is necessary to apply an inversion routine, e.g. "onion peeling" (see Sec. 3.2). However, such a procedure introduces noise concentrated at the symmetry axis of the inverted image. This is in the region of small emission angles, which also is the region of the image where the orbital alignment dynamics can be observed. We have therefore refrained from carrying out the inversion routine. Instead, the data analysis presented below involves integration of the signal in the jet regions of the non-inverted images. The areas of integration, outlined in red in Figs. 5.1–5.3, are chosen to account for the total signal of jet electrons while avoiding the background contributions from surrounding areas. The integrated yield is used as a measure of the orbital alignment degree in the direction of the probe pulse polarization.

Fig. 5.4 shows three representative images obtained for carbon at fixed pump-probe time delays of 2000 fs, 2300 fs, and 2600 fs, respectively. One should note that the normalization routine introduced in Eq. (5.7) significantly improves the contrast between the signal in the jets and the signal in the image center, where the yield is dominated by low energy electrons produced via photodetachment by the probe beam of negative ions that survived the pump pulse. The three chosen time delays lie within a spin-orbit period of the ground ^3P state of the C atom, which represents an intrinsic time scale of electron dynamics in this state. This matter will be discussed in more detail below. The experimental results presented in Fig. 5.4 clearly reveal the time dependence of the spatial distribution of the electron density in the laser-generated carbon atom. Following the pump pulse, the electron hole in the valence shell starts its evolution. The hole orientation interchanges between being localized along and perpendicular to the quantization axis defined by the pump pulse polarization. Fig. 5.4a represents the case where the hole is oriented in the direction of the probe polarization axis and, therefore, the signal in the jet region is absent. In contrast, Fig. 5.4c shows an image where the jets are most pronounced. In this case the hole is localized at 90° with respect to the probe polarization axis and, thus, the electron density has a maximum along the direction of the probe field. Fig. 5.4b represents an intermediate case.

For the quantitative analysis of the alignment dynamics in C, Si, and Ge, the ionization

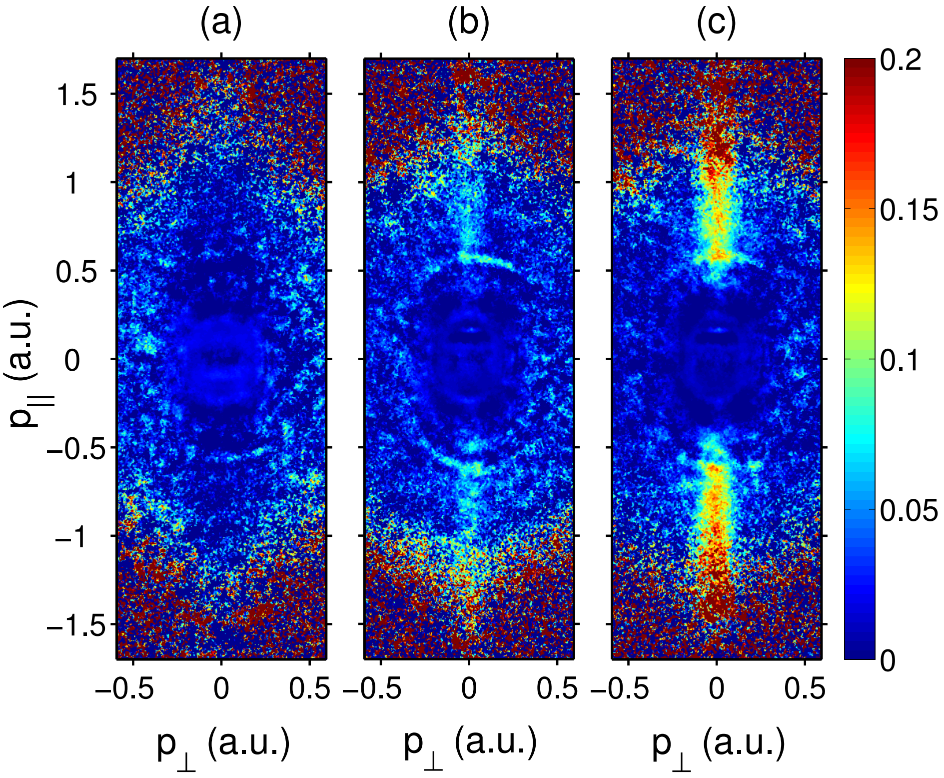

Figure 5.4: Normalized images of ionized electrons obtained for carbon at a fixed pump-probe time delay of 2000 fs (a), 2300 fs (b) and 2600 fs (c).

signal in the normalized images was integrated over the areas of interest outlined in Figs. 5.1–5.3. The obtained time dependencies of the integrated yield in the jet regions are shown in Figs. 5.5–5.7, where the time scale represents the pump-probe delay. In the carbon experiment, the time delay was varied between 600 and 5000 fs. Shorter ranges from 950 to 2200 fs and from 600 to 780 fs were investigated for Si and Ge, respectively. In each case the chosen delay range covers several spin-orbit periods of the ground ^3P state of the atom. The oscillations in the carbon and silicon data shown in Figs. 5.5 and 5.6 clearly demonstrate the dynamics of the orbital alignment initiated in these atoms by the pump pulse. It can also be seen that, apart from the time-dependent behavior, the alignment degree has a constant offset. In germanium (Fig. 5.7) the data shows a constant alignment but there is no clear sign of a temporal oscillation.

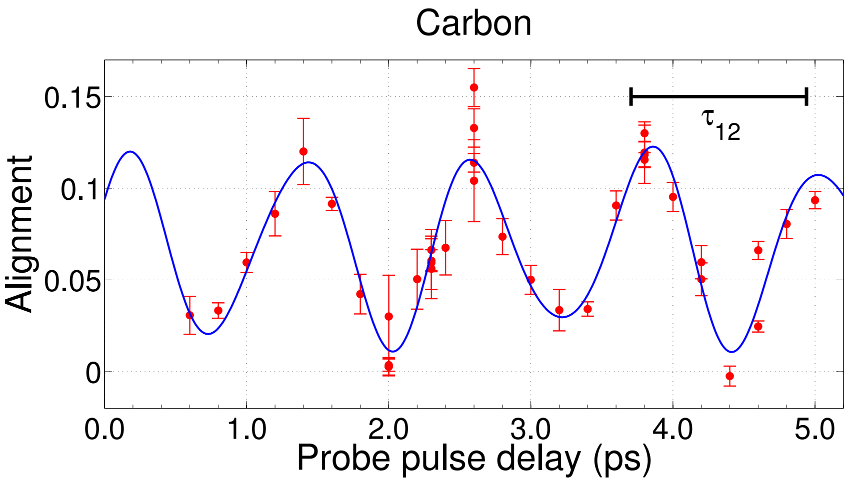

Figure 5.5: The normalized yield of high-energy electrons emitted in the ionization step for carbon plotted as a function of the time delay between the pump and probe pulses. The yield is integrated over the areas of interest in the jet region shown in Fig. 5.1. The solid blue curve represents the fit result of Eq. (5.8) to the experimental data. The horizontal bar represents the predicted beat period τ_{12} between the $J = 1$ and $J = 2$ spin-orbit sublevels of the atomic ground state.

5.5 Data analysis and discussion

As it was pointed out in the introduction, the orbital alignment dynamics in the laser-generated atom manifests as the time evolution of a coherently excited wave packet formed by a superposition of atomic bound states. The three elements considered in the present work have isoelectronic p^2 configurations of the ground state, giving rise to the ^3P, ^1D, and ^1S terms [87]. Their negative ions have a p^3 $^4S_{3/2}$ electron configuration in the ground state [86]. Since spin conservation does not allow photodetachment transitions from a quartet state to a singlet state, the laser-generated C, Si, and Ge atoms can only be created in the triplet ^3P ground state. Thus, the alignment dynamics observed in carbon and silicon is due to a coherent population of the three fine structure components of the ^3P state characterized by the total angular momentum $J = 0$, 1, and 2. A depiction of the involved states is shown in Fig. 5.8 for the case of carbon.

It follows that the time evolution of orbital alignment is governed by a quantum beat between three coherently populated states. The time period τ of the beat of two coherent states is given by $\tau = h/\Delta E$, where ΔE is the energy separation between the states involved, and h is the Planck constant. In our case the three populated fine structure components give rise to three possible beat periods denoted by τ_{01} $(J = 0, 1)$, τ_{02} $(J =$

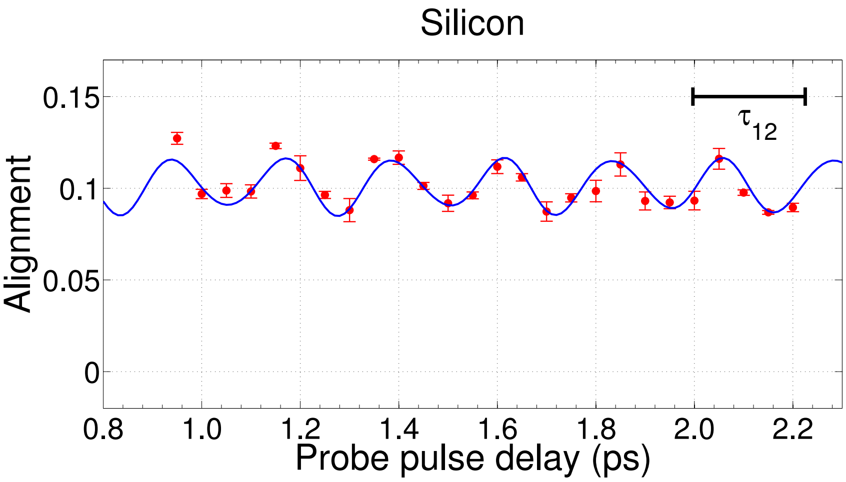

Figure 5.6: The normalized yield of high-energy electrons emitted in the ionization step for silicon plotted as a function of the time delay between the pump and probe pulses. The yield is integrated over the areas of interest in the jet region shown in Fig. 5.2. The solid blue curve represents the fit result of Eq. (5.8) to the experimental data. The horizontal bar represents the predicted beat period τ_{12} between the $J = 1$ and $J = 2$ spin-orbit sublevels of the atomic ground state.

$0, 2)$ and τ_{12} $(J = 1, 2)$. The fine structure energy splittings ΔE_{FS} taken from Ref. [87] and the spin-orbit (beat) periods calculated from $\tau = h/\Delta E_{FS}$ are presented in Table I. Thus, as mentioned above, the spin-orbit periods of the ^3P ground state represent the intrinsic time scale of the electron dynamics in laser-generated C, Si, and Ge atoms.

Due to the three possible beat periods, a phenomenological function

$$f(t) = \alpha_0 + \sum_{i=1}^{3} \alpha_i \cos\left(\frac{2\pi}{\tau_i}(t - t_0)\right), \tag{5.8}$$

containing the sum of three harmonic functions was fitted to the data sets shown in Figs. 5.5, 5.6, and 5.7 for carbon, silicon, and germanium, respectively, with α_0, α_i, τ_i, and t_0 being the fit parameters. Here α_0 represents a constant offset and α_i are the amplitudes of oscillations with the individual beat periods τ_i. While the time delay is measured between the maxima of the pump and probe pulses, we cannot experimentally determine the instance at the leading front of the pump pulse where the detachment process is saturated, nor the instance during the probe pulse where the ionization yield is maximum. Because of this uncertainty and the limited accuracy in the determination of the zero time delay, the fit parameter t_0 is introduced in Eq. (5.8).

The fit results of Eq. (5.8) to the data sets are represented by the solid lines in Figs. 5.5–

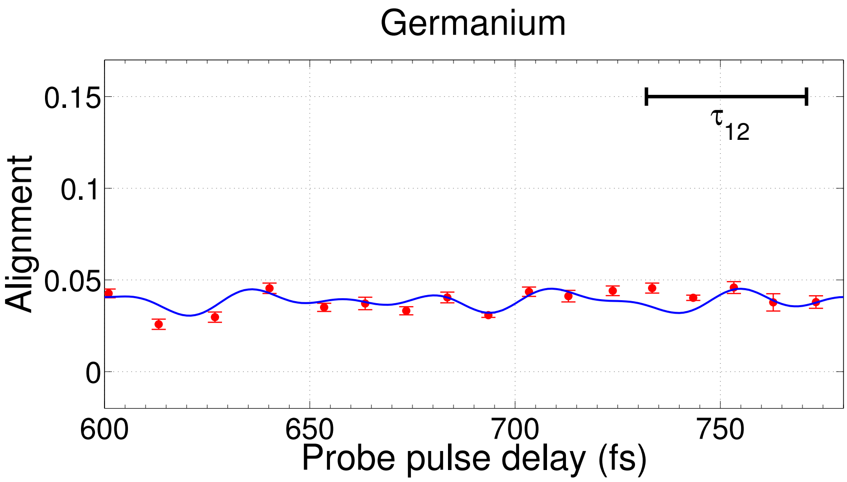

Figure 5.7: The normalized yield of high-energy electrons emitted in the ionization step for germanium plotted as a function of the time delay between the pump and probe pulses. The yield is integrated over the areas of interest in the jet region shown in Fig. 5.3. The solid blue curve represents the fit result of Eq. (5.8) to the experimental data. The horizontal bar represents the predicted beat period τ_{12} between the $J = 1$ and $J = 2$ spin-orbit sublevels of the atomic ground state.

5.7, and the obtained fit parameters τ_i and α_i are given in Table I. The fit to the experimental data for Ge produced statistically nonsignificant values for the beat amplitudes (see Table I). For completeness, these results are shown in Fig. 5.7, but will not be discussed further. It can be seen from the amplitude parameters α in Table I that for both C and Si the alignment dynamics is dominated by the beat J_{12} between the $J = 1$ and $J = 2$ components of the ^3P state. This can be explained by considering that the multiplet levels are populated according to their statistical weights $2J+1$ and, thus, the weights of the $J = 1$ and $J = 2$ states are the highest. The fit results closely reproduce the calculated periods for the J_{12} beat in C and Si (see Table I). Considering the J_{01} and J_{02} beats, the uncertainties in the obtained amplitude values make the fit results statistically nonsignificant.

The results obtained from the fit can be verified by carrying out a Fourier analysis of the temporal dependencies shown in Figs. 5.5–5.7. Such an approach was already implemented by Höhr *et al.* in the study of orbital alignment in laser-generated positive ions [82]. A discrete Fourier transform routine was applied to the data set for Si. The obtained results are plotted in Fig. 5.9 as a function of the Fourier frequency, ν_F. The Fourier spectrum exhibits a distinct peak at the frequency that corresponds to the τ_{12} beat period, indicated by the arrow in the figure. All other maxima in the spectrum are artifacts of the transform since the transform is conducted using only 26 temporal

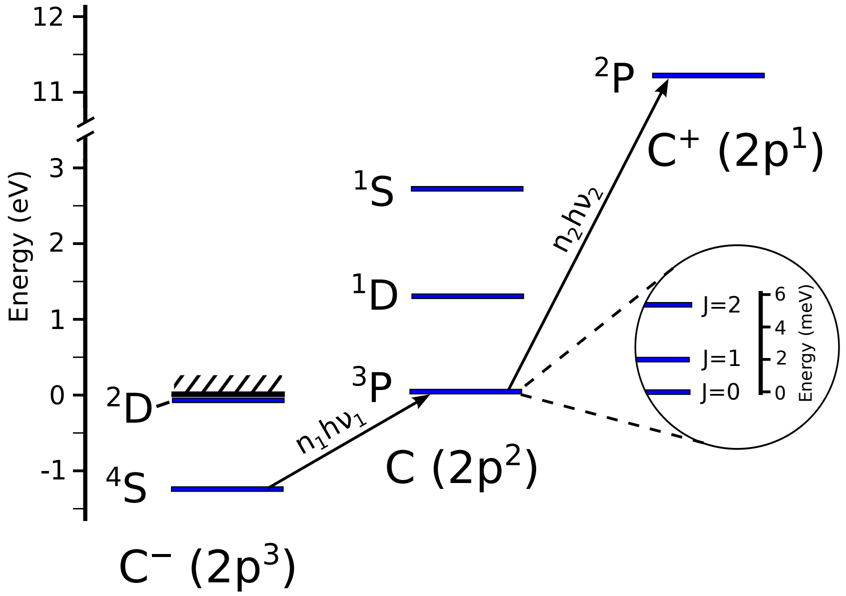

Figure 5.8: Energy levels involved for the neutral as well as the negative and positive ions of carbon. The arrows indicate strong-field photodetachment and ionization. The fine-structure states of the ground state of the neutral are shown inside the circle.

points. A larger number of experimental data points with a higher density on the time scale are needed to improve the signal-to-noise ratio in the Fourier spectrum.

The present study demonstrates a dramatic decrease in the coherence degree of orbital alignment with the increase of the fine structure energy splitting of the ground atomic state. This result is associated with the particular laser pulse duration of 100 fs used in the experiment. Such a pulse length is approximately one order of magnitude shorter than the spin-orbit period in the ground state of carbon. Therefore, the strong temporal modulation in the ionization yield is observed in this case (see Fig. 5.5), which is a result of the temporal rearrangement of the electron density distribution due to coherent population of the spin-orbit sublevels of the ground state. In contrast, no clear modulations are visible in the temporal dependency obtained for germanium (see Fig. 5.7). Simulations show that the interval during which photodetachment occurs has a FWHM

	Beat	ΔE_{FS} (meV)	τ_{cal} (fs)	τ_{exp} (fs)	α (10^{-3})	α_0 (10^{-3})	t_0 (fs)
C	J_{01}	2.033	2034	2239±308.5	-3.69±3.52	67.7±2.6	179.9±33.8
	J_{02}	5.381	768.6	756.4±15.6	7.81±3.94		
	J_{12}	3.348	1235	1216±15	48.2±3.3		
Si	J_{01}	9.5610	432.6	410.9±25.0	-1.32±1.93	101.8±1.4	51.4±21.6
	J_{02}	27.6679	149.5	143.6±2.8	1.83±2.80		
	J_{12}	18.1069	228.4	222.9±3.0	13.9±1.9		
Ge	J_{01}	69.07582	59.87	59.38±2.88	2.22±2.59	38.6±1.8	-3.3±30.7
	J_{02}	174.81286	23.66	24.06±1.07	-2.92±3.03		
	J_{12}	105.73704	39.11	38.81±1.72	3.56±2.54		

Table 5.1: Fine structure splittings ΔE_{FS} [87], calculated beat periods τ_{cal}, measured beat periods τ_{exp} and amplitudes α of the quantum beats in C, Si, and Ge. The uncertainties represent one standard deviation. The two rightmost columns show the fit values for the constant offset α_0 and the time t_0 in Eq. (5.8).

of around 50 fs. This is larger than the period of the main beat τ_{12} in germanium, which leads to a non-coherent population of its fine structure sublevels. It should be noted that the probe pulse duration plays an important role as well, since the ionization step duration defines the time resolution in the observation of electron motion. As previously mentioned, the pump and probe pulses have the same length in the present experiment.

The three temporal dependencies of the ionization yield shown in Figs. 5.5–5.7 for C, Si, and Ge exhibit a constant positive offset, represented by the parameter α_0 in Eq. (5.8). It implies that the mean value of the electron density in the laser-generated atom is larger in the direction perpendicular to the pump polarization axis than in the parallel direction. This constitutes the orbital alignment effect of non-coherent character, which was observed in the experiments on strong-field ionization of noble gas atoms [80, 81, 82] and described in Refs. [83, 84]. In this case the population of a given spin-orbit state can be considered independently of other channels. The degree of the stationary alignment depends on the intensity-dependent admixture of photodetachment from the $m_\ell \neq 0$ substates of the negative ion, which is averaged over the spatiotemporal intensity distribution in the laser focus.

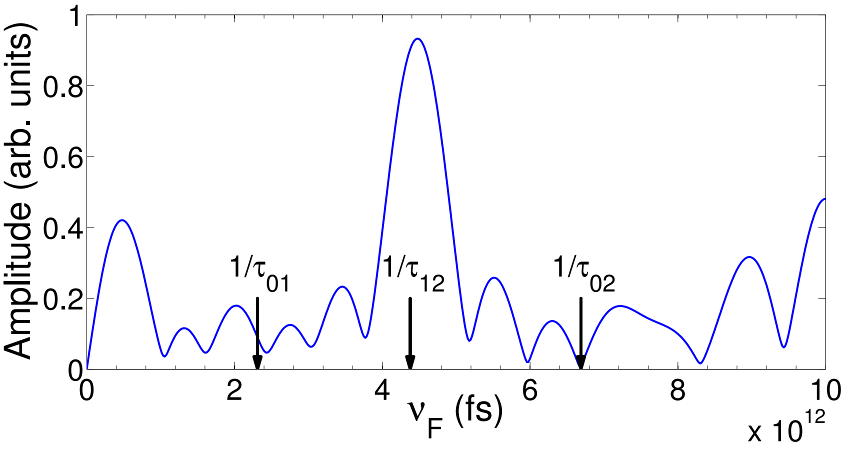

Figure 5.9: The Fourier transform of the measured time dependency of the ionization yield of Si shown in Fig. 5.6. Note that the abscissa is inversely proportional to the Fourier frequency ν_F. The vertical arrow indicate the beat period calculated from the tabulated energy splitting of the $J = 1$ and $J = 2$ spin-orbit components of the ground state of the Si atom.

5.6 Simulation

A theoretical model for the beat can be constructed using the density matrix description of the process presented in section 3.1.1. By populating a density matrix coherently using the differing detachment rates for p-orbitals with zero and non-zero magnetic quantum number m_ℓ, the time evolution of the electron density distribution in the neutral atom can be calculated. Similarly, the m_ℓ dependent ionization rates are used to determine the total ionization rate. A full pulse strong-field simulation as described in section 3.1 using the laser parameters of the experiment was used to estimate the ratio between detachment from an m_ℓ zero and non-zero state. The detachment rate ratios are found to be 26.2, 19.9 and 32.2 for carbon, silicon and germanium, respectively, and the corresponding ionization rate ratios are 6.25, 3.63 and 3.57.

Figures. 5.10-5.12 show the simulations for the three atomic species of the ionization rates as a function of the pump-probe delay. The blue curves ($Q_\perp$) represents the ionization rate where the pump and probe polarizations are in a perpendicular configuration and the green ($Q_\parallel$) represent a parallel configuration. The red curves (Q) are the normalized ionization rates corresponding to Eq. (5.7). The red dots is the experimental data from the previous section. Note that the experimental data has been scaled and offset to have the same amplitude and mean value as the simulation. This is necessary due to the background signal in the experimental data. It can be seen that for carbon and silicon the simulations agree well with what was obtained in the experiment. For germanium the model shows a significant oscillation which is not present in the experimental data. This is due to the assumption in the model that detachment and ionization is instantaneous. In reality the duration of the photoprocess is around 50 fs. On the intrinsic time scales of carbon and silicon this instantaneity assumption is justifiable, but in the case of germanium the model fails. It is interesting to note that even with the assumption of an instantaneous photoprocess, the simulation shows a constant offset of the normalized ionization rate, implying that an orbital alignment of constant character is achieved also in this case.

In a recent paper by Rey *et al.*[88], a model for ionization of carbon in an orbitally aligned state was developed. The authors used a time-dependent R-matrix theory to describe the process and they used the experimental data presented in this chapter for comparison to calculations of the wave function time evolution. The results show a remarkable resemblance to the simple model used in this work. A recently developed analytical expression by Gribakin[89] giving the ionization rate based on the assumption that solely $m_\ell = 0$ electrons are detached in both photoprocesses, shows a similar result.

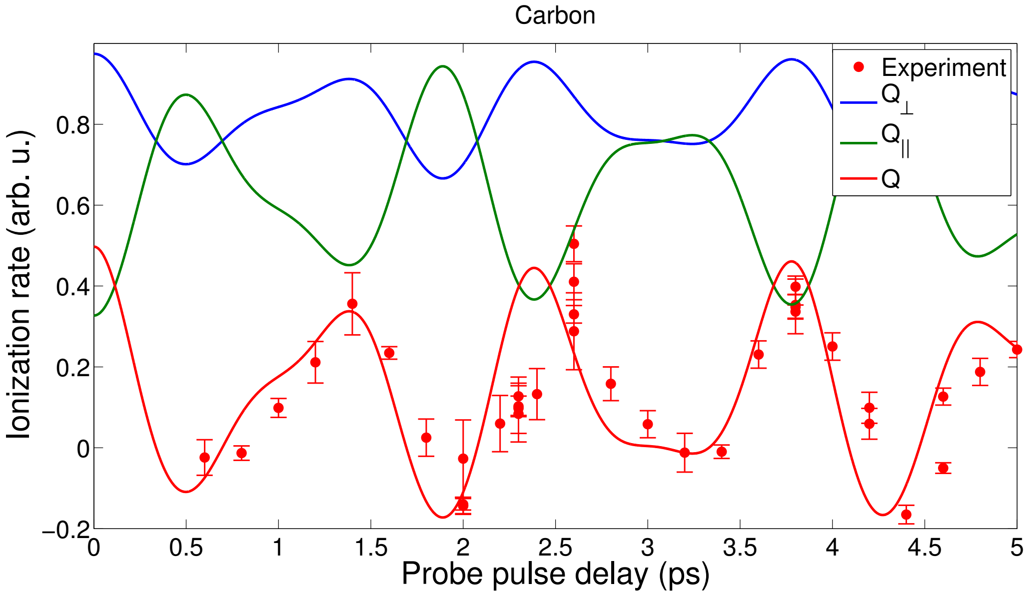

Figure 5.10: Simulated ionization rates for neutral carbon atoms prepared in an aligned state by a pump pulse at time zero as a function of the probe delay. The blue curve ($Q_\perp$) represents the case when the polarization of pump and probe are kept perpendicular and the green ($Q_{||}$) a parallel configuration. The red curve represents the alignment measure Q from Eq. (5.7). The red dots with error bars represent experimental data.

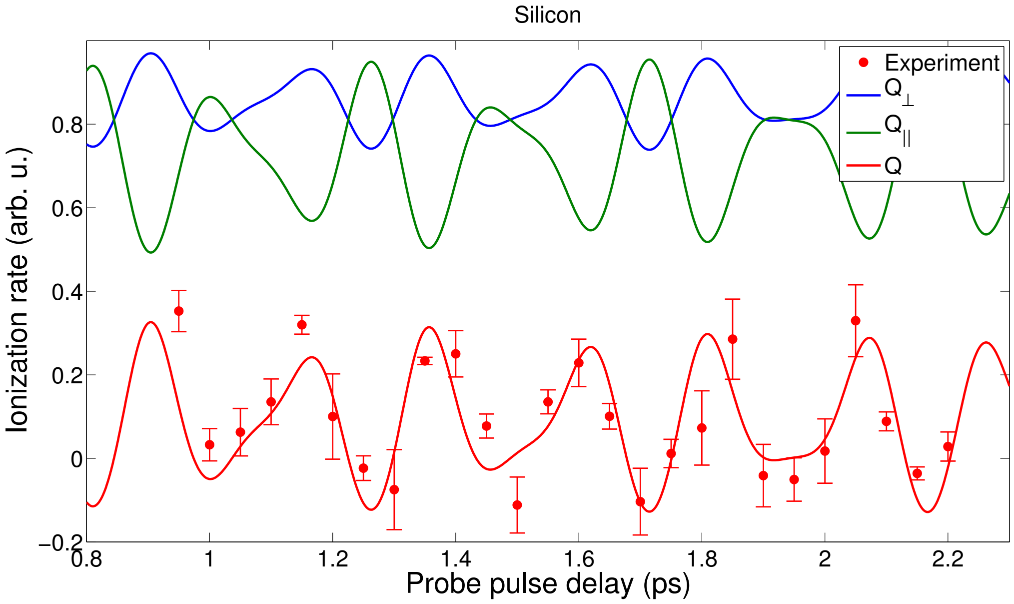

Figure 5.11: Simulated ionization rates for neutral silicon atoms prepared in an aligned state by a pump pulse at time zero as a function of the probe delay. The blue curve ($Q_\perp$) represents the case when the polarization of pump and probe are kept perpendicular and the green ($Q_{||}$) a parallel configuration. The red curve represents the alignment measure Q from Eq. (5.7). The red dots with error bars represent experimental data.

5.7 Summary

A strong-field pump-probe laser scheme was used to reveal the dynamics of orbital alignment in atoms generated through photodetachment of their negative ions. The alignment dynamics are shown to acquire a coherent character when the time scale of the photodetachment process is shorter than the spin-orbit period of the atomic ground state. In this case the alignment effect is associated with a coherent population of spin-orbit components of the ground state. It results in a spatial confinement of the electron density distribution in the residual atom that periodically changes in time. The coherence condition was fulfilled in the experiment on C^- and Si^-, which permitted the observation of electron motion in the ground state of laser-generated carbon and silicon atoms. Simulations using a density matrix approach was shown to be in good agreement with the experimental data in these cases. When the spin-orbit period is shorter than the time of photodetachment, the coherence condition is lost and the orbital alignment in the residual atom has a stationary character. This case was realized in the experiment on Ge^-. These results are in accordance with the predictions by Rohringer and Santra [84], who described the alignment effect in the process of strong-field ionization of noble

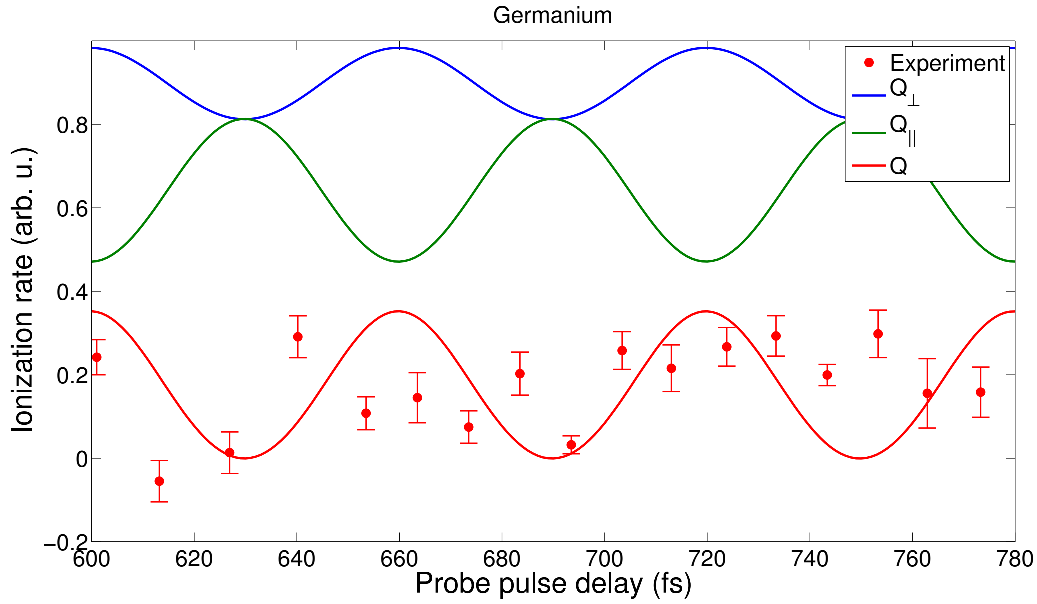

Figure 5.12: Simulated ionization rates for neutral germanium atoms prepared in an aligned state by a pump pulse at time zero as a function of the probe delay. The blue curve ($Q_\perp$) represents the case when the polarization of pump and probe are kept perpendicular and the green ($Q_{||}$) a parallel configuration. The red curve represents the alignment measure Q from Eq. (5.7). The red dots with error bars represent experimental data.

gas atoms.

The present work addresses orbital alignment in atoms possessing two electrons in the outer p-shell. Despite the complexity of the electronic structure of these atoms, which includes three spin-orbit components of the ^3P ground state, the study reveals that only two state components of the highest statistical weight contribute significantly to the alignment dynamics. We believe that this result remains valid for atomic systems with higher multiplet orders of the ground state. Further experiments, however, are needed to verify this.

A detailed interpretation of the strong-field ionization probe method that allows monitoring the electron density angular distribution in bound atomic states has been given. Its principle is based on the fact that the portion of electron density localized along the probe field polarization is mapped by the strong field to a jet of outgoing energetic electrons. The angular resolution of this method is increasing with the increase of kinetic energies of ejected photoelectrons. The developed probe technique has a general character and is not restricted to neutral atoms. It can also be used to test angular distributions of electron densities in other (charged) atomic or molecular systems.

To conclude, a method to initiate and to monitor electron motion in the ground state of a neutral atom has been developed. It opens a wide range of applications, where coherent control over a process can be achieved by preparing the reactive atom in its ground state with a desired electron density distribution. With the use of a laser pulse of 100 fs duration the coherence condition can be achieved in light elements, where the intrinsic time scale of electron motion lies in the picosecond range. Shorter pulses are needed to achieve coherent control in heavier atoms.

Chapter 6

Tomography of Electron Emission Patterns

6.1 Introduction

Electron imaging has become a ubiquitous tool in recording the momentum and angular distribution of electrons emitted in photoionization and photodetachment processes. Imaging methods are also used for recording the distributions of heavy charged particles which emerge from laser-induced processes. In its simplest implementation, the imaging method relies on projecting the emerging charged particles onto a planar detector using an external electric field. Linearly polarized light produces a rotationally symmetric spatial distribution around the polarization axis. For circularly polarized light, on the other hand, a rotationally symmetric spatial distribution appears around the laser propagation axis. In both cases a position sensitive detector located in a plane parallel to these distinguished axes can be used to record an image of charged particle impacts which is twofold symmetric, with one symmetry axis along the distinguished axis and and one along an axis perpendicular to it.

When fulfilling the criterion that the kinetic energy gained in the projection field E is much larger than the excess energy from the photo process W, it is possible to rely on inversion routines such as the Inverse Abel Transform (IAT) (see Sec. 3.2) to transform the 2D image on the detector into 3D information of the spatial electron distribution in the atomic or molecular frame.

In general situations a more elaborate analysis is required. This, for example, concerns the case when elliptically polarized light is used, or in experiments aimed at complete characterization of photoionization[90], or in experiments where the photoelectron energy is affected by different ponderomotive acceleration parallel and perpendicular to the laser beam [91]. Furthermore, when electron emission is preferentially parallel to the laser polarization (such as is generally the case in strong electromagnetic fields) conventional inversion routines produce distortions since single-image inversion implies the accumulation of inversion error along the axis of symmetry. The more elaborate analysis requires images at different orientations of the polarization vector. In its most general implementation this is achieved by tomographic imaging as described in a recent paper by Smeenk *et al.*[31].

Here it is shown that tomographic imaging is of great use in standard imaging experiments as it allows circumventing problems associated with imperfect acceleration fields, spatial inhomogeneity of the detector, and is capable of inverting complex continuous energy distributions. This is demonstrated using minimum two and three photon detachment of Ag^- ions for which theoretical model calculations exist that can be compared one-to-one with the tomographic imaging method.

6.2 Experimental setup

The experimental setup is shown in Fig. 4.5. Ag^- ions are formed in a cesium sputter source, accelerated to 4.5 keV, and mass selected in a Wien filter. Einzel lenses are used to focus the ion beam in the interaction region, where the beam waist is 1 mm at a flux of 27 nA. The 90° bend in the quadrupole serves to clean the negative-ion beam from neutral atoms formed by collisional detachment in the first two vacuum sections. Three differentially pumped sections maintain a residual pressure of the order of 10^{-9} mbar in the interaction region. Laser pulses with a wavelength of 1310 and 2055 nm with a pulse energy of 60 and 30 μJ, respectively, both with a pulse length of 130 fs full width at half maximum, are generated in an optical parametric amplifier pumped by a Ti:sapphire laser system at a repetition rate of 1 kHz. The laser beam is focused by a lens with 20 cm focal length and crosses the ion beam at a right angle. The intensity distribution in the laser focus is measured by scanning a razor blade across the focus. The shape of the pulses can be described well by a Gaussian profile with a waist of 27 and 44 μm FWHM, yielding peak intensities in the laser focus of the order of 5.3×10^{13} W/cm^2 and 9.6×10^{12} W/cm^2 for the 1310 and 2055 nm pulses, respectively. The central part of the setup is an electron imaging spectrometer, which projects electrons emitted in the entire solid angle onto a two-dimensional position sensitive detector by an electrostatic field. The position sensitive detector consists of two image-quality micro-channel plates in chevron configuration and a homemade phosphor screen, coated on a glass plate with a transparent conductive gold layer. The light flashes from the phosphor screen are recorded by a CCD array with 12-bit resolution where they are accumulated and read out to a PC at intervals of a few seconds. The spectrometer is operated in the velocity mapping regime (see Sec. 4.3.1). The last vertical pair of steering plates compensates the small deflection of negative ions towards the detector surface by the projection field of the imaging spectrometer. This ensures a nearly horizontal beam path across the laser focus, which is an important requirement in order to suppress asymmetry of the photoelectron image. Residual electron background is reduced by pulsing the ion beam with 10 μs on and 990 μs off for each laser shot period. This switching also acts as an additional mass filter due to the different times of flight of different atomic and molecular species. Additionally, the voltage over the MCPs is reduced in the period between laser pulses in order to further reduce background noise. Under typical operating conditions about 5 events per laser shot are recorded. Distortions by space charge effects do not occur at such low electron yields.

Images suitable for tomography are obtained by rotating the laser polarization in step sizes of 3 degrees using a stepper motor-driven half-wave plate and recording images for 25000 laser shots at each position of the half-wave plate. The recorded images are used to reconstruct the three-dimensional photoelectron distribution using the inverse Radon transform (IRT) described in detail in Sec. 3.2.1.

6.3 Results

In this section, experimental data obtained from photodetachment of Ag^- (EA(Ag) = 1.30447 eV[92]) as well as a comparison to theory is presented. Measurements were made at laser wavelengths of 1310 nm ($h\nu = 0.94644$ eV) and 2055 nm ($h\nu = 0.60333$ eV). The ground state of Ag^- has two $5s$ electrons in its valence shell. Figures 6.1 and 6.2 show a comparison between theory and experiment for 1310 nm and 2055 nm, respectively. The figures show the angle-resolved electron momentum distribution which is obtained by integrating the full 3D distribution along the azimuthal angle ϕ. The theoretical electron distributions were calculated by simulating strong-field photodetachment by means of the strong-field approximation as described by Gribakin and Kuchiev [46]. The theory and simulation procedure is described in detail in Chaps. 2 and 3. For the 1310 nm case, a clear EPD structure is visible with 2, 3, 4... photon detachment signals at momenta $p \approx 0.187, 0.311, 0.397....$ Theory reproduces all the main features of the experiment although it overestimates the 3 photon detachment yield along the polarization axis so that it is observed to be more intense than the 2 photon process. For the 2055 nm case, the electron distribution shows less pronounced EPD peaks due to the lower detachment rate, allowing the ions to survive to higher intensities. Here theory also agrees well with the experiment, although the jet along the laser polarization axis is more intense in the experiment. The simulation procedure takes the spatio-temporal intensity distribution into account. The theoretical electron distribution is subject to the same processing as the experimental data to make sure that any distortion induced by the inversion is also present in the simulated data. The only noticeable inversion artifact is the slight distortion at an emission angle of 45 and 135 degrees.

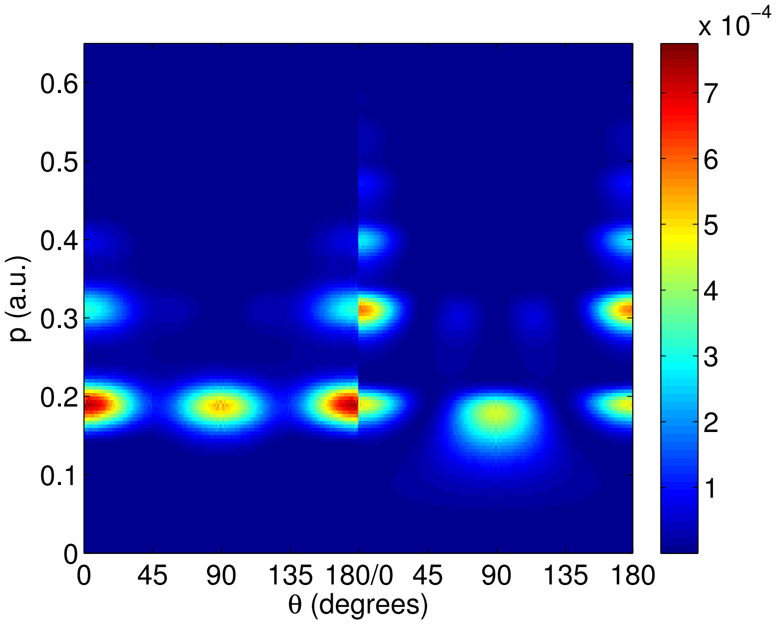

Figure 6.1: Comparison of experiment (left) and using the theory of Gribakin/Kuchiev (right) of the photoelectron momentum distribution for detachment of Ag^- at 1310 nm. The figure is in polar coordinates where θ is the angle to the laser polarization axis.

6.4 Discussion

One advantage of using the inverse Radon transform (IRT) instead of the inverse Abel transform (IAT) to recreate the electron distribution, even in the case of an experiment using linear laser polarization, is that the latter introduces distortions along the polarization axis. The IAT is also sensitive to finding the left-right center of the image. For a strong-field experiment, it is in general the case that the area of interest lies along the polarization axis. In Refs. [93, 94], for instance, we refrained from performing the Abel inversion because of the distortions it might introduce. The inverse Radon transform on the other hand, is completely insensitive to centering the image in the x-direction (parallel to the laser propagation axis) and is instead sensitive to centering w (perpendicular to the laser propagation axis). For a long jet along the linear polarization axis (z-axis), however, centering w can be done with higher precision than centering x. (For a description of the mentioned coordinate axes, see Sec. 3.2.1 and Fig. 3.2 in particular)

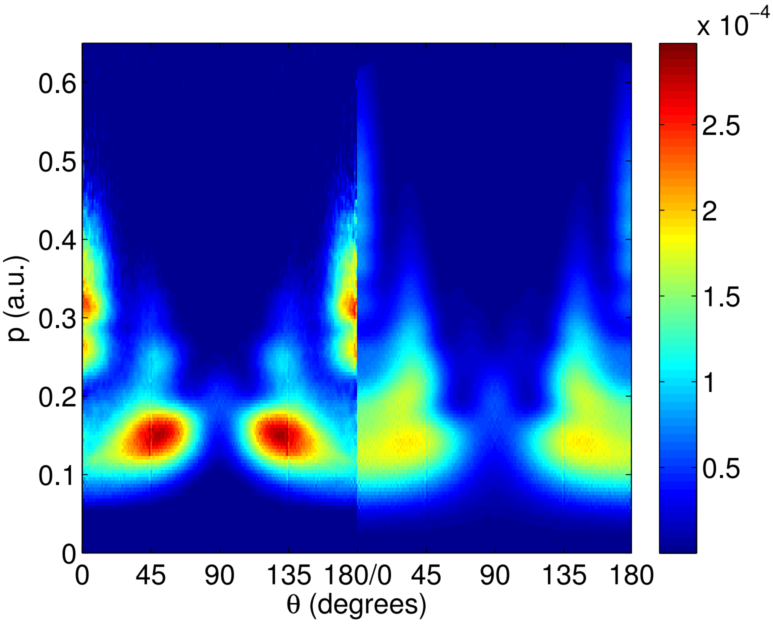

Figure 6.2: Comparison of experiment (left) and using the theory of Gribakin/Kuchiev (right) of the photoelectron momentum distribution for detachment of Ag^- at 2055 nm. The figure is in polar coordinates where θ is the angle to the laser polarization axis.

Another advantage of the tomographic method is the insensitivity to the polarization axis being parallel to the detector plane. When IAT is to be performed, one needs to make sure that the polarization and the detector are perfectly parallel to each other. If not, information about the electron distribution will be lost. In the case of IRT, however, having the polarization axis misaligned merely introduces an offset in the angle ϑ which can be easily adjusted for in post-processing.

By spreading the information of the electron swarm over a larger area on the detector, the tomographic method is also less sensitive to inhomogeneities in the detector. Consider a portion of the electron swarm occupying a ball with volume $V = 4\pi(\Delta p)^3/3$ in momentum space. If the time of flight for the electrons in the EIS is assumed to be Δt then, in case the polarization orientation is stationary (as in IAT), the electrons will be projected onto an area $\pi(\Delta t \Delta p)^2$ on the detector. Let p_r be the distance from the axis of rotation to the center of the volume V. Now if we instead rotate the polarization axis in sufficiently small steps, the volume V will sweep out a torus with major radius p_r. This torus projects onto an area on the detector surface that is $\pi(\Delta t \Delta p)^2 + 2p_r \Delta t \Delta p$. That is to say, we form a weighted average over different positions on the detector to reconstruct the electron distribution, with the effect being most pronounced for large values of p_r.

In figure 6.3 the 3D photoelectron momentum distribution for 1310 nm can be seen. The left panel shows the front view where the laser propagation axis and the laser polarization axis represent the directions of the (negative) horizontal and vertical axes of the image, respectively. The right panel shows a side view where the laser propagation axis is out of the paper and the laser polarization axis points in the vertical direction. It can be seen in the right panel that the torus produced by two-photon detachment comes out at an angle, with respect to the axis on which the caps of the two- and three-photon detachment lies, which deviates from the expected 90 degrees. This breaks the cylindrical symmetry of the electron swarm. Possible explanations of this tilt will be addressed in the following section. The fact that the caps are not aligned to the p_z axis could easily be explained by a slight offset in the rotation angle, but as the zero point in the polarization axis was aligned with an error of no more than ±1°, the 3D data is presented exactly as it was recreated. Figure 6.4 shows the same views for 2055 nm. Here no asymmetry is visible in the right panel. The left-right asymmetry in the left panels for both wavelengths can be ascribed to inhomogeneities in the detector response.

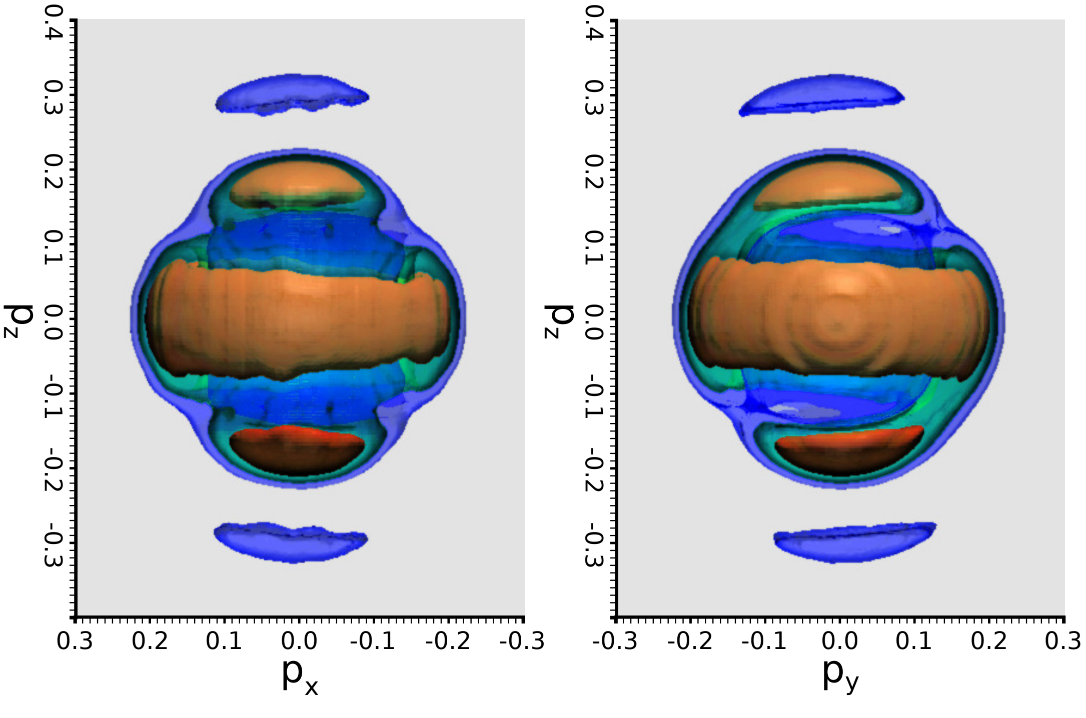

Figure 6.3: Reconstructed three-dimensional photoelectron momentum distribution for detachment of Ag^- at 1310 nm. The figure shows three isosurfaces at values 0.4 (red), 0.2 (green) and 0.1 (blue) of the maximum value. The laser is propagating in the x-direction and the laser polarization is along the z-axis.

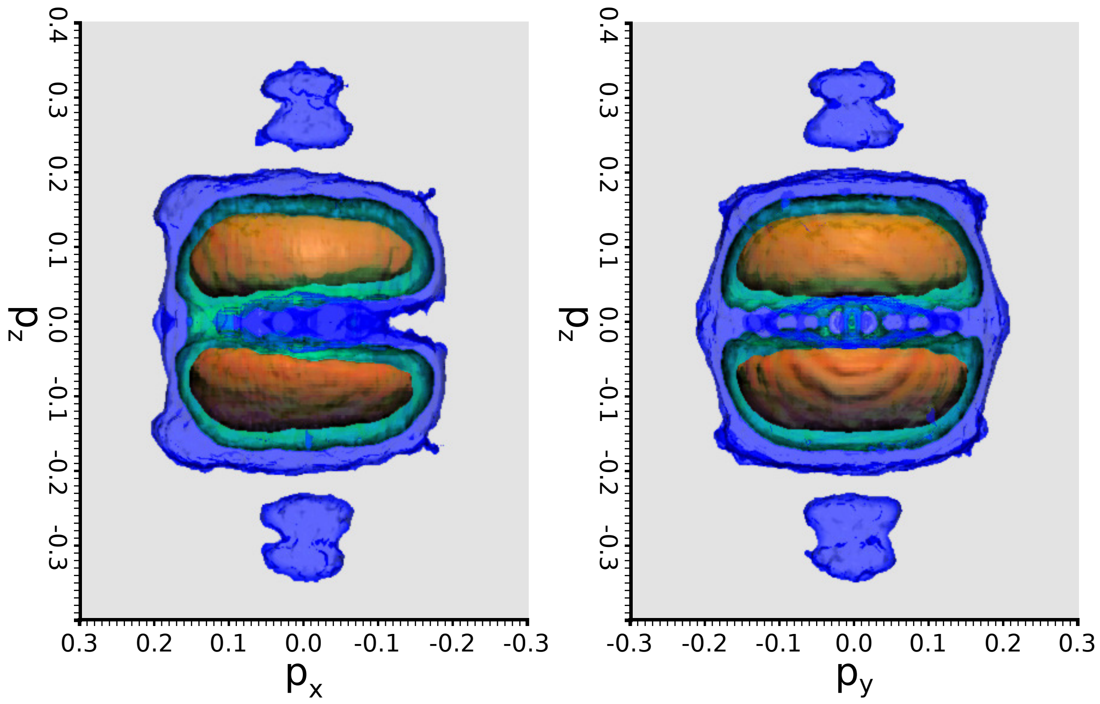

Figure 6.4: Reconstructed three-dimensional photoelectron momentum distribution for detachment of Ag^- at 2055 nm. The figure shows three isosurfaces at values 0.4 (red), 0.2 (green) and 0.1 (blue) of the maximum value. The laser is propagating in the x-direction and the laser polarization is along the z-axis.

6.5 Asymmetry in the polarization plane for photodetachment at 1310 nm

It is possible to rule out imperfect projection of photoelectrons, detector inhomogeneities, as well as the inversion method as causing factors of the asymmetry. This is due to the image acquisition taking place over a full rotation around the laser propagation axis, thereby averaging out any asymmetry. For a more thorough discussion of possible causes, see Appendix B. The most plausible explanation for the asymmetry is a residual elliptical polarization of the laser beam. Only through simulations with an elliptical polarization has the asymmetry been reproduced. Since mirror symmetry in the polarization plane is enforced by theories using the SFA, it is necessary to use an alternate theoretical approach to the generalized Gribakin/Kuchiev method presented in Section 2.3.1. One powerful method that is capable of explaining the asymmetry in terms of a residual elliptical polarization is the *quasistationary quasienergy state* approach (QQES) [59]. In the QQES approach the time-dependent Schrödinger equation (SE) is rewritten to take the form of a stationary SE. In addition to this the results have the property of being gauge invariant, a property famously absent in KFR theories[54, 95, 55].

In the QQES approach an initial bound state wave function with binding energy E_0

$$\Psi_0(\mathbf{r}, t) = e^{iE_0 t}\psi(\mathbf{r}), \tag{6.1}$$

dressed by an adiabatically switched on strong laser field takes the form

$$\Psi(\mathbf{r}, t) = e^{-i\epsilon t}\Phi_\epsilon(\mathbf{r}, t) \tag{6.2}$$

where $\Phi_\epsilon(\mathbf{r}, t) = \Phi_\epsilon(\mathbf{r}, t+2\pi/\omega)$ is the periodic QQES wave function and ϵ is the complex quasienergy of the state. The wave function Φ_ϵ fulfills the "quasistationary" SE

$$\mathcal{H}\Phi_\epsilon(\mathbf{r}, t) = \epsilon\Phi_\epsilon(\mathbf{r}, t) \tag{6.3}$$

with the Hamiltonian

$$\mathcal{H} = U(\mathbf{r}) + V_\mathrm{F}(t) - \nabla^2 - i\frac{\partial}{\partial t} \tag{6.4}$$

where $U(\mathbf{r})$ is the atomic potential and $V_\mathrm{F}(t)$ is the dipole interaction of the electron with the laser field

$$V_\mathrm{F}(\mathbf{r}, t) = \frac{1}{c}\mathbf{p}\cdot\mathbf{A}(t) + \frac{1}{2c^2}|\mathbf{A}(t)|^2 \tag{6.5}$$

with the magnetic vector potential $\mathbf{A}(t)$ defined such that the electric field is given by $\mathbf{F}(t) = -\frac{1}{c}\frac{\partial}{\partial t}\mathbf{A}(t)$. Note that while Eq. (6.5) is given in the velocity gauge, the final results of the QQES method are gauge invariant. The total detachment rate Γ of the negative ion can be extracted immediately from the quasienergy as

$$\Gamma = -2\,\mathrm{Im}(\epsilon). \tag{6.6}$$

In the case when the atomic potential is taken to be a zero-range potential (2.24), the QQES wave function is given by

$$\Phi_\epsilon(\mathbf{r}, t) = -4\pi\int_0^\infty e^{i\epsilon t'}G^{(+)}(\mathbf{r}, t, 0, t-t')f_\epsilon(t-t')dt', \tag{6.7}$$

where $G^{(+)}$ is the retarded Green's function of a free electron subject to the interaction Hamiltonian (6.5). The quasienergy ϵ and the function $f_\epsilon(t)$ is the eigenvalue/eigenfunction pair to the integral equation

$$(\sqrt{E}-1)f_\epsilon(t) = \frac{1}{\sqrt{4\pi i}}\int_0^\infty\left(f_\epsilon(t-t')e^{iu_p t'+iS(t',t-t')} - f_\epsilon(t)\right)\frac{e^{-iEt'}}{(t')^{3/2}}dt \tag{6.8}$$

where $E = u_p - \epsilon$ is the effective (complex) binding energy,

$$\begin{aligned} S(t,t') = &-\frac{u_p}{\omega}\left(\omega(t-t') - \frac{4\sin^2(\omega(t-t')/2)}{\omega(t-t')}\right) \\ &+ \frac{lu_p}{\omega}\cos(\omega(t+t'))\left(\sin(\omega(t-t')) - \frac{4\sin^2(\omega(t-t')/2)}{\omega(t-t')}\right) \end{aligned} \tag{6.9}$$

is the coordinate independent part of the classical action,

$$u_p = \frac{U_p}{|E_0|} \tag{6.10}$$

is the ratio between the ponderomotive and binding energies, and

$$l = \frac{1-\varepsilon^2}{1+\varepsilon^2} \tag{6.11}$$

is the degree of linear polarization in terms of the ellipticity ε.

The n-photon differential detachment rate is given by

$$\frac{d\Gamma^{(n)}}{d\Omega} = 2|\sqrt{k_n}\mathcal{A}_n|^2, \tag{6.12}$$

where $k_n^2 = n\omega - E$ is the complex equivalent of the photoelectron energy, and

$$\mathcal{A}_n = i^n \sum_{j=-\infty}^{\infty} f_j \sum_{m=-\infty}^{\infty} (-1)^m J_{m-j}\left(\frac{lu_p}{2\omega}\right) J_{n-2m}\left(\frac{2F\sqrt{1+\varepsilon^2}k_n}{\omega^2}|\hat{\varepsilon}\cdot\hat{\mathbf{n}}|\right)\left(\frac{\hat{\varepsilon}\cdot\hat{\mathbf{n}}}{|\hat{\varepsilon}\cdot\hat{\mathbf{n}}|}\right)^{n-2m}, \tag{6.13}$$

where the electric field strength F is defined in Eq. (2.12), f_j are the coefficients for the Fourier expansion of $f_\epsilon(t)$

$$f_\epsilon(t) = \sum_{j=-\infty}^{\infty} f_j e^{-2ij\omega t}, \tag{6.14}$$

J_n are Bessel functions of the first kind,

$$\hat{\varepsilon} = \frac{\hat{\mathbf{z}} - i\varepsilon\hat{\mathbf{y}}}{\sqrt{1+\varepsilon^2}} \tag{6.15}$$

is the unit polarization vector, and $\hat{\mathbf{n}}$ is the unit vector in the direction of the asymptotic photoelectron momentum vector. For the full derivation of the differential detachment rate, see Refs. [96, 59].

The code for calculating the quasienergy and angular distribution was obtained from the authors of Ref. [59]. Using the simulation procedure described in Sec. 3.1. the electron distribution in the polarization plane was simulated taking the spatiotemporal population of the laser focus into account. Due to the significant computational demands of the QQES method, the simulation was limited to the two and three photon processes in which the asymmetry is apparent.

To be able to estimate the ellipticity of the laser polarization in the experiment, the angular distance between the polar (close to the p_z-axis) and equatorial (close to the (p_x,p_y)-plane) maxima was used as a metric. Figure 6.5 shows the relative distance between the maxima as a function of the ellipticity ε. Blue curves represent the simulated distributions for $F = \{1.5, 3.0, 4.5, 6.0\} \times 10^{-2}$ a.u. and are shown to intersect with the experimentally obtained angle (black) at an ellipticity of $\varepsilon = 0.21 \pm 0.01$. The simulation for this estimated ellipticity is shown in Fig. 6.7 and the experimental distribution is shown in Fig. 6.6. As was the case for the Gribakin/Kuchiev simulation in Fig. 6.1, the three photon yield is overestimated compared to yield of the two photon process, but to a lesser degree. To put emphasis on the lack of mirror symmetry Figs. 6.8 and 6.9 show contour plots of the photoelectron count in the polarization plane for the experimental and simulated distributions, respectively. To de-emphasize the ratio between the yields of the two- and three-photon processes, the yields have been individually normalized. The angular distributions for the experimental and simulated images are in good agreement for both the two- and three-photon processes and the asymmetry of the experimental data is reproduced in the simulation. The inset in Fig. 6.9 shows the ellipse representing the rotational direction and magnitude of the laser field for $\varepsilon = 0.21$.

6.6 Conclusion

We have developed a tomographic imaging method to recreate the full three-dimensional distribution of photoelectrons produced in a strong-field photodetachment process. The method is general and can be applied to any polarization. This stands in contrast to traditional imaging inversion methods, such as Abel inversion, which require a prior knowledge of the symmetries of the electron distribution. This limits experiments to linear or circular polarization. The developed method is also useful in a situation where linear polarization is used, since it allows us to automatically compensate for inhomogeneities in the detector by spreading the information on a larger detector surface. In addition to this it facilitates a method to detect polarization defects.

Measurements were made for photodetachment of Ag^- at laser wavelengths of 1310 and 2055 nm, and were found to agree well with simulations of theoretical models. The data in the 1310 nm case revealed an unexpected asymmetry in the plane in which the laser polarization axis is rotated. A range of possible causes for this observation were

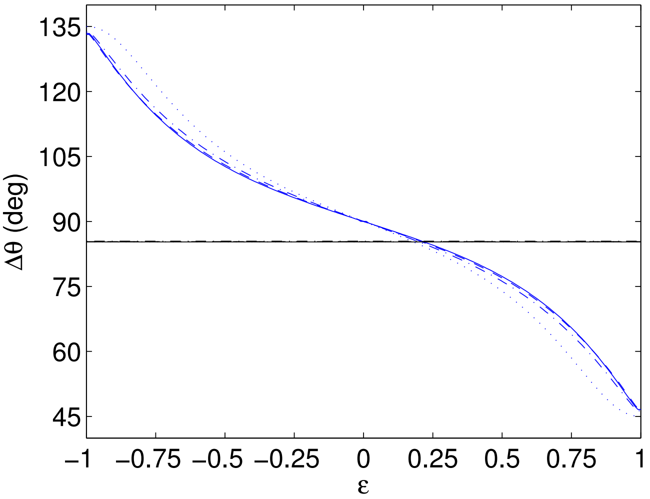

Figure 6.5: Angular distance between the polar and equatorial maxima for laser field strengths 0.1 (solid), 0.2 (dashed), 0.3 (dash-dotted) and 0.4 (dotted) for two-photon detachment of Ag^- at 1310 nm. Blue curves represent simulated values as a function of the ellipticity ε and the black curves represent the experimentally measured values.

examined in detail but could be ruled out. Using a QQES model, a residual elliptical polarization with $\epsilon = 0.21$ can however consistently explain the asymmetry. An obvious improvement to the experiment would be to add a polarizing filter that rotates with the half-wave plate to control the polarization. A thorough investigation of the ellipticity dependence on the photoelectron distribution would be of considerable interest.

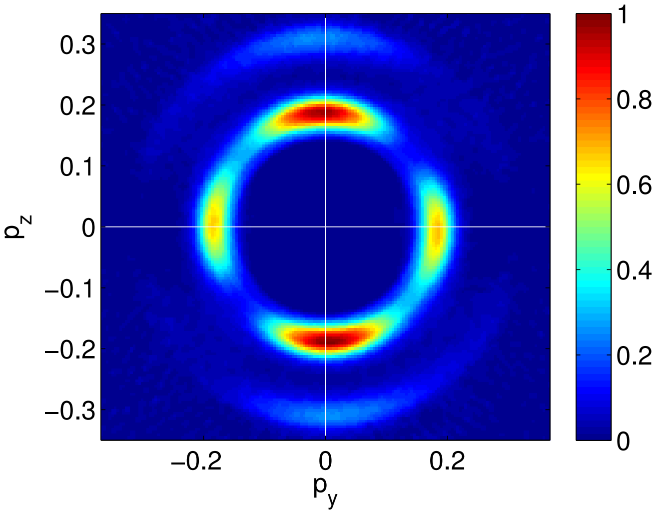

Figure 6.6: Experimental photoelectron momentum distribution in the central polarization plane obtained at two and three photon detachment of Ag^- at a wavelength of 1310nm.

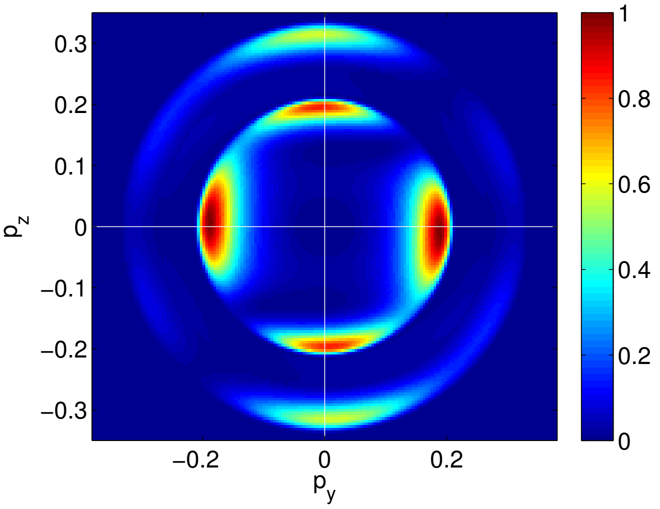

Figure 6.7: Simulated photoelectron momentum distribution in the central polarization plane obtained through simulation of two and three photon detachment of Ag^- at a wavelength of 1310nm, using the QQES method for an ellipticity of $\varepsilon = 0.21$.

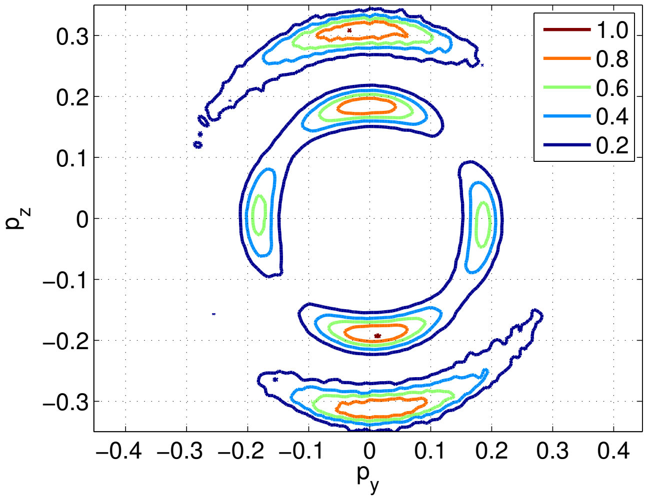

Figure 6.8: Contour plot of the experimental photoelectron momentum distribution in the central polarization plane obtained at two and three photon detachment of Ag^- at a wavelength of 1310nm. The two and three photon processes have been individually normalized.

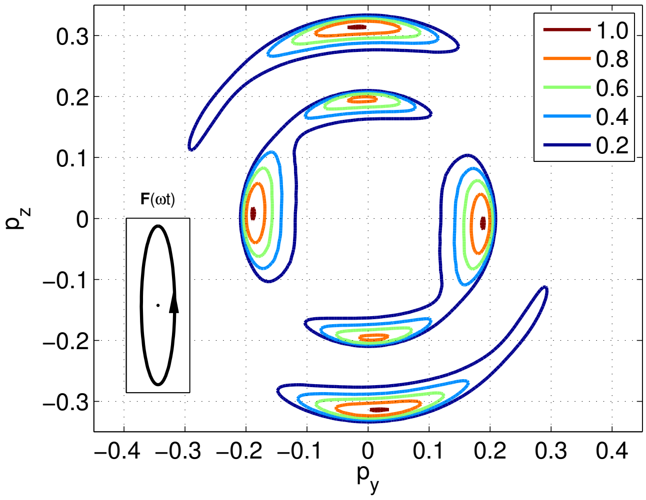

Figure 6.9: Contour plot of the simulated photoelectron momentum distribution in the central polarization plane obtained through QQES simulation of two and three photon detachment of Ag^- at a wavelength of 1310nm. The two and three photon processes have been individually normalized. The inset ellipse represents the rotational direction and magnitude of an elliptically polarized laser field with ellipticity $\varepsilon = 0.21$.

Chapter 7

Strong-Field Photodetachment of Homonuclear Diatomic Negative Ions

7.1 Introduction

The subject of study in this chapter is photodetachment of homonuclear diatomic negative ions in a strong laser field. Experimental data for C_2^-, Si_2^- and Ag_2^- are compared to theoretical models. In a recent paper [51], two models based on the strong field approximation were developed attempting to describe the process. While the models were developed for ionization of neutral molecules, they can be modified to simulate detachment of negative ions.

In the case of single-atom negative ions, for a given momentum of the detached electron, the detachment process mainly occurs at two distinct times during a laser cycle, giving rise to two possible trajectories of the ejected electron which will necessarily interfere with each other. The same holds true for diatomic molecules, but the fact that the electron has the possibility of being ejected from either of the two atomic cores makes the situation more complicated. The consideration of two cores also means that the difference in electric potential between the cores as induced by the laser field can be taken into account. In the *undressed* version of the model, such dressing by the laser field is neglected and any interference between the two trajectories is merely a result of the relative spatial orientation of the cores. In the *dressed* version, on the other hand, the laser-field induced potential difference between the cores is taken to generate a phase difference between the two trajectories of $e^{i\mathbf{R}_0\cdot\mathbf{k}_\mathrm{t}}$, where $\mathbf{R}_0$ is the relative position vector of the two cores and $\mathbf{k}_\mathrm{t}$ is the ponderomotive momentum of a free electron oscillating in the laser field.

A recent paper by Hultgren *et al.*[32] treated strong-field photodetachment of F_2^-. The experimental data in this case showed large discrepancies the with the theoretical models. This was explained by the fact that the dissociation energy at 1.21 eV is only a fraction of the vertical detachment energy at 3.965 eV, resulting in a non-determinate contribution from photodetachment of F^-. In the three molecular species that are the subject of study here [$D_0(C_2^-) = 8.12$ eV, $EA(C_2) = 3.27$ eV; $D_0(Si_2^-) = 2.93$ eV, $EA(Si_2) = 2.20$ eV; $D_0(Ag_2^-) = 1.37$ eV, $EA(Ag_2) = 1.06$ eV] , this should play a much smaller role since the dissociation energy is larger than the electron affinity.

7.2 Methods

The methods and experimental setup used in this chapter are described in detail in Chaps. 3 and 4.

The experimental data for C_2^- was obtained using the traditional photoelectron velocity map imaging technique described in Sec. 4.3. The data was accumulated by taking 30 images at an exposure time of 20 seconds. For every image a corresponding image was recorded with the laser blocked, allowing for subtraction of background noise. The total recording time was 20 minutes including the background measurements. The ion beam had a current of 230 nA and was crossed by a laser beam which was focused by a 15 cm lens to a focus size of 20 and 30 μm FWHM for the 1310 nm and 2055 nm beam, respectively. The 130 fs pulses had a pulse energy of 195 μJ and 98 μJ, respectively, reaching peak intensities of the order of 3.1×10^{14} and 6.9×10^{13} W/cm^2.

Traditional VMI was also used for Si_2^-, where the ion current reached 85 nA. Data was accumulated for 30 images for a duration of 30 seconds each, for a total of 30 minutes recording time. 1340 and 1985 nm laser pulses of 130 fs duration were focused using a 20 cm lens to a beam waist of 27 and 40 μm. The pulse energies were here 203 and 102 μJ yielding a peak intensity of the order of 1.8×10^{14} and 4.0×10^{13} W/cm^2, respectively.

In the case of Ag_2^-, the tomographic method described in Chap. 6 was used, collecting data at 120 different angles for 6×10 seconds each. This led to a total recording time of 4 hours. The ion current was 9 nA. The 130 fs pulses used were of wavelengths 1310 and 2055 nm and had a pulse energy of 60 and 30 μJ, yielding a peak intensity of 5.3×10^{13} and 9.6×10^{12} W/cm^2, respectively.

For carbon and silicon, the above parameters were used to simulate the process using the molecular strong-field approximation described in Sec. 2.3.2. The simulation procedure takes into account the temporal and spatial intensity distribution of the laser focus, saturation effects as well as the random orientation of the internuclear axis.

In the case of silver, the theoretical photoelectron distribution was obtained by calculation the strength of vibrational transitions by weighing them by their Franck-Condon factors (square of the overlap integral (2.60)) and the Boltzmann factors of a thermal distribution of the negative ions

$$e^{-E_\nu/k_\mathrm{B}T}, \tag{7.1}$$

where E_ν is the energy of the ν:th vibrational state, k_B is the Boltzmann constant and T the temperature of the ions.

7.3 Results

In this section, experimental data obtained for photodetachment of C_2^- , Si_2^- and Ag_2^- is presented and compared to simulations.

C_2^-

In the left panels of Figs. 7.1 and 7.3, the Abel inverted photoelectron images produced by photodetachment of C_2^- at a laser wavelength of 1310 nm and 2055 nm are shown, respectively. The center and right panels show simulations for the dressed and undressed version of the theory presented in section 2.3.2. The simulations were made for the transition $\mathrm{C}_2^-(X^2\Sigma_\mathrm{g}^+) \rightarrow \mathrm{C}_2(X^1\Sigma_\mathrm{g}^+)$ by detachment of a σ_g electron. Figures 7.2 and 7.4 represent a cut along the vertical axis of the images to show the momentum distribution of photoelectrons along the laser polarization axis for 1310 and 2055 nm, respectively.

It can be seen that for both wavelengths, theory and experiment are in good agreement with each other. In particular, the positions of the maxima agree well. In the 1310 nm case, there is a shoulder in the simulations at approximately $p_\| = 0.6$ a.u. which is not apparent in the experimental data (see Fig. 7.2). The shoulder is slightly more pronounced in the undressed case. The simulated distributions are wider in the $p_\perp$ direction than for the experimental case (see Fig. 7.1). Additionally, a high energy jet, extending to around 1.5 a.u. along the laser polarization axis, is visible in the experiment which has no counterpart in the simulated distributions.

For the 2055 nm case, the agreement along the polarization axis is even better (see Fig. 7.4). Again the simulated distributions are wider than experiment (see Fig. 7.3). The difference between the simulations of the dressed and undressed case is small for both wavelengths.

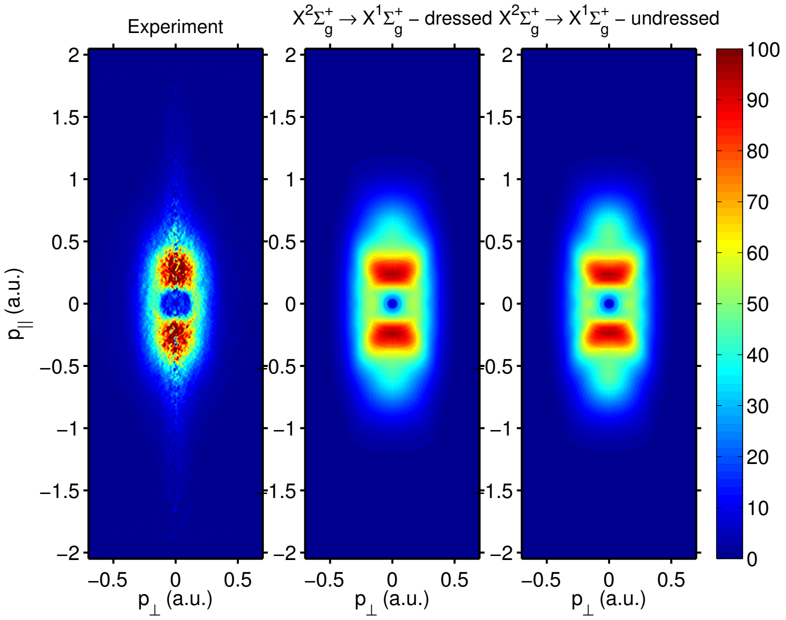

Figure 7.1: Abel inverted experimental photoelectron momentum distribution for photodetachment of C_2^- (left) measured at a laser wavelength of 1310 nm compared to simulations of the dressed (center) and undressed (right) versions of the molecular SFA. The laser polarization is oriented along $p_{\|}$.

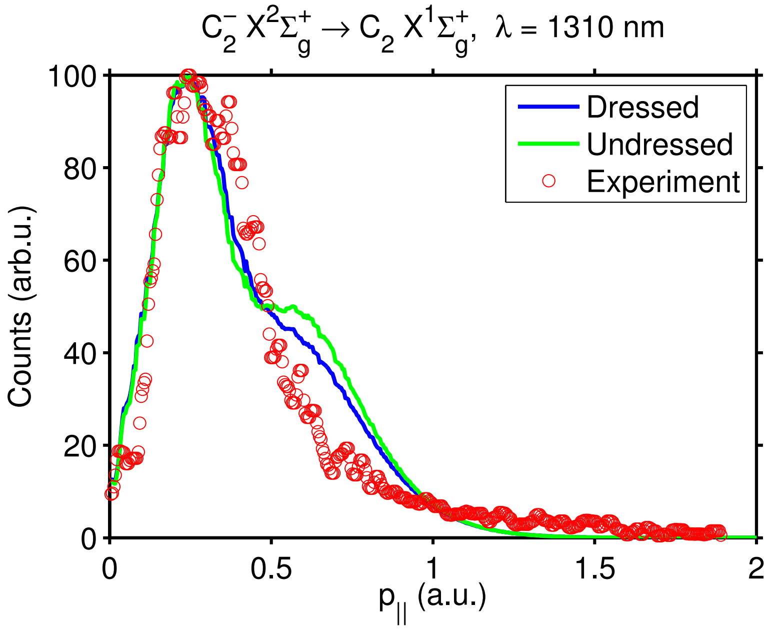

Figure 7.2: Photoelectron momentum distribution along the laser polarization axis for photodetachment of C_2^- at 1310 nm.

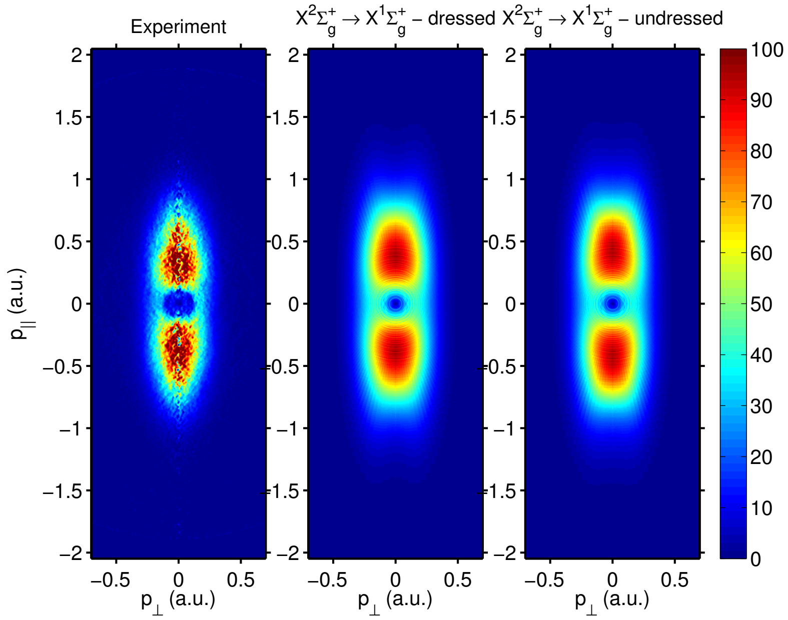

Figure 7.3: Abel inverted experimental photoelectron momentum distribution for photodetachment of C_2^- (left) measured at a laser wavelength of 2055 nm compared to simulations of the dressed (center) and undressed (right) versions of the molecular SFA. The laser polarization is oriented along $p_{\|}$.

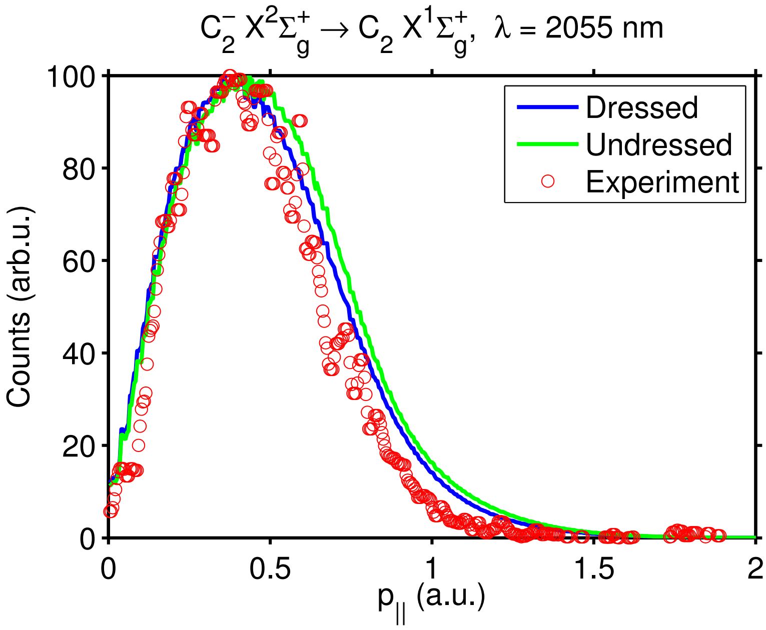

Figure 7.4: Photoelectron momentum distribution along the laser polarization axis for photodetachment of C_2^- at 2055 nm.

Si_2^-

The corresponding images for Si_2^- are shown in Figs. 7.5 and 7.6 for a laser wavelength of 1340 nm and in Figs. 7.7 and 7.8 for a wavelength of 1985 nm. The simulations were made for the transition $\mathrm{Si}_2^-(X^2\Sigma_\mathrm{g}^+) \rightarrow \mathrm{Si}_2(D^3\Pi_\mathrm{u})$ by detachment of a π_u electron. For both wavelengths the simulations of the dressed and undressed cases are again similar to each other although the dressed case has a narrower distribution in the $p_\perp$ direction, especially in the 1985 nm case.

The agreement between theory and experiment in the 1340 nm case is not as good as for C_2^-. The simulations predict pronounced EPD peaks which are not clearly visible in the experimental data. Plateaus are however present at the corresponding momenta as can be seen in Fig. 7.6. Further, the intensity of higher-energy processes are overestimated in the simulations. Such plateaus are present in the all the experimental distributions for C_2^- and Si_2^-, but they are not predicted by theory except for in the Si_2^- 1340 nm case.

The experimental data in the 1985 nm case is in good agreement with the dressed simulation and less so with the undressed one. The simulations, the undressed in particular, show a shoulder at around $p_\parallel = 0.6$ a.u. (see Fig. 7.8), a feature not present in the experiment. The experimental distribution shows a larger signal at lower momenta than the simulations. There is a weak high-energy jet observed in the experimental data along the laser polarization direction for both wavelengths. These jets are not reproduced in the simulations. The undressed simulation becomes two-pronged around a momentum of $p_\parallel = 0.6$ a.u. (Fig. 7.7). There is no indication of this in the experimental data. The same split can be seen also at 1340 nm, but to a lesser extent.

Ag_2^-

The experimental data for Ag_2^- was collected using the tomographic method presented in chapter 6. The Abel inversion equivalent photoelectron images obtained for wavelengths 1310 and 2055 nm are presented in figure 7.9. Due to the multitude of vibrational transitions, the linewidth of the transition $\mathrm{Ag}_2^-(X^2\Sigma_\mathrm{u}^+) \rightarrow \mathrm{Ag}_2(X^1\Sigma_\mathrm{g}^+)$ is 146, 253 and 287 meV FWHM for initial temperatures of 300, 1000 and 3000 K, respectively. This can be seen in Fig. 7.10 which shows the product of the Boltzmann factors of the initial states and Franck-Condon factors for all possible vibrational transitions as a function of the energy of the transition. This distribution is then used to calculate the photoelectron distribution shown in Figs. 7.11 and 7.12 for a wavelength of 1310 and 2055 nm, respectively, by subtracting the transition energy from the energy of the

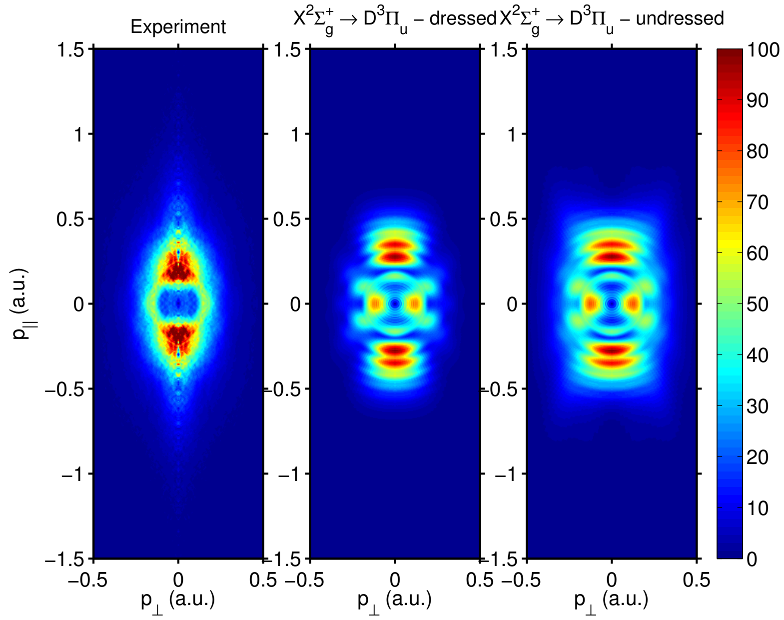

Figure 7.5: Abel inverted experimental photoelectron momentum distribution for photodetachment of Si_2^- (left) measured at a laser wavelength of 1340 nm compared to simulations of the dressed (center) and undressed (right) versions of the molecular SFA. The laser polarization is oriented along $p_{\|}$.

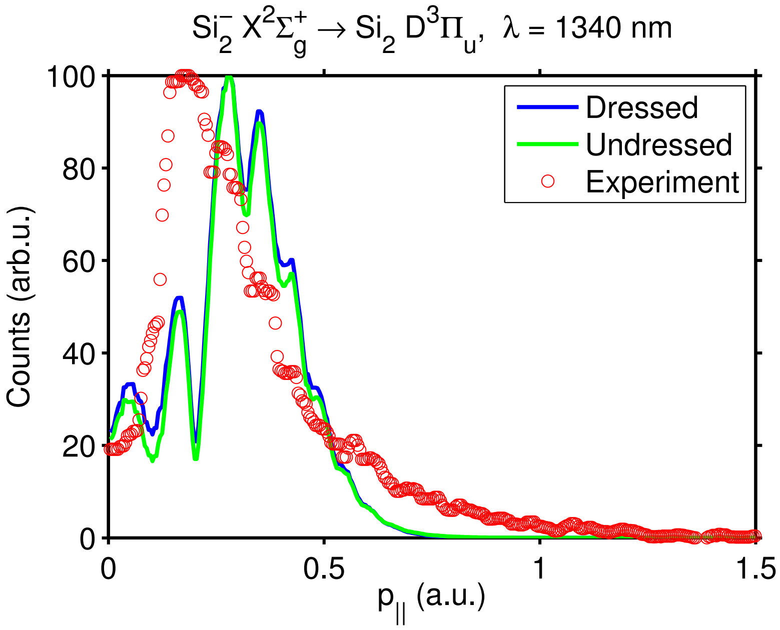

Figure 7.6: Photoelectron momentum distribution along the laser polarization axis for photodetachment of Si_2^- at 1340 nm.

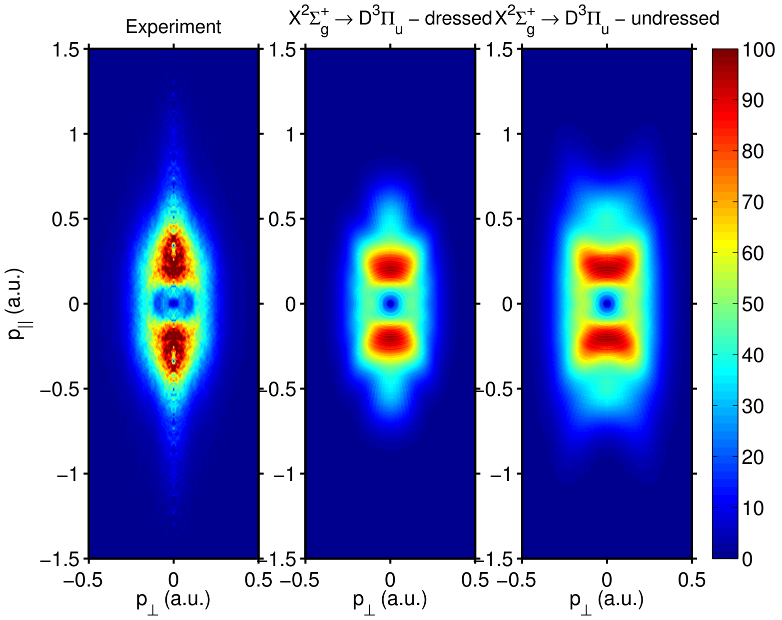

Figure 7.7: Abel inverted experimental photoelectron momentum distribution for photodetachment of Si_2^- (left) measured at a laser wavelength of 1985 nm compared to simulations of the dressed (center) and undressed (right) versions of the molecular SFA. The laser polarization is oriented along $p_{\|}$.

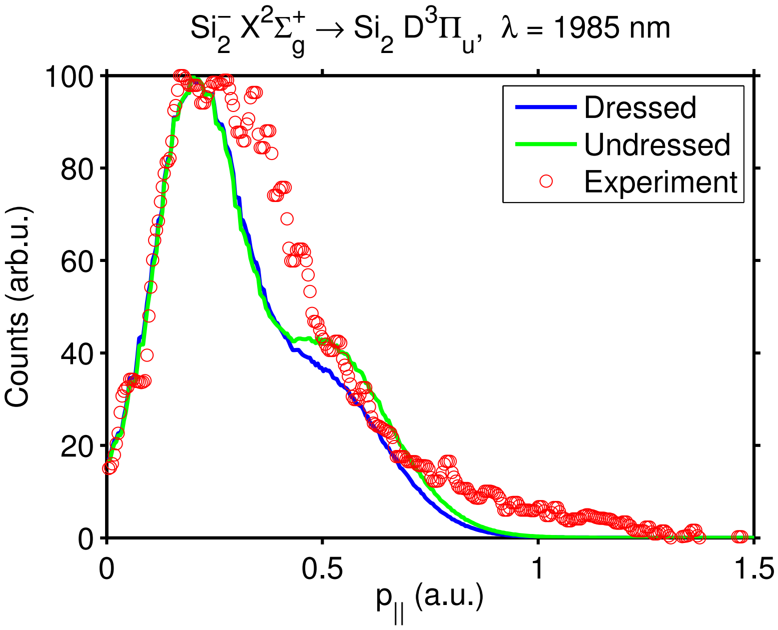

Figure 7.8: Photoelectron momentum distribution along the laser polarization axis for photodetachment of Si_2^- at 1985 nm.

absorbed photons. The photoelectron distributions are binned in order to emulate the limited resolution of the imaging detector. In addition to this the signal is multiplied with the square root of the photoelectron energy to account for the density of states of the detached electron. The experimental curves are obtained by integrating the recreated 3D electron distribution over a solid angle of 4π.

It can be seen in the left panel of Fig. 7.9 that for a wavelength of 1310 nm, the recorded photoelectron distribution is nearly isotropic. The central peak at low momentum is a result of a one-photon process. Fig. 7.11 shows the experimental and calculated energy distributions of photoelectrons. The calculated distributions are very narrow with a FWHM of 13, 23 and 25 meV for 300, 1000 and 3000 K, respectively. The experimental distribution is much wider with a FWHM of 135 meV.

In the 2055 nm case, there is again a sharp peak at low electron momentum in the center of the experimental image (Fig. 7.9, right panel). The center peak is a result of a two-photon process. There is also a clear sign of a 3-photon process with p character that has its peak value on the laser polarization axis at $p_{\|} = \pm 0.173$ atomic units. The integrated experimental distribution in Fig. 7.12 shows that the center peak has a FWHM of 65 meV on the energy scale and that the 3-photon process has its maximum at 409 meV. For the three calculated distributions, the two- and three-photon processes peak at energies of 130, 168, 226 meV and 731, 749, 815 meV, respectively.

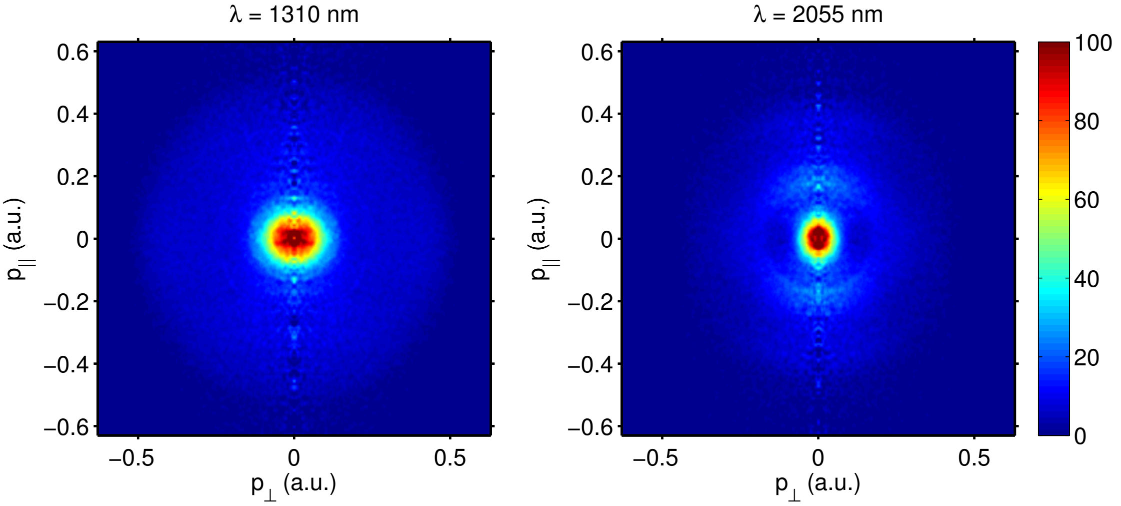

Figure 7.9: Abel inversion equivalent photoelectron momentum distribution produced in photodetachment of Ag_2^- for laser wavelengths of 1310 (left) and 2055 nm (right)

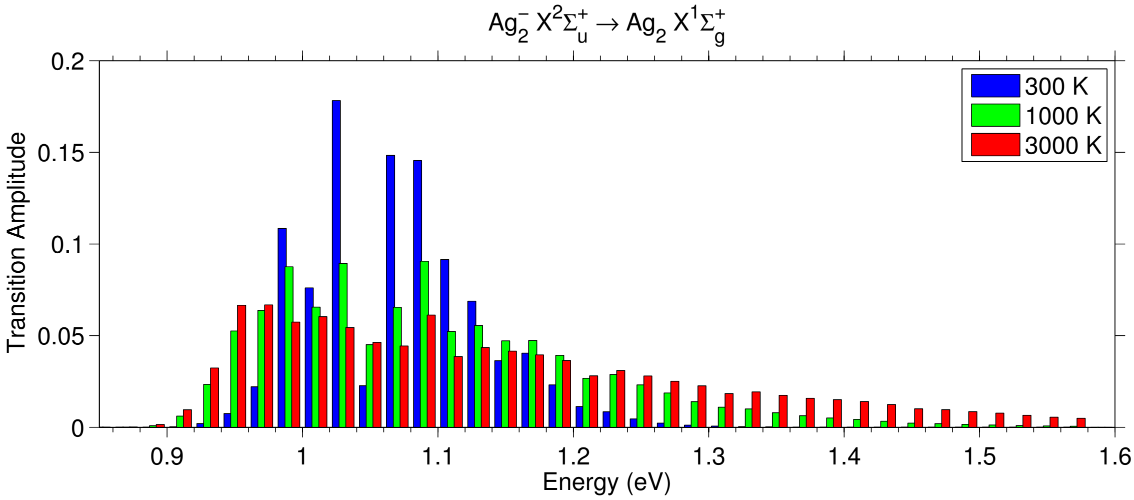

Figure 7.10: Calculated transition probability as a function of the detachment energy for Ag_2^- at a temperatures of 300, 1000 and 3000 K. The bin size is 0.02 eV.

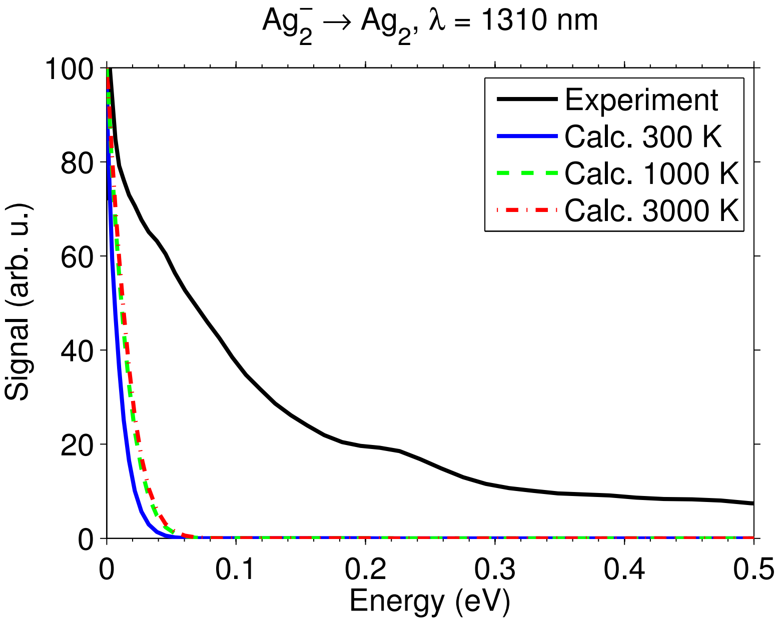

Figure 7.11: Photoelectron energy distribution integrated over the full solid angle for photodetachment of Ag_2^- at 1310 nm.

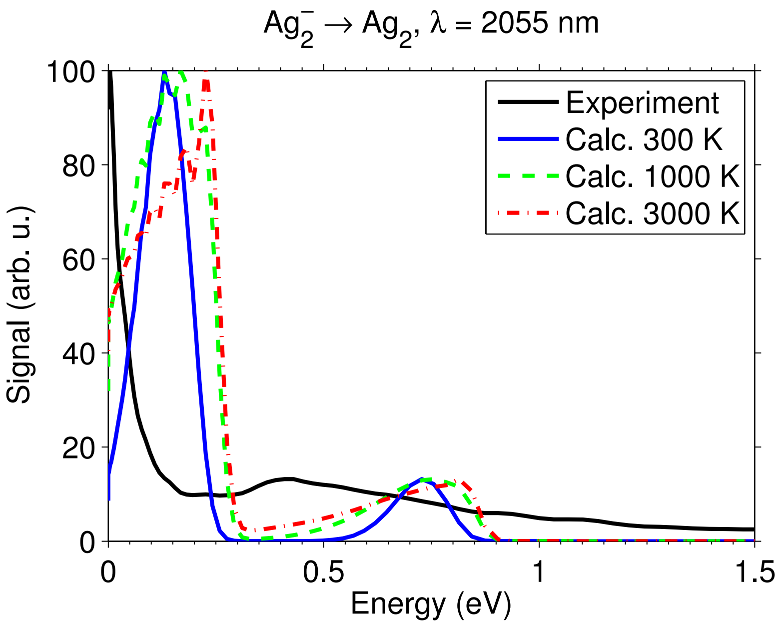

Figure 7.12: Photoelectron energy distribution integrated over the full solid angle for photodetachment of Ag_2^- at 2055 nm.

7.4 Discussion

The agreement between the experimental and simulated strong-field electron distributions is good in the case of dicarbon and disilicon, with the exception of the 1340 nm case for disilicon, where the difference is larger. In the following a discussion of the energy levels involved is made, followed by an overall discussion of all three molecular species.

Table 7.1 gives the characteristic data for the electronic states of C_2^- and C_2 and in Fig. 7.13 potential curves of a few select states are shown. In the simulations we only considered the $X(\nu = 0) \rightarrow X(\nu' = 0)$ transition, by detachment of an electron in the σ_g orbital. The assumption that the negative ion is in its electronic ground state is well justified as the first excited electronic state is virtually unpopulated because of its high excitation energy of 0.49 eV. The temperature of the molecular ions is largely unknown, but even assuming a temperature of 1000 K yields 92% of the population in the electronic and vibrational ground state. Due to the similar internuclear distance of the electronic ground-states of the negative ion and the neutral, the $X \rightarrow X$ transition dominates over the $X \rightarrow a$ transition (cf. [97], Fig. 1). The electron affinity of C_2 is 3.269(6) eV which means that a minimum of 4 and 6 photons are necessary to detach at wavelengths of 1310 and 2055 nm, respectively.

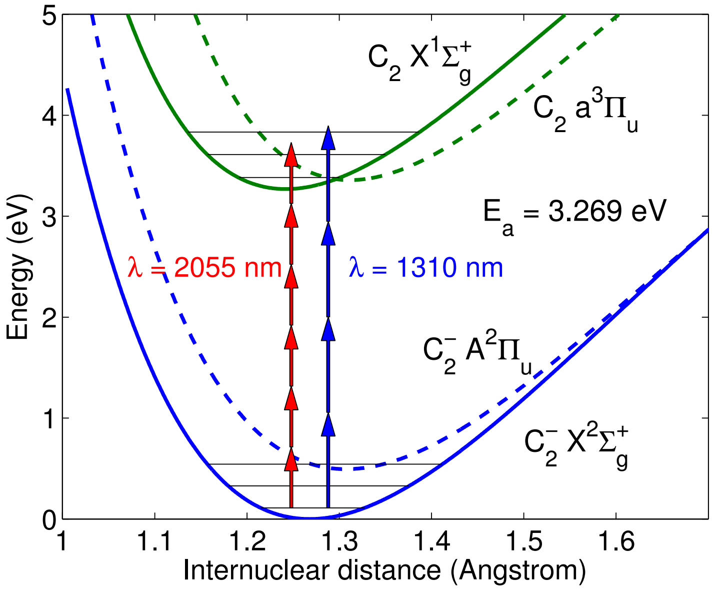

Figure 7.13: Qualitative depiction of potential curves for C_2^- mentioned in the text. The arrows represent the minimum amount of photons necessary for photodetachment.

The data for the electronic states of Si_2^- and Si_2 are listed in Table 7.2 and in Fig. 7.14 potential curves for select states are shown. The simulation was limited to the transition $X(\nu = 0) \rightarrow D(\nu' = 0)$ by detachment of a π_u electron. Limiting ourselves to a single electronic transition is not as clearly justifiable as in the dicarbon case above, the ground state and the first excited state being energetically very close to each other ($T_e(\mathrm{Si}_2^- \mathrm{A}^2\Pi_\mathrm{u}) = 0.025(10)\mathrm{eV}$). There is presumably a significant population in the first excited electronic state, but the exact value is difficult to ascertain due to the unknown temperature of the ions together with the large uncertainty in the energy of the excited state. Detachment of the A state mainly occurs by means of removal of a π_u electron to induce the transition $A \rightarrow X$. This would require an energy of 2.177 eV as opposed to the 2.2430 eV necessary for the $X \rightarrow D$ transition. The small difference in energy and internuclear distance means that the simulated distribution of these two transitions do not differ significantly and we therefore limit our attention to the $X \rightarrow D$ transition. As for transitions into even higher-lying excited states of the neutral there is no sign of such transitions in the experimental data. To overcome the detachment energy a minimum of 3 and 4 photons are necessary in the 1340 and 1985 nm cases.

The case of diatomic silver seems simpler at first glance due to the lack of excited electronic states of the negative ion and the presence of only a single loosely bound state of the neutral molecule (see Table 7.3 and Fig. 7.15). Due to the abundance of

	State	T_e (eV)	ω_e (cm^{-1})	$\omega_\mathrm{e}x_\mathrm{e}$ (cm^{-1})	r_e (Å)
C_2^-	$X^2\Sigma_\mathrm{g}^+(\sigma_\mathrm{g}^1\pi_\mathrm{u}^4)$	0	1781.189(18)	11.6717(48)	1.2683
	$A^2\Pi_\mathrm{u}(\sigma_\mathrm{g}^2\pi_\mathrm{u}^3)$	0.494169(63)	1666.4(10)	10.80(26)	1.3077
	$B^2\Sigma_\mathrm{u}^+(\sigma_\mathrm{g}^3\pi_\mathrm{u}^2)$	2.2801065(44)	1969.542(84)	15.100(57)	1.2234
C_2	$X^1\Sigma_\mathrm{g}^+(\sigma_\mathrm{g}^0\pi_\mathrm{u}^4)$	0	1854.5881(83)	13.2730(38)	1.2425
	$a^3\Pi_\mathrm{u}(\sigma_\mathrm{g}^1\pi_\mathrm{u}^3)$	0.08905806(3)	1641.3423(24)	11.66474(24)	1.3119

Table 7.1: The first few electronic states for C_2^- and C_2. EA (C_2) = 3.269(6) eV. T_e is the electronic excitation energy relative to the ground state, ω_e and $\omega_e x_e$ are the linear and quadratic expansion coefficients for the vibrational energy in an anharmonic oscillator, respectively, and r_e is the internuclear distance. [97][98]

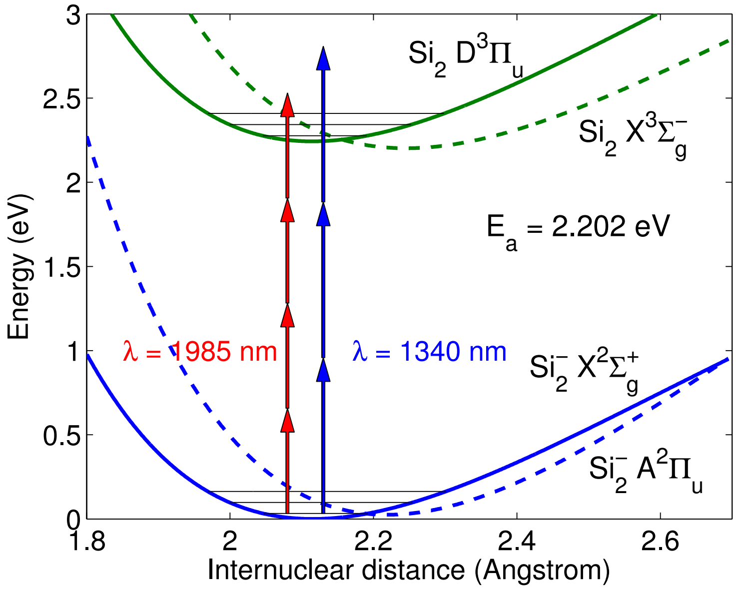

Figure 7.14: Qualitative depiction of potential curves for Si_2^- mentioned in the text. The arrows represent the minimum amount of photons necessary for photodetachment.

vibrational transitions, however, performing a strong-field simulation taking all possible transitions into account is computationally very demanding and not feasible on a normal PC. The simulation of Ag_2^- is therefore limited to a simple calculation of transition probabilities based on their Franck-Condon factors. The calculations were done for 300, 1000 and 3000 K. The exact temperature is unknown, but in [102] where a flowing afterglow ion source was used, the estimated temperature of the molecules is 350 K. In this case the pressure of the source was 0.5 mbar so that the molecules were subject

	State	T_e (eV)	ω_e (cm^{-1})	$\omega_\mathrm{e}x_\mathrm{e}$ (cm^{-1})	r_e (Å)
Si_2^-	$X^2\Sigma_\mathrm{g}^+(\sigma_\mathrm{g}^1\pi_\mathrm{u}^4)$	0	528(10)	...	2.116(5)
	$A^2\Pi_\mathrm{u}(\sigma_\mathrm{g}^2\pi_\mathrm{u}^3)$	0.025(10)	533(5)	...	2.207(5)
Si_2	$X^3\Sigma_\mathrm{g}^-(\sigma_\mathrm{g}^2\pi_\mathrm{u}^2)$	0	509(10)	...	2.246
	$D^3\Pi_\mathrm{u}(\sigma_\mathrm{g}^1\pi_\mathrm{u}^3)$	0.041(10)	536(5)	...	2.115
	$a^1\Delta_\mathrm{g}(\sigma_\mathrm{g}^2\pi_\mathrm{u}^2)$	0.435(2)	486(10)	...	2.290(10)
	$b^1\Pi_\mathrm{u}(\sigma_\mathrm{g}^1\pi_\mathrm{u}^3)$	0.544(10)	540(10)	...	2.160(5)

Table 7.2: The first few electronic states for Si_2^- and Si_2. EA (Si_2) = 2.202(10) eV. T_e is the electronic excitation energy relative to the ground state, ω_e and $\omega_e x_e$ are the linear and quadratic expansion coefficients for the vibrational energy in an anharmonic oscillator, respectively, and r_e is the internuclear distance. [99][39][100][101]

to considerable collisional cooling. In our case, the residual pressure of the ion source is several orders of magnitude smaller, and the cooling is therefore negligible so that a temperature larger than 350 K is presumably to be expected.

In the 2055 nm case for Ag_2^-, the ratio between the amplitude of the calculated 2- and 3-photon detachment is set to the corresponding ratio in the experimental data. The discrepancy between the measured and calculated values for the position of the maximum of the 3-photon transition is 322, 340 and 406 meV for 300, 1000 and 3000 K, respectively (see Fig. 7.12). This could be accounted for by a ponderomotive shift corresponding to intensities of 8.15×10^{11}, 8.61×10^{11} and 1.03×10^{12} W/cm^2, an order of magnitude smaller than the peak intensity of 9.6×10^{12} W/cm^2. This suggests that detachment occurs at the leading edge of the pulse. A shift of the entire calculated photoelectron distributions by these ponderomotive energies would eliminate the non-monotonic behavior of the simulated 2-photon transition. The experimentally obtained distribution for 1310 nm is wider than the calculated one (see Fig. 7.11). One contributing factor to the experimental widening is that every electron impact event on the detector creates a signal with a FWHM of 7.5 pixels in the experimental image[103].

The above results for dicarbon and disilicon show that the difference between the dressed and undressed versions of the theory is small. Determining which version of the theory describes the process better is difficult to do, as an experimental widening of the simulated images would even out the differences. Especially in the C_2^- cases, the model simulations are very similar to each other. In the Si_2^- case the difference between the dressed and undressed simulations is larger, with the dressed version agreeing better with experiment. The larger difference is what is expected in light of the internuclear distances of the initial states of the two molecular species ($R_0(\mathrm{C}_2^-) \approx 1.27$ Å, $R_0(\mathrm{Si}_2^-) \approx 2.12$ Å) as the effect of dressing the initial state increases with increasing distance.

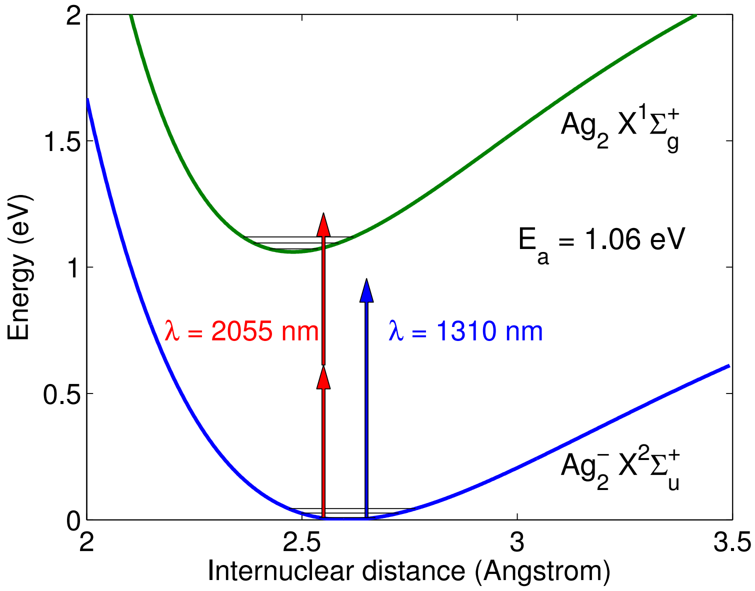

Figure 7.15: Qualitative potential curves for Ag_2^- mentioned in the text. The arrows represent the minimum amount of photons necessary for photodetachment.

The general trend is that the accuracy of the simulations improves as the number of photons required to induce the photodetachment process increases. The 6 and 4 minimum photons necessary in the C_2^- 2055 and 1310 nm cases, as well as the minimum 4 photons in the Si_2^- 1985 nm case prove to be well reproduced in simulations. For the 1340 nm case for Si_2^-, where 3 photons are necessary, the agreement is smaller and for the 1- and 2-photon processes in Ag_2^-, the simulations fail altogether and a different approach is required.

It should be pointed out that there could be a small contribution from photoionization of the neutral molecule, as well as contributions from the negative ion and neutral of the corresponding atomic species, produced through photodissociation early in the pulse. Such processes were neglected in the above simulations. Inclusion of more electronic and vibrational transitions could also improve the accuracy.

7.5 Conclusion

In this chapter a study of strong-field photodetachment of homonuclear diatomic negative ions has been performed. Measurements were performed for three different molecular species, namely C_2^-, Si_2^- and Ag_2^-, for two different laser wavelengths each. The

	State	T_e (eV)	ω_e (cm^{-1})	$\omega_\mathrm{e}x_\mathrm{e}$ (cm^{-1})	r_e (Å)
Ag_2^-	$X^2\Sigma_\mathrm{u}^+(\sigma_\mathrm{g}^2\sigma_\mathrm{u}^1)$	0	145(10)	[0.9]	2.604(7)
Ag_2	$X^1\Sigma_\mathrm{g}^+(\sigma_\mathrm{g}^2\sigma_\mathrm{u}^0)$	0	192.4	0.60	2.480
	$a^3\Sigma_\mathrm{u}(\sigma_\mathrm{g}^1\sigma_\mathrm{u}^1)$	[≤1.74]	...	...	...

Table 7.3: The first few electronic states for Ag_2^- and Ag_2. EA (Ag_2) = 1.06(2) eV. T_e is the electronic excitation energy relative to the ground state, ω_e and $\omega_e x_e$ are the linear and quadratic expansion coefficients for the vibrational energy in an anharmonic oscillator, respectively, and r_e is the internuclear distance. [102]

experimental measurements were compared to simulations of models of strong-field photodetachment in the two former species, and a calculation based on the strength of vibrational transitions in the latter. We conclude that the difference between the two strong-field models is small for C_2^- but that the dressed version of the theory agrees better with theory for Si_2^-. It can also be seen that with an increasing amount of photons necessary for detachment, the accuracy of the simulations improves. This can be expected as an increasing number of photons required to induce the photodetachment process necessarily takes us deeper into the strong-field regime. It should be noted that extended versions of the model for strong-field detachment exist, e.g. [104], where rescattering effects are taken into account. This could perhaps help explain the high energy jets present in the experimental data in Figs. 7.1, 7.5 and 7.7, but other than that, no significant improvement is to be expected.

Chapter 8

Conclusion and Outlook

This thesis has explored fundamental topics in photoelectron imaging and strong-field photodetachment of atomic and molecular negative ions as well as the experimental realization and the theoretical modeling of bound-state electronic wave packets in the ground-state of atoms.

In chapter 5 the orbital alignment dynamics of atoms created through strong-field photodetachment of a negative ion in the carbon group was studied. Atoms were prepared by strong-field detachment of the corresponding negative ion. The laser preferentially detaches $\mathrm{m}_\ell = 0$ electrons from the valence shell, thereby causing an orbital alignment in the atom. After a variable time delay the atom was ionized by a second strong-field laser pulse and the photoelectron distribution was recorded. The angle resolved momentum distribution of electrons produced in the photoionization step provides a probe of the electron density distribution in the atom. The results show that for carbon and silicon a wave packet is created manifesting as a beat in the angular part of the electron probability density. This shows that a coherent alignment of atomic orbitals has taken place. For germanium, however, due to the duration of both the pump and probe laser pulses being longer than that of the spin-orbit period, only a non-coherent alignment effect could be detected. The implemented method is general and the creation of vibrational wave packets in molecules is an interesting possible application. There is no sign of decoherence of the wave packet on the time scale of the present experiment. An extension to the presented study measuring the decoherence time of the would be of interest. A theoretical model for the beat using a density matrix approach was developed and was shown to be in good agreement with the experiment.

In chapter 6 a tomographic method for recording the full three-dimensional distribution of photoelectrons was developed. The method does not assume any symmetries of the photoelectron distribution and can therefore be used for any laser field polarization. The method was applied to photodetachment of Ag^- and compared to theory. A lack of mirror symmetry in the polarization plane was discovered and was found to be explainable by a residual elliptical polarization of the laser field. Such a residual elliptical polarization is not detectable using traditional inversion methods. The combination of the tomographic method with the pump-probe experiment in chapter 5 could provide more insight into the alignment dynamics in atoms created through strong-field photodetachment. By being able to select the region of interest with larger precision, thereby increasing the signal-to-background ratio, the detection of a weaker oscillation would be possible. In addition to this, to definitely determine elliptical polarization as the cause of the recorded asymmetry, a study of the photoelectron distribution dependence on the polarization ellipticity parameter would represent an interesting topic for further study.

In addition to the experimental results above, in Chapter 2 an SFA model for strong-field photodetachment was generalized to elliptical polarization. The model coincides with existing models for linear and circular polarization. It was however found to be insufficient to explain the experimentally observed lack of mirror symmetry in the plane perpendicular to the laser propagation axis as a consequence of elliptical polarization. This is due to the fact that in order to induce an asymmetry, the interaction between the detached electron and the residual core needs to be taken into account, something which is neglected in basic SFA theories.

Chapter 7 provides a comparison of experimental data for diatomic homonuclear negative ions to that of two theoretical models for strong-field photodetachment of homonuclear molecular negative ions. In the dressed version of the theory, the potential difference between the two atomic cores is taken into account, whereas for the undressed version it is neglected. The results show that for the cases tested, there is little difference between the two models and neither model can unequivocally be declared to be preferred. The dressed version of the theory does however agree better with the experimental results for photodetachment of Si_2^- at a wavelength of 1985 nm. In addition to this, both models increase in accuracy with increasing amount of photons needed to overcome the photodetachment threshold. Since the results of the dressed and undressed versions of the theory diverge for larger internuclear distances, a study of molecular species with a larger range of internuclear separations would be of interest to shed more light in which range each model is applicable.

Acknowledgments

First I would like to thank Hanspeter Helm for letting me into his group and for his eagerness to discuss problems in physics and non-physics alike. Thank you to Dag Hanstorp for telling me about the open position and providing good advice first unofficially and at a later stage also officially. Thank you to Igor Kiyan for his seemingly infinite patience in keeping the laser in the best possible shape and the reverse Russian page ordering theoretical treatments that simplified my life immensely. A big thank you to Hannes Hultgren for convincing me to join the negative ion project so that we could continue the synergistic collaboration we had for many years during our undergraduate studies.

Thank you to present and (in an overwhelming majority these days) past members of the Helm group. There was always someone to engage in a conversation about physics or share a beer with. Marion, Isabella and Uwe eased the burden of administrative and technical issues.

Thank you to the ICONIC network EU-ITN 238671 for funding and unforgettable conferences. Thank you to Anthony Starace and Mikhail Frolov for supplying advice and Fortran code for the QQES simulation. The competent work of the mechanical and electronic workshops was invaluable for setting up the experiments.

Thank you to my parents and brother with family for always believing in me although they never really understood what it was that I was doing. The international community of Freiburg was welcoming from the very beginning and eased the move to a new country.

Last but definitely not least I would like to thank my partner in crime Sanjana Rao. Thanks for putting up with me during these years and last few months in particular. Without your love and encouragement this would just not have happened.

Appendix A

Effects on Polarization Ellipticity Passing Through a Retarder Plate

In this appendix it will be described how a waveplate affects the polarization of a laser beam and how to calculate the ellipticity as well as the semi-major and semi-minor axes of the polarization ellipse of the resulting electric field.

The general case of an elliptically polarized incoming electric field can be described by a Jones vector of the form

$$\mathbf{E}_{\text{in}} = \begin{pmatrix} 1 \\ i\varepsilon_{\text{in}} \end{pmatrix}. \tag{A.1}$$

The effect of passing through a waveplate with retardance Γ with its fast axis oriented at an angle α with the x-axis is given by

$$\mathbf{E} = \mathrm{R}\mathrm{W}\mathrm{R}^{-1}\mathbf{E}_{\text{in}}, \tag{A.2}$$

where

$$\mathrm{R} = \begin{pmatrix} \cos(\alpha) & -\sin(\alpha) \\ \sin(\alpha) & \cos(\alpha) \end{pmatrix} \tag{A.3}$$

is a rotation matrix. The matrix

$$\mathrm{W} = \begin{pmatrix} 1 & 0 \\ 0 & e^{i\Gamma} \end{pmatrix} \tag{A.4}$$

phase-shifts the component of the electric field parallel to the slow axis by Γ.

The resulting electric field can be decomposed into a real and imaginary part

$$\mathbf{E} = \mathbf{E}_{\text{re}} + i\mathbf{E}_{\text{im}}, \tag{A.5}$$

with $\mathbf{E}_{\mathrm{re}}$ and $\mathbf{E}_{\mathrm{im}}$ being real vectors. Multiplying $\mathbf{E}$ with a time-harmonic exponential $e^{-i\omega t}$ and taking the real part defines an ellipse in the xy-plane. Note that $\mathbf{E}_{\mathrm{re}}$ and $\mathbf{E}_{\mathrm{im}}$ are not perpendicular to each other in the general case.

In order to calculate the semi-major and semi-minor axes of the ellipse as well as its ellipticity, we first note that a phase-shifted complex vector of the form

$$\mathbf{F} = e^{i\varphi}\mathbf{E} \tag{A.6}$$

defines the same ellipse in the xy-plane as $\mathbf{E}$. Finding the major and minor axes of the ellipse is equivalent to finding a phase φ such that the real component of $\mathbf{F}$ is perpendicular to its imaginary component. The solution to this problem is

$$\mathbf{F} = \frac{|\sqrt{\mathbf{E}\cdot\mathbf{E}}|}{\sqrt{\mathbf{E}\cdot\mathbf{E}}}\mathbf{E}. \tag{A.7}$$

This solution can be justified by taking the scalar product of $\mathbf{F}$ with itself

$$\mathbf{F}\cdot\mathbf{F} = \mathbf{F}_{\mathrm{re}}\cdot\mathbf{F}_{\mathrm{re}} - \mathbf{F}_{\mathrm{im}}\cdot\mathbf{F}_{\mathrm{im}} + 2i\mathbf{F}_{\mathrm{re}}\cdot\mathbf{F}_{\mathrm{im}} = |\sqrt{\mathbf{E}\cdot\mathbf{E}}|^2, \tag{A.8}$$

which is a real number and $\mathbf{F}_{\mathrm{re}}\cdot\mathbf{F}_{\mathrm{im}}$ must thus be identically zero and the components are perpendicular. The solution can be written as in Eq. (A.6) since the prefactor is the reciprocal of a complex number divided by its absolute value.

It can be shown that $\mathbf{F}_{\mathrm{re}}$ and $\mathbf{F}_{\mathrm{im}}$ are indeed the semi-major and semi-minor axes by looking at the absolute value of the real time-harmonic field

$$|\operatorname{Re}(\mathbf{F}e^{-i\omega t})| = \sqrt{\mathbf{F}_{\mathrm{re}}\cdot\mathbf{F}_{\mathrm{re}}\cos^2(\omega t) + \mathbf{F}_{\mathrm{im}}\cdot\mathbf{F}_{\mathrm{im}}\sin^2(\omega t)}, \tag{A.9}$$

which has extreme values of $|\mathbf{F}_{\mathrm{re}}|$ and $|\mathbf{F}_{\mathrm{im}}|$.

The ellipticity of the outgoing laser beam is given by

$$\varepsilon_{\mathrm{out}} = \frac{1}{\mathbf{F}_{\mathrm{re}}\cdot\mathbf{F}_{\mathrm{re}}}(\mathbf{F}_{\mathrm{re}}\times\mathbf{F}_{\mathrm{im}})\cdot\hat{\mathbf{z}}, \tag{A.10}$$

where the cross product is taken on the three-dimensional extension of the vectors, and $\hat{\mathbf{z}}$ is the unit vector in the propagation direction of the laser.

The waveplate used in the experiments described in this thesis is nominally a half-wave plate. The retardance at 1310 nm is specified by the manufacturer to be

$$\Gamma = 0.49292\cdot 2\pi. \tag{A.11}$$

Light passing through the waveplate deviates in its ellipticity by

$$\Delta\varepsilon = \varepsilon_{\text{out}} + \varepsilon_{\text{in}} \tag{A.12}$$

from the value of a half-wave plate. The plus sign here is because the ellipticity is expected to change its sign. The deviation in the outgoing ellipticity as a function of the waveplate orientation for a few values of the incoming ellipticity is shown in Fig. A.1.

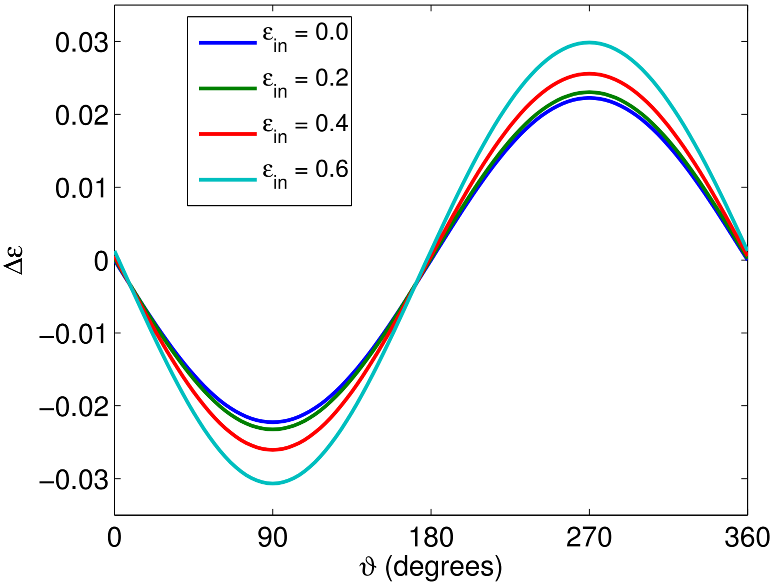

Figure A.1: The deviation in the ellipticity parameter ε as a function of the nominal angle of orientation of the polarization major axis ϑ

Fig. A.2 shows the deviation from the nominal angle given by

$$\Delta\vartheta = \vartheta_{\text{out}} - 2\alpha, \tag{A.13}$$

where ϑ_{out} is the angle $\mathbf{F}_{\text{re}}$ makes with the x-axis. The meaning of nominal angle here is the angle which the major axis of the incoming elliptical polarization would rotate were the waveplate a perfect half-wave plate.

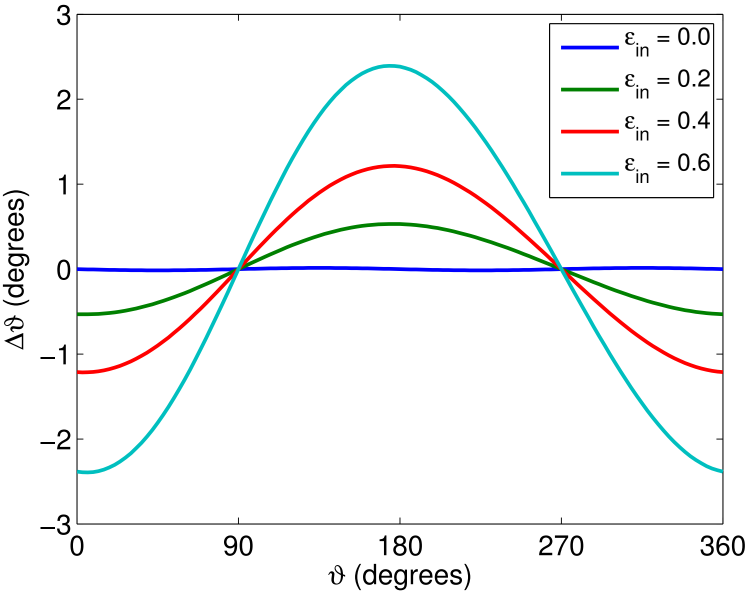

Figure A.2: The deviation in the major axis orientation as a function of the nominal angle of orientation of the polarization major axis ϑ

Appendix B

Discussion of the Lack of Mirror Symmetry in the Polarization Plane

The following appendix is a discussion of possible explanations for the lack of mirror symmetry in the polarization plane for strong-field photodetachment of Ag^- at 1310 nm in Chap. 6.

The first set of possible causes to consider are shortcomings in the design, machining and assembly of the electron imaging spectrometer as well defects in the detector. Examples of this are inhomogeneities in the projection fields; damages to the MCPs and phosphor screen or readout effects of the CCD camera causing the detector response to be position dependent; and that kinematic effects associated with the moving ions would have a skewing effect on the distribution. The effects of the mentioned potential causes would be clearly visible in the raw data, however. With the exception of a slightly higher signal in the downstream direction of the ion beam, no sign of severe inhomogeneities in the direction corresponding to the polarization axis can be seen. Artificial introduction of inhomogeneities of this kind was tested in simulations and produces no asymmetry in the recreated polarization plane distribution. The reason for this can be easily understood by considering two individual portions, let's call them portion A and B, of the electron swarm ejected through the two-photon process. For simplicity we assume that the portions lie on a circle of constant radius in the center plane swept out by the polarization of the rotated laser beam, the circle passing through the maximum of the swarm density ($p = p_{max} \approx 0.187, \phi = 0$). Let portion A lie in the cap along the laser polarization direction, i.e. at $\theta = 0$, and let portion B lie in the torus, i.e. $\theta = 90°$. Portion A will thus be exposed to the projection and detection conditions at angles $0°, 3°, \ldots, 357°$ and portion B will be subject to the conditions at $90°, 93°, \ldots, 447° (= 87°)$. Since the laser polarization vector is rotated 360 degrees, the portions A and B will thus be subject to exactly the same conditions, shifted by 90 degrees. Introducing a shift in the inverse Radon transform merely rotates the recreated object without any distortions, so it would be impossible to introduce the observed asymmetry in this way. The above argument relies on the assumption that the response of the detector is the same for both portions, independent of hits from electrons from the surrounding electron swarm. This is a reasonable assumption since the electron count rate is of the order of 5000 counts per second where the detector response is close to linear.

Another possible origin of the asymmetry is that the laser polarization is slightly elliptical. This could be produced either by the waveplate used to rotate the polarization or prior to the waveplate. The waveplate used is achromatic, meaning that its phase retardation of the component parallel to the slow axis is not exactly π relative to the fast axis. For a wavelength of 1310 nm, the phase shift Γ is $0.49292 \times 2\pi$ according to the manufacturer. The ellipticity induced by the waveplate is not constant but varies with the angle. Aside from this, the waveplate also introduces an error in the rotational angle from the nominal one. The meaning of nominal angle here is the angle which the major axis of the incoming elliptical polarization would rotate were the waveplate a perfect half-wave plate. For details on how to calculate these errors, please see Appendix A. The errors depend on the ellipticity of the incoming beam. Figures A.1 and A.2 show the dependence on the nominal angle of the ellipticity- and angular errors, respectively, for a few values of the incoming ellipticity parameter $\varepsilon_{\mathrm{in}}$.

Disregarding the slight offset, it can be seen in Fig. A.1 that the polarization is virtually unaffected at 0 and 180 degrees, with the deviation reaching its minimum and maximum at 90 and 270 degrees, respectively. For an incoming linear polarization, the outgoing ellipticity has different sign for the intervals 0-180 and 180-360. The fact that we acquire images over 360 degrees means that half the experimental images are recorded for a handedness corresponding to a right-handed rotation of the electric field and half for a left-handed rotation. This means that any asymmetry introduced in one of the intervals would be exactly compensated for by an equally large and opposite asymmetry in the other interval. Since it is enough to use projections over an interval of 180 degrees to fully recreate the original distribution, it is possible to use only half of the images for the reconstruction. The angular position of maxima would thus vary between different reconstruction intervals in case the wave-plate induced ellipticity was the causing factor. Figure B.1 shows the angular distribution of electrons in the polarization plane for reconstructions made for a few different intervals. The figure shows the density on a circle with radius $p = 0.187$ in the central polarization plane. The polar maxima have been aligned to the z-axis. It can be seen that the equatorial maximum deviates approximately -5 degrees from the expected value of 90 degrees, irrespective of the interval used and we thus conclude that the waveplate-induced ellipticity error cannot be the cause. The asymmetry in the peak values for opposing maxima when using data from a half rotation is caused by the taller peak being downstream in the ion beam in all of the used images.

The effect of the angular error shown in Fig. A.2 is more difficult to assess. To exclude this as the effect causing the asymmetry in the electron distribution, we perform an individual simulation of the Gribakin/Kuchiev theory developed in Sec. 2.3 with the calculated ellipticity and real rotation angle, project these simulated distributions and Radon-invert using the nominal angles. As can be seen in figure B.2, this does not introduce any asymmetry. This was performed up to an incoming ellipticity of 0.6, since it is only then that an angular error of the same order as the asymmetry appears. As a consequence we conclude that the most probable explanation of the asymmetry is an ellipticity of the polarization already present in the laser beam before the waveplate. The QQES simulation in Chap. 6 shows that the asymmetry is consistent with an ellipticity of $\varepsilon = 0.21$.

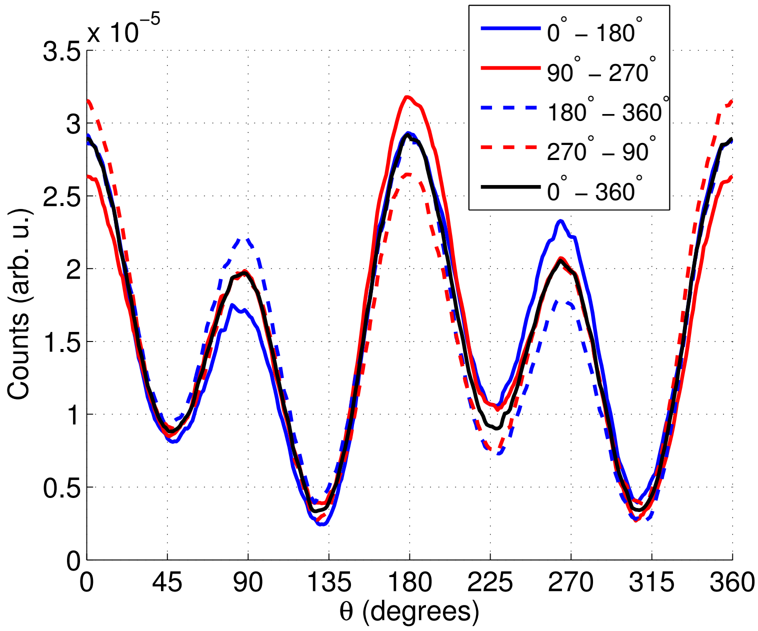

Figure B.1: Reconstruction of the photoelectron angular distribution at $p = 0.187$ for different intervals of the projection angle.

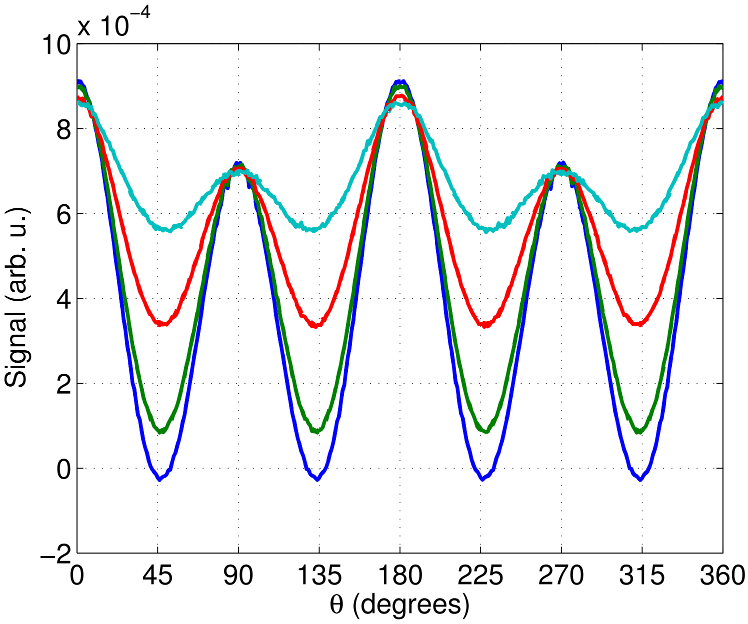

Figure B.2: Simulated angular electron distribution at a momentum of $p = 1.87$, taking waveplate induced aberrations into account. Color coding as in Fig. A.2.

Bibliography

[1] H. Hertz. Ueber einen einfluss des ultravioletten lichtes auf die electrische entladung. *Annalen der Physik*, 267(8):983–1000, 1887. ISSN 1521-3889. doi:10.1002/andp.18872670827. URL `http://dx.doi.org/10.1002/andp.18872670827`.

[2] A. Einstein. über einen die erzeugung und verwandlung des lichtes betreffenden heuristischen gesichtspunkt. *Annalen der Physik*, 322(6):132–148, 1905. ISSN 1521-3889. doi:10.1002/andp.19053220607. URL `http://dx.doi.org/10.1002/andp.19053220607`.

[3] P. Lenard. Ueber wirkungen des ultravioletten lichtes auf gasförmige körper. *Annalen der Physik*, 306(3):486–507, 1900. ISSN 1521-3889. doi:10.1002/andp.19003060308. URL `http://dx.doi.org/10.1002/andp.19003060308`.

[4] Lewis M. Branscomb and W. L. Fite. Photodetachment of the hydrogen negative ion. *Phys. Rev.*, 93:951 (A), May 1954. doi:10.1103/PhysRev.93.647. URL `http://link.aps.org/doi/10.1103/PhysRev.93.647`.

[5] Lewis M. Branscomb and Stephen J. Smith. Experimental cross section for photodetachment of electrons from H^- and D^-. *Phys. Rev.*, 98:1028–1034, Feb 1955. doi:10.1103/PhysRev.98.1028. URL `http://link.aps.org/doi/10.1103/PhysRev.98.1028`.

[6] Lewis M. Branscomb and Stephen J. Smith. Electron affinity of atomic oxygen. *Phys. Rev.*, 98:1127–1128, May 1955. doi:10.1103/PhysRev.98.1127. URL `http://link.aps.org/doi/10.1103/PhysRev.98.1127`.

[7] B. Brehm, M. A. Gusinow, and J. L. Hall. Electron affinity of helium via laser photodetachment of its negative ion. *Phys. Rev. Lett.*, 19:737–741, Sep 1967. doi:10.1103/PhysRevLett.19.737. URL `http://link.aps.org/doi/10.1103/PhysRevLett.19.737`.

[8] J. Cooper and R. N. Zare. Angular distribution of photoelectrons. *The Journal of Chemical Physics*, 48(2):942–943, 1968. doi:10.1063/1.1668742. URL `http://scitation.aip.org/content/aip/journal/jcp/48/2/10.1063/1.1668742`.

[9] J. L. Hall and M. W. Siegel. Angular dependence of the laser photodetachment of the negative ions of carbon, oxygen, and hydrogen. *The Journal of Chemical Physics*, 48(2):943–945, 1968. doi:10.1063/1.1668743. URL `http://scitation.aip.org/content/aip/journal/jcp/48/2/10.1063/1.1668743`.

[10] H. Helm, N. Bjerre, M. J. Dyer, M. Saeed, and D. L. Huestis. Experimental visualization of photoelectron angular distributions. *AIP Conference Proceedings*, 295(1):779–785, 1993. doi:10.1063/1.45246. URL `http://scitation.aip.org/content/aip/proceeding/aipcp/10.1063/1.45246`.

[11] H. Helm, N. Bjerre, M. J. Dyer, D. L. Huestis, and M. Saeed. Images of photoelectrons formed in intense laser fields. *Phys. Rev. Lett.*, 70:3221–3224, May 1993. doi:10.1103/PhysRevLett.70.3221. URL `http://link.aps.org/doi/10.1103/PhysRevLett.70.3221`.

[12] Christophe Blondel, Christian Delsart, and François Dulieu. The photodetachment microscope. *Phys. Rev. Lett.*, 77:3755–3758, Oct 1996. doi:10.1103/PhysRevLett.77.3755. URL `http://link.aps.org/doi/10.1103/PhysRevLett.77.3755`.

[13] C. Bordas, F. Paulig, H. Helm, and D. L. Huestis. Photoelectron imaging spectrometry: Principle and inversion method. *Review of Scientific Instruments*, 67 (6):2257–2268, 1996. doi:10.1063/1.1147044. URL `http://scitation.aip.org/content/aip/journal/rsi/67/6/10.1063/1.1147044`.

[14] Andre T. J. B. Eppink and David H. Parker. Velocity map imaging of ions and electrons using electrostatic lenses: Application in photoelectron and photofragment ion imaging of molecular oxygen. *Review of Scientific Instruments*, 68(9):3477–3484, 1997. doi:10.1063/1.1148310. URL `http://scitation.aip.org/content/aip/journal/rsi/68/9/10.1063/1.1148310`.

[15] T. H. Maiman. Stimulated optical radiation in ruby. *Nature*, 187(4736):493–494, Aug 1960. doi:10.1038/187493a0. URL `http://dx.doi.org/10.1038/187493a0`.

[16] Fritz P. Schäfer, Werner Schmidt, and Jürgen Volze. Organic dye solution laser. *Applied Physics Letters*, 9(8):306–309, 1966. doi:10.1063/1.1754762. URL `http://scitation.aip.org/content/aip/journal/apl/9/8/10.1063/1.1754762`.

[17] H. Hotop and W. C. Lineberger. Binding energies in atomic negative ions. *Journal of Physical and Chemical Reference Data*, 4(3):539–576, 1975. doi:10.1063/1.555524. URL `http://scitation.aip.org/content/aip/journal/jpcrd/4/3/10.1063/1.555524`.

[18] D. E. Spence, P. N. Kean, and W. Sibbett. 60-fsec pulse generation from a self-mode-locked ti:sapphire laser. *Opt. Lett.*, 16(1):42–44, Jan

1991. doi:10.1364/OL.16.000042. URL `http://ol.osa.org/abstract.cfm?URI=ol-16-1-42`.

[19] P. M. W. French, J. A. R. Williams, and J. R. Taylor. Femtosecond pulse generation from a titanium-doped sapphire laser using nonlinear external cavity feedback. *Opt. Lett.*, 14(13):686–688, Jul 1989. doi:10.1364/OL.14.000686. URL `http://ol.osa.org/abstract.cfm?URI=ol-14-13-686`.

[20] J. Goodberlet, P. A. Schulz, J. Wang, and J. G. Fujimoto. Femtosecond passively mode-locked ti:al2o3 laser with a nonlinear external cavity. *Opt. Lett.*, 14(20):1125–1127, Oct 1989. doi:10.1364/OL.14.001125. URL `http://ol.osa.org/abstract.cfm?URI=ol-14-20-1125`.

[21] D. Strickland and G. Mourou. Compression of amplified chirped optical pulses. *Optics Communications*, 56:219–221, December 1985. doi:10.1016/0030-4018(85)90120-8.

[22] P. Agostini, F. Fabre, G. Mainfray, G. Petite, and N. K. Rahman. Free-free transitions following six-photon ionization of xenon atoms. *Phys. Rev. Lett.*, 42:1127–1130, Apr 1979. doi:10.1103/PhysRevLett.42.1127. URL `http://link.aps.org/doi/10.1103/PhysRevLett.42.1127`.

[23] C Blondel, M Crance, C Delsart, and A Giraud. Excess-photon absorption in a negative ion. *Journal of Physics B: Atomic, Molecular and Optical Physics*, 24 (16):3575, 1991. URL `http://stacks.iop.org/0953-4075/24/i=16/a=010`.

[24] John A. Yeazell and C. R. Stroud Jr. Observation of spatially localized atomic electron wave packets. *Phys. Rev. Lett.*, 60:1494–1497, Apr 1988. doi:10.1103/PhysRevLett.60.1494. URL `http://link.aps.org/doi/10.1103/PhysRevLett.60.1494`.

[25] A. ten Wolde, L. D. Noordam, A. Lagendijk, and H. B. van Linden van den Heuvell. Observation of radially localized atomic electron wave packets. *Phys. Rev. Lett.*, 61:2099–2101, Oct 1988. doi:10.1103/PhysRevLett.61.2099. URL `http://link.aps.org/doi/10.1103/PhysRevLett.61.2099`.

[26] Stefan Gilb, Elva A Torres, and Stephen R Leone. Mapping of time-dependent electron orbital alignment. *Journal of Physics B: Atomic, Molecular and Optical Physics*, 39(20):4231, 2006. doi:10.1088/0953-4075/39/20/020. URL `http://stacks.iop.org/0953-4075/39/i=20/a=020`.

[27] S. Zamith, M.A. Bouchene, E. Sokell, C. Nicole, V. Blanchet, and B. Girard. Pump probe experiment in atomic fine structure levels: Observation of the oscillation of an angular wavepacket. *Eur. Phys. J. D*, 12:255–261, Nov 2000. doi:10.1007/s100530070020.

[28] Qun Zhang and John W. Hepburn. In situ accurate determination of the zero time delay between two independent ultrashort laser pulses by observing the oscillation of an atomic excited wave packet. *Optics Letters*, 33:1893–1895, 2008. doi:10.1364/OL.33.001893.

[29] A. Fleischer, H. J. Wörner, L. Arissian, L. R. Liu, M. Meckel, A. Rippert, R. Dörner, D. M. Villeneuve, P. B. Corkum, and A. Staudte. Probing angular correlations in sequential double ionization. *Phys. Rev. Lett.*, 107:113003, Sep 2011. doi:10.1103/PhysRevLett.107.113003. URL `http://link.aps.org/doi/10.1103/PhysRevLett.107.113003`.

[30] Eleftherios Goulielmakis, Zhi-Heng Loh, Adrian Wirth, Robin Santra, Nina Rohringer, Vladislav S. Yakovlev, Sergey Zherebtsov, Thomas Pfeifer, Abdallah M. Azzeer, Matthias F. Kling, Stephen R. Leone, and Ferenc Krausz. Real-time observation of valence electron motion. *Nature*, 466(7307):739–743, Aug 2010. ISSN 0028-0836. doi:10.1038/nature09212. URL `http://dx.doi.org/10.1038/nature09212`.

[31] C Smeenk, L Arissian, A Staudte, D M Villeneuve, and P B Corkum. Momentum space tomographic imaging of photoelectrons. *Journal of Physics B: Atomic, Molecular and Optical Physics*, 42(18):185402, 2009. URL `http://stacks.iop.org/0953-4075/42/i=18/a=185402`.

[32] Hannes Hultgren and Igor Yu. Kiyan. Photodetachment dynamics of F_2^- in a strong laser field. *Phys. Rev. A*, 84:015401, Jul 2011. doi:10.1103/PhysRevA.84.015401. URL `http://link.aps.org/doi/10.1103/PhysRevA.84.015401`.

[33] David J Pegg. Structure and dynamics of negative ions. *Reports on Progress in Physics*, 67(6):857, 2004. URL `http://stacks.iop.org/0034-4885/67/i=6/a=R02`.

[34] George Gioumousis and D. P. Stevenson. Reactions of gaseous molecule ions with gaseous molecules. v. theory. *The Journal of Chemical Physics*, 29(2):294–299, 1958. doi:10.1063/1.1744477. URL `http://scitation.aip.org/content/aip/journal/jcp/29/2/10.1063/1.1744477`.

[35] René C. Bilodeau and Harold K. Haugen. Experimental studies of Os^-: Observation of a bound-bound electric dipole transition in an atomic negative ion. *Phys. Rev. Lett.*, 85:534–537, Jul 2000. doi:10.1103/PhysRevLett.85.534. URL `http://link.aps.org/doi/10.1103/PhysRevLett.85.534`.

[36] C. W. Walter, N. D. Gibson, C. M. Janczak, K. A. Starr, A. P. Snedden, R. L. Field III, and P. Andersson. Infrared photodetachment of Ce^-: Threshold spectroscopy and resonance structure. *Phys. Rev. A*, 76:052702, Nov 2007.

doi:10.1103/PhysRevA.76.052702. URL `http://link.aps.org/doi/10.1103/PhysRevA.76.052702`.

[37] W. Walter, C. D. Gibson, N. J. Matyas, D. C. Crocker, A. Dungan, K. R. Matola, B. and J. Rohlén. Candidate for laser cooling of a negative ion: Observations of bound-bound transitions in La$^-$. *Phys. Rev. Lett.*, 113:063001, Aug 2014. doi:10.1103/PhysRevLett.113.063001. URL `http://link.aps.org/doi/10.1103/PhysRevLett.113.063001`.

[38] Brent D. Rehfuss, DiJia Liu, Bianca M. Dinelli, MaryFrances Jagod, Wing C. Ho, Mark W. Crofton, and Takeshi Oka. Infrared spectroscopy of carboions. iv. the $A^2\Pi_u - X^2\Sigma_g^+$ electronic transition of C_2^-. *The Journal of Chemical Physics*, 89(1):129–137, 1988. doi:10.1063/1.455731. URL `http://scitation.aip.org/content/aip/journal/jcp/89/1/10.1063/1.455731`.

[39] Zhuan Liu and Paul B. Davies. Infrared laser spectroscopy of the $A^2\Pi_u \leftarrow X^2\Sigma_g^+$ system of the Si_2^- anion. *The Journal of Chemical Physics*, 105(9):3443–3449, 1996. doi:10.1063/1.472214. URL `http://scitation.aip.org/content/aip/journal/jcp/105/9/10.1063/1.472214`.

[40] *Atomic, Molecular, and Optical Physics Handbook.* American Institute of Physics, 1996. ISBN 156396242X.

[41] A. Ludwig, J. Maurer, W. Mayer, B. R. Phillips, C. L. Gallmann, and U. Keller. Breakdown of the dipole approximation in strong-field ionization. *Phys. Rev. Lett.*, 113:243001, Dec 2014. doi:10.1103/PhysRevLett.113.243001. URL `http://link.aps.org/doi/10.1103/PhysRevLett.113.243001`.

[42] J D Rudmin, L P Ratliff, J N Yukich, and D J Larson. Structure of the photodetachment cross section in a magnetic field: an experiment with OH$^-$. *Journal of Physics B: Atomic, Molecular and Optical Physics*, 29(24):L881, 1996. URL `http://stacks.iop.org/0953-4075/29/i=24/a=004`.

[43] V.K. Ivanov. Theoretical studies of photodetachment. *Radiation Physics and Chemistry*, 70(1-3):345 – 370, 2004. ISSN 0969-806X. doi:10.1016/j.radphyschem.2003.12.020. URL `http://www.sciencedirect.com/science/article/pii/S0969806X03006583`. Photoeffect: Theory and Experiment.

[44] Eugene P. Wigner. On the behavior of cross sections near thresholds. *Phys. Rev.*, 73:1002–1009, May 1948. doi:10.1103/PhysRev.73.1002. URL `http://link.aps.org/doi/10.1103/PhysRev.73.1002`.

[45] L.V. Keldysh. Ionization in the field of a strong electromagnetic wave. *Journal of Experimental and Theoretical Physics*, 20(5):1307, 1965. URL `http://www.jetp.ac.ru/cgi-bin/e/index/e/20/5/p1307?a=list`.

[46] G. F. Gribakin and M. Yu. Kuchiev. Multiphoton detachment of electrons from negative ions. *Phys. Rev. A*, 55:3760–3771, May 1997. doi:10.1103/PhysRevA.55.3760. URL `http://link.aps.org/doi/10.1103/PhysRevA.55.3760`.

[47] F H M Faisal. Multiple absorption of laser photons by atoms. *Journal of Physics B: Atomic and Molecular Physics*, 6(4):L89, 1973. URL `http://stacks.iop.org/0022-3700/6/i=4/a=011`.

[48] Howard R. Reiss. Effect of an intense electromagnetic field on a weakly bound system. *Phys. Rev. A*, 22:1786–1813, Nov 1980. doi:10.1103/PhysRevA.22.1786. URL `http://link.aps.org/doi/10.1103/PhysRevA.22.1786`.

[49] Yu.N. Demkov and V.N. Ostrovskii. *Zero-Range Potentials and their Applications in Atomic Physics*. Plenum Press, New York, 1988. URL `http://dx.doi.org/10.1007/978-1-4684-5451-2`.

[50] G F Gribakin and M Yu Kuchiev. Multiphoton detachment from negative ions: new theory versus experiment. *Journal of Physics B: Atomic, Molecular and Optical Physics*, 30(19):L657, 1997. URL `http://stacks.iop.org/0953-4075/30/i=19/a=005`.

[51] D. B. Milošević. Strong-field approximation for ionization of a diatomic molecule by a strong laser field. *Phys. Rev. A*, 74:063404, Dec 2006. doi:10.1103/PhysRevA.74.063404. URL `http://link.aps.org/doi/10.1103/PhysRevA.74.063404`.

[52] A. Gazibegović-Busuladžić, D. B. Milošević, W. Becker, B. Bergues, H. Hultgren, and I. Yu. Kiyan. Electron rescattering in above-threshold photodetachment of negative ions. *Phys. Rev. Lett.*, 104:103004, Mar 2010. doi:10.1103/PhysRevLett.104.103004. URL `http://link.aps.org/doi/10.1103/PhysRevLett.104.103004`.

[53] Svea Beiser, Michael Klaiber, and Igor Yu. Kiyan. Photodetachment in a strong circularly polarized laser field. *Phys. Rev. A*, 70:011402, Jul 2004. doi:10.1103/PhysRevA.70.011402. URL `http://link.aps.org/doi/10.1103/PhysRevA.70.011402`.

[54] Boris Bergues, Zunaira Ansari, Dag Hanstorp, and Igor Yu. Kiyan. Photodetachment in a strong laser field: An experimental test of keldysh-like theories.

Phys. Rev. A, 75:063415, Jun 2007. doi:10.1103/PhysRevA.75.063415. URL `http://link.aps.org/doi/10.1103/PhysRevA.75.063415`.

[55] Boris Bergues, Zunaira Ansari, Dag Hanstorp, and Igor Yu. Kiyan. Reply to comment on photodetachment in a strong laser field: An experimental test of keldysh-like theories. *Phys. Rev. A*, 77:067402, Jun 2008. doi:10.1103/PhysRevA.77.067402. URL `http://link.aps.org/doi/10.1103/PhysRevA.77.067402`.

[56] D.M. Wolkow. über eine klasse von lösungen der diracschen gleichung. *Zeitschrift für Physik*, 94(3-4):250–260, 1935. ISSN 0044-3328. doi:10.1007/BF01331022. URL `http://dx.doi.org/10.1007/BF01331022`.

[57] P. Debye. Näherungsformeln für die zylinderfunktionen für grosse werte des arguments und unbeschränkt veränderliche werte des index. *Mathematische Annalen*, 67(4):535–558, 1909. ISSN 0025-5831. doi:10.1007/BF01450097. URL `http://dx.doi.org/10.1007/BF01450097`.

[58] S. P. Goreslavski, G. G. Paulus, S. V. Popruzhenko, and N. I. Shvetsov-Shilovski. Coulomb asymmetry in above-threshold ionization. *Phys. Rev. Lett.*, 93:233002, Nov 2004. doi:10.1103/PhysRevLett.93.233002. URL `http://link.aps.org/doi/10.1103/PhysRevLett.93.233002`.

[59] N L Manakov, M V Frolov, B Borca, and Anthony F Starace. Multiphoton detachment of a negative ion by an elliptically polarized, monochromatic laser field. *Journal of Physics B: Atomic, Molecular and Optical Physics*, 36(9):R49, 2003. URL `http://stacks.iop.org/0953-4075/36/i=9/a=201`.

[60] Mary M Tai. A mathematical model for the determination of total area under glucose tolerance and other metabolic curves. *Diabetes Care*, 17(2):152–154, 1994. doi:10.2337/diacare.17.2.152. URL `http://care.diabetesjournals.org/content/17/2/152.abstract`.

[61] Karl Blum. *Density Matrix Theory and Applications*. Plenum, New York, 1981.

[62] Vladimir Dribinski, Alexei Ossadtchi, Vladimir A. Mandelshtam, and Hanna Reisler. Reconstruction of abel-transformable images: The gaussian basis-set expansion abel transform method. *Review of Scientific Instruments*, 73(7):2634–2642, 2002. doi:10.1063/1.1482156. URL `http://scitation.aip.org/content/aip/journal/rsi/73/7/10.1063/1.1482156`.

[63] Gustavo A. Garcia, Laurent Nahon, and Ivan Powis. Two-dimensional charged particle image inversion using a polar basis function expansion. *Review of Scientific Instruments*, 75(11):4989–4996, 2004. doi:10.1063/1.1807578. URL `http://scitation.aip.org/content/aip/journal/rsi/75/11/10.1063/1.1807578`.

[64] R.N. Bracewell. Numerical transforms. *Science*, 248(4956):697, 1990. doi:10.1126/science.248.4956.697.

[65] Y. Nievergelt. Elementary inversion of radons transform. *SIAM Review*, 28(1): 79–84, 1986. doi:10.1137/1028005. URL `http://epubs.siam.org/doi/abs/10.1137/1028005`.

[66] Light Conversion. URL `http://lightcon.com/products/product.php?ID=162`.

[67] Peabody Scientific. URL `http://peabody-scientific.com/page13.html`.

[68] Rainer Reichle, Hanspeter Helm, and Yu. Igor Kiyan. Detailed comparison of theory and experiment of strong-field photodetachment of the negative hydrogen ion. *Phys. Rev. A*, 68:063404, Dec 2003. doi:10.1103/PhysRevA.68.063404. URL `http://link.aps.org/doi/10.1103/PhysRevA.68.063404`.

[69] M. Uiberacker, Th Uphues, M. Schultze, A. J. Verhoef, V. Yakovlev, M. F. Kling, J. Rauschenberger, N. M. Kabachnik, H. Schröder, M. Lezius, K. L. Kompa, H.-G. Muller, M. J. J. Vrakking, S. Hendel, U. Kleineberg, U. Heinzmann, M. Drescher, and F. Krausz. Attosecond real-time observation of electron tunnelling in atoms. *Nature*, 446(7136):627–632, Apr 2007. ISSN 0028-0836. doi:10.1038/nature05648. URL `http://dx.doi.org/10.1038/nature05648`.

[70] G. Sansone, F. Kelkensberg, J. F. Perez-Torres, F. Morales, M. F. Kling, W. Siu, O. Ghafur, P. Johnsson, M. Swoboda, E. Benedetti, F. Ferrari, F. Lepine, J. L. Sanz-Vicario, S. Zherebtsov, I. Znakovskaya, A. L'Huillier, M. Yu Ivanov, M. Nisoli, F. Martin, and M. J. J. Vrakking. Electron localization following attosecond molecular photoionization. *Nature*, 465(7299):763–766, Jun 2010. ISSN 0028-0836. doi:10.1038/nature09084. URL `http://dx.doi.org/10.1038/nature09084`.

[71] Matthias Wollenhaupt and Thomas Baumert. Ultrafast laser control of electron dynamics in atoms, molecules and solids. *Faraday Discuss.*, 153:9–26, 2011. doi:10.1039/C1FD00109D. URL `http://dx.doi.org/10.1039/C1FD00109D`.

[72] M.V. Ammosov, N.B. Delone, and V.P. Krainov. Tunnel ionization of complex atoms and of atomic ions in an alternating electromagnetic field. *Sov. Phys. JETP*, 64(6):1191, 1986. URL `http://www.jetp.ac.ru/cgi-bin/e/index/e/64/6/p1191?a=list`.

[73] M. V. Frolov, N. L. Manakov, E. A. Pronin, and Anthony F. Starace. Model-independent quantum approach for intense laser detachment of a weakly bound electron. *Phys. Rev. Lett.*, 91:053003, Aug 2003. doi:10.1103/PhysRevLett.91.053003. URL `http://link.aps.org/doi/10.1103/PhysRevLett.91.053003`.

[74] Richard Taïeb, Valérie Véniard, and Alfred Maquet. Photoelectron spectra from multiple ionization of atoms in ultra-intense laser pulses. *Phys. Rev. Lett.*, 87: 053002, Jul 2001. doi:10.1103/PhysRevLett.87.053002. URL `http://link.aps.org/doi/10.1103/PhysRevLett.87.053002`.

[75] S. J. McNaught, J. P. Knauer, and D. D. Meyerhofer. Measurement of the initial condition of electrons ionized by a linearly polarized, high-intensity laser. *Phys. Rev. Lett.*, 78:626–629, Jan 1997. doi:10.1103/PhysRevLett.78.626. URL `http://link.aps.org/doi/10.1103/PhysRevLett.78.626`.

[76] C. I. Moore, A. Ting, S. J. McNaught, J. Qiu, H. R. Burris, and P. Sprangle. A laser-accelerator injector based on laser ionization and ponderomotive acceleration of electrons. *Phys. Rev. Lett.*, 82:1688–1691, Feb 1999. doi:10.1103/PhysRevLett.82.1688. URL `http://link.aps.org/doi/10.1103/PhysRevLett.82.1688`.

[77] E. Gubbini, U. Eichmann, M. Kalashnikov, and W. Sandner. Core relaxation in atomic ultrastrong laser field ionization. *Phys. Rev. Lett.*, 94:053602, Feb 2005. doi:10.1103/PhysRevLett.94.053602. URL `http://link.aps.org/doi/10.1103/PhysRevLett.94.053602`.

[78] Hugo W. van der Hart. Influence of magnetic quantum number m and spin-angular symmetry on sequential double detachment in strong laser fields. *Phys. Rev. A*, 74:053406, Nov 2006. doi:10.1103/PhysRevA.74.053406. URL `http://link.aps.org/doi/10.1103/PhysRevA.74.053406`.

[79] J B Greenwood, G F Collins, J Pedregosa-Gutierrez, J McKenna, A Murphy, and J T Costello. Double ionization of atomic negative ions in an intense laser field. *Journal of Physics B: Atomic, Molecular and Optical Physics*, 36(16):L235, 2003. URL `http://stacks.iop.org/0953-4075/36/i=16/a=101`.

[80] L. Young, D. A. Arms, E. M. Dufresne, R. W. Dunford, D. L. Ederer, C. Höhr, E. P. Kanter, B. Krässig, E. C. Landahl, E. R. Peterson, J. Rudati, R. Santra, and S. H. Southworth. X-ray microprobe of orbital alignment in strong-field ionized atoms. *Phys. Rev. Lett.*, 97:083601, Aug 2006. doi:10.1103/PhysRevLett.97.083601. URL `http://link.aps.org/doi/10.1103/PhysRevLett.97.083601`.

[81] S. H. Southworth, D. A. Arms, E. M. Dufresne, R. W. Dunford, D. L. Ederer, C. Höhr, E. P. Kanter, B. Krässig, E. C. Landahl, E. R. Peterson, J. Rudati, R. Santra, D. A. Walko, and L. Young. k-edge x-ray-absorption spectroscopy of laser-generated Kr^{+} and Kr^{2+}. *Phys. Rev. A*, 76:043421, Oct 2007. doi:10.1103/PhysRevA.76.043421. URL `http://link.aps.org/doi/10.1103/PhysRevA.76.043421`.

[82] C. Höhr, E. R. Peterson, N. Rohringer, J. Rudati, D. A. Arms, E. M. Dufresne, R. W. Dunford, D. L. Ederer, E. P. Kanter, B. Krässig, E. C. Landahl, R. Santra, S. H. Southworth, and L. Young. Alignment dynamics in a laser-produced plasma. *Phys. Rev. A*, 75:011403, Jan 2007. doi:10.1103/PhysRevA.75.011403. URL `http://link.aps.org/doi/10.1103/PhysRevA.75.011403`.

[83] Robin Santra, Robert W. Dunford, and Linda Young. Spin-orbit effect on strong-field ionization of krypton. *Phys. Rev. A*, 74:043403, Oct 2006. doi:10.1103/PhysRevA.74.043403. URL `http://link.aps.org/doi/10.1103/PhysRevA.74.043403`.

[84] Nina Rohringer and Robin Santra. Multichannel coherence in strong-field ionization. *Phys. Rev. A*, 79:053402, May 2009. doi:10.1103/PhysRevA.79.053402. URL `http://link.aps.org/doi/10.1103/PhysRevA.79.053402`.

[85] Boris Bergues and Igor Yu. Kiyan. Two-electron photodetachment of negative ions in a strong laser field. *Phys. Rev. Lett.*, 100:143004, Apr 2008. doi:10.1103/PhysRevLett.100.143004. URL `http://link.aps.org/doi/10.1103/PhysRevLett.100.143004`.

[86] Michael Scheer, René C. Bilodeau, Cicely A. Brodie, and Harold K. Haugen. Systematic study of the stable states of C^-, Si^-, Ge^-, and Sn^- via infrared laser spectroscopy. *Phys. Rev. A*, 58:2844–2856, Oct 1998. doi:10.1103/PhysRevA.58.2844. URL `http://link.aps.org/doi/10.1103/PhysRevA.58.2844`.

[87] A. Kramida, Yu. Ralchenko, J. Reader, and NIST ASD Team. *NIST Atomic Spectra Database (version 5.0.0), [Online].* National Institute of Standards and Technology, Gaithersburg, MD, 2012. URL `http://physics.nist.gov/asd`.

[88] H. F. Rey and H. W. van der Hart. Probing spin-orbit-interaction-induced electron dynamics in the carbon atom by multiphoton ionization. *Phys. Rev. A*, 90:033402, Sep 2014. doi:10.1103/PhysRevA.90.033402. URL `http://link.aps.org/doi/10.1103/PhysRevA.90.033402`.

[89] G. Gribakin. Private Communication.

[90] Katharine L. Reid. Photoelectron angular distributions. *Annual Review of Physical Chemistry*, 54(1):397–424, 2003. doi:10.1146/annurev.physchem.54.011002.103814. URL `http://dx.doi.org/10.1146/annurev.physchem.54.011002.103814`. PMID: 12574491.

[91] Muhammad Saeed, Mark J. Dyer, and Hanspeter Helm. Spatial anisotropy of the velocity of electrons emitted from a short-pulse laser focus. *Phys. Rev. A*, 49:1491–1493, Feb 1994. doi:10.1103/PhysRevA.49.1491. URL `http://link.aps.org/doi/10.1103/PhysRevA.49.1491`.

[92] René C Bilodeau, Michael Scheer, and Harold K Haugen. Infrared laser photodetachment of transition metal negative ions: studies on Cr^-, Mo^-, Cu^- and Ag^-. *Journal of Physics B: Atomic, Molecular and Optical Physics*, 31(17):3885, 1998. URL `http://stacks.iop.org/0953-4075/31/i=17/a=013`.

[93] Mikael Eklund, Hannes Hultgren, Dag Hanstorp, and Igor Yu. Kiyan. Orbital alignment in atoms generated by photodetachment in a strong laser field. *Phys. Rev. A*, 88:023423, Aug 2013. doi:10.1103/PhysRevA.88.023423. URL `http://link.aps.org/doi/10.1103/PhysRevA.88.023423`.

[94] Hannes Hultgren, Mikael Eklund, Dag Hanstorp, and Igor Yu. Kiyan. Electron dynamics in the ground state of a laser-generated carbon atom. *Phys. Rev. A*, 87:031404, Mar 2013. doi:10.1103/PhysRevA.87.031404. URL `http://link.aps.org/doi/10.1103/PhysRevA.87.031404`.

[95] H. R. Reiss. Comment on “photodetachment in a strong laser field: An experimental test of keldysh-like theories”. *Phys. Rev. A*, 77:067401, Jun 2008. doi:10.1103/PhysRevA.77.067401. URL `http://link.aps.org/doi/10.1103/PhysRevA.77.067401`.

[96] N.L. Manakov, V.D. Ovsiannikov, and L.P. Rapoport. Atoms in a laser field. *Physics Reports*, 141(6):320 – 433, 1986. ISSN 0370-1573. doi:10.1016/S0370-1573(86)80001-1. URL `http://www.sciencedirect.com/science/article/pii/S0370157386800011`.

[97] Kent M. Ervin and W. C. Lineberger. Photoelectron spectra of dicarbon(1-) and ethynyl(1-). *The Journal of Physical Chemistry*, 95(3):1167–1177, 1991. doi:10.1021/j100156a026. URL `http://dx.doi.org/10.1021/j100156a026`.

[98] M. Dupuis and B. Liu. Theoretical study of C_2 and C_2^-. *The Journal of Chemical Physics*, 73(1):337–342, 1980. doi:10.1063/1.439879. URL `http://scitation.aip.org/content/aip/journal/jcp/73/1/10.1063/1.439879`.

[99] Mark R. Nimlos, Lawrence B. Harding, and G. Barney Ellison. The electronic states of Si_2 and Si_2^- revealed by photoelectron spectroscopy. *The Journal of Chemical Physics*, 87(9):5116–5124, 1987. doi:10.1063/1.453679. URL `http://scitation.aip.org/content/aip/journal/jcp/87/9/10.1063/1.453679`.

[100] T. N. Kitsopoulos, C. J. Chick, Y. Zhao, and D. M. Neumark. Study of the lowlying electronic states of Si_2 and Si_2^- using negative ion photodetachment techniques. *The Journal of Chemical Physics*, 95(3):1441–1448, 1991. doi:10.1063/1.461057. URL `http://scitation.aip.org/content/aip/journal/jcp/95/3/10.1063/1.461057`.

[101] Caroline C. Arnold, Theofanis N. Kitsopoulos, and Daniel M. Neumark. Reassignment of the Si_2^- photodetachment spectra. *The Journal of Chemical Physics*, 99(1):766–768, 1993. doi:10.1063/1.465757. URL `http://scitation.aip.org/content/aip/journal/jcp/99/1/10.1063/1.465757`.

[102] Joe Ho, Kent M. Ervin, and W. C. Lineberger. Photoelectron spectroscopy of metal cluster anions: Cu_n^-, Ag_n^-, and Au_n^-. *The Journal of Chemical Physics*, 93 (10):6987–7002, 1990. doi:10.1063/1.459475. URL `http://scitation.aip.org/content/aip/journal/jcp/93/10/10.1063/1.459475`.

[103] Rainer Reichle, Hanspeter Helm, and Igor Yu. Kiyan. Photodetachment of H^- in a strong infrared laser field. *Phys. Rev. Lett.*, 87:243001, Nov 2001. doi:10.1103/PhysRevLett.87.243001. URL `http://link.aps.org/doi/10.1103/PhysRevLett.87.243001`.

[104] M. Busuladžić, A. Gazibegović-Busuladžić, D. B. Milošević, and W. Becker. Strong-field approximation for ionization of a diatomic molecule by a strong laser field. ii. the role of electron rescattering off the molecular centers. *Phys. Rev. A*, 78:033412, Sep 2008. doi:10.1103/PhysRevA.78.033412. URL `http://link.aps.org/doi/10.1103/PhysRevA.78.033412`.